Decomposition of 3D joint kinematics of walking in *Drosophila melanogaster*

Inaugural-Dissertation

zur

Erlangung des Doktorgrades

der Mathematisch-Naturwissenschaftlichen Fakultät

der Universität zu Köln

vorgelegt von

Moritz Haustein

aus Düsseldorf

2023

Berichterstatter (Gutachter):

Prof. Dr. Ansgar Büschges

Prof. Dr. Martin Nawrot

Tag der mündlichen Prüfung:

1. März, 2023

Table of contents

Abstract

Animals exhibit a rich repertoire of locomotive behaviors. In the context of legged locomotion, i.e. walking, animals can change their heading direction, traverse diverse substrates with different speeds, or can even compensate for the loss of a leg. This versatility emerges from the fact that biological limbs have more joints and/or more degrees of freedom (DOF), i.e. independent directions of motions, than required for any single movement task. However, this further entails that multiple, or even infinitely many, joint configuration can result in the same leg stepping pattern during walking. How the nervous system deals with such kinematic redundancy remains still unknown. One proposed hypothesis is that the nervous system does not control individual DOFs, but uses flexible combinations of groups of anatomical or functional DOFs, referred to as motor synergies.

Drosophila melanogaster represents an excellent model organism for studying the motor control of walking, not least because of the extensive genetic toolbox available, which, among others, allows the identification and targeted manipulation of individual neurons or muscles. However, their tiny size and ability for relatively rapid leg movements hampered research on the kinematics at the level of leg joints due to technical limitations until recently.

Hence, the main objective of this dissertation was to investigate the three-dimensional (3D) leg joint kinematics of *Drosophila* during straight walking. For this, I first established a motion capture setup for *Drosophila* which allowed the accurate reconstruction of the leg joint positions in 3D with high temporal resolution (400 Hz). Afterwards, I created a kinematic leg model based on anatomical landmarks, i.e. joint condyles, extracted from micro computed-tomography scan data. This step was essential insofar that the actual DOFs of the leg joints in *Drosophila* were currently unknown. By using this kinematic model, I have found that a mobile trochanter-femur joint can best explain the leg movements of the front legs, but is not mandatory in the other leg pairs. Additionally, I demonstrate that rotations of the femur-tibia plane in the middle legs arise from interactions between two joints suggesting that the natural orientation of joint rotational axes can extent the leg movement repertoire without increasing the number of elements to be controlled. Furthermore, each leg pair exhibited distinct joint kinematics in terms of the joint DOFs employed and their angle time courses during swing and stance phases.

Since it is proposed that the nervous system could use motor synergies to solve the redundancy problem, I finally aimed to identify kinematic synergies based on the obtained joint angles from the kinematic model. By applying principal component analysis on the mean joint angle sets of leg steps, I found that three kinematic synergies are sufficient to reconstruct the movements of the tarsus tip during stepping for all leg pairs. This suggests that the problem of controlling seven to eight joint DOFs can be in principal reduced to three control parameters.

In conclusion, this dissertation provides detailed insights into the leg joint kinematics of *Drosophila* during forward walking which are relevant for deciphering motor control of walking in insects. When combined with the extensive genetic toolbox offered by *Drosophila* as model organism, the experimental platform presented here, i.e. the 3D motion capture setup and the kinematic leg model, can facilitate investigations of *Drosophila* walking behavior in the future.

List of abbreviations

3D	three-dimensional
2D	two-dimensional
AHCA	agglomerative hierarchical cluster analysis
ANN	artificial neural network
BPN	bolt protocerebral neurons
CI	confidence interval
CNN	convolutional neural network
CPG	central pattern generator
CQV	coefficient of quartile variation
CX	coxa
CxTr	coxa-trochanter joint
D-H	Denavit-Hartenberg
DLC	DeepLabCut
DOF	degree of freedom
EMG	electromyogram
fCO	femoral chordotonal organ
FE	femur
FeTi	femur-tibia joint
IR	infrared
IQR	interquartile range
LCS	local coordinate system
LED	light emitting diode
PC	principal component
PCA	principal component analysis
SD	standard deviation
SEM	standard error of the mean
SVD	singular value decomposition
Tar	tarsus tip
TAR	tarsus
ThAp	thorax posterior scutellum apex

ThCx	thorax-coxa joint
TI	tibia
TiTar	tibia-tarsus joint
TR	trochanter
TrFe	trochanter-femur joint
TTL	transistor-transistor logic
WH	wing hinge

Chapter 1

General introduction

1.1 Legged locomotion

The ability to navigate through their habitats allows animals to perform a huge variety of essential behavioral activities such as foraging, mating, and escaping predators or unfavorable conditions. Hence, it is not surprising that locomotion was immensely fostered during animal evolution resulting in the emergence of a vast diversity of body morphologies optimized for a wide range of movement types (Dickinson et al., 2000; Zenkevich, 1945). Animals explore their environments by walking, crawling, swimming, and flying, or by more specialized modes of locomotion such as brachiation, burrowing, or hopping (Ijspeert, 2002). Despite this diversity of locomotion strategies, the fundamental principle of locomotion is that animals need to exert force on the external world to propel their bodies towards the intended direction (Dickinson et al., 2000; Holmes et al., 2006). This force is generated by rhythmical muscle activity, often originating from antagonistic muscle groups and rigorously controlled by the nervous system. Since animals live in a dynamic environment, i.e. conditions are constantly changing and perturbations can occur at any time, the motor output of the nervous system must be continuously updated to cope with unforeseen challenges. For this, animals have developed a large variety of sensory organs and the emerging sensory feedback is used to adjust the output of the nervous system's rhythm generating networks or motor neurons. In addition, goal-orientated locomotor behaviors are realized by modulatory actions of descending input from higher areas of the nervous system on the motor control circuits. In summary, locomotion is the outcome of a complex interplay of neural processes, muscle activity, biomechanical properties and morphology of body parts used, and external influences by the prevailing environmental conditions (Dickinson et al., 2000; Holmes et al., 2006; Nishikawa et al., 2007; Seipel et al., 2017).

In the context of terrestrial animals, legged locomotion, is the main mode of locomotion on land (Biewener and Patek, 2018). For this, animals perform recurrent and coordinated

movements of multi-jointed body appendages, commonly called limbs or legs, to propel the body forward. Although a variety of subtypes of legged locomotion is used by some animals (e.g. hopping, jumping, or climbing), walking and its faster manifestations such as e.g. running can be considered as the standard method of traveling on legs (Alexander, 1992). In this context, legs are moved in a cyclic pattern to generate stepping, which can be roughly divided in two phases. During the stance or power stroke phase, the leg is in contact with the ground and the emerging force is used for propulsion of the body. In contrast, the swing or return stroke phase is characterized by the leg being lifted off the ground and moved to the starting position of the next stance phase. To produce proper leg steps, the nervous system must spatiotemporally coordinate the motion of the multiple leg segments (intraleg coordination) and the demands on coordination change dramatically at the transitions between the step phases. For instance, mechanical coupling plays a rather minor role during the swing phase, while the leg is coupled mechanically to the ground during the stance phase (Cruse et al., 2009).

Although legs usually occur in pairs, animal species differ in the number of legs they possess: humans and birds move with two legs (bipeds), most mammals, amphibians, and reptiles have four legs (tetrapods), insects use six legs (hexapods), spiders have eight legs (octapods), and centipedes or millipedes have even more legs (up to 750). Consequently, the movements of individual legs must also be spatiotemporally coordinated among each other (interleg coordination) to establish an appropriated gait that propels the body but also stabilizes it at the same time (Alexander, 2006). Importantly, gaits are distinct modes of interleg coordination optimized for energy consumption at a certain speed and the transition between them is discontinuous (Alexander, 1989). Animals therefore change their gait according to traveling speed. For instance, a horse walks at low speeds, switch to trot at intermediate speeds, and will gallop at high speeds.

The neural basis of locomotion was extensively studied during the last century. It is now generally accepted that central pattern generators (CPGs) are essential for the generation of the complex motor patterns that underlie all kinds of animal locomotion (for review: Grillner, 2006; Grillner and El Manira, 2020; MacKay-Lyons, 2002; Mantziaris et al., 2020) including walking (for review: Grillner and Kozlov, 2021; Mantziaris et al., 2020). CPGs are networks of

interneurons that can generate the basic rhythmic activity required to organize and drive the timing, phasing, and intensity of motor neurons without rhythmic input from descending or sensory signals (Harris-Warrick and Ramirez, 2017). However, to allow robust and flexible motor behaviors, CPGs process and integrate sensory feedback and their activity is modulated by descending signals from higher areas of the nervous system. Although CPGs for e.g. swimming are today well understood, there is still a lack of knowledge about how CPGs function in the context of legged locomotion (Grillner and Kozlov, 2021).

1.2 Motor control of walking in insects

Motor control of walking is frequently investigated in insects, because on the one hand insects and vertebrates obey many of the same general principles of locomotion (Büschges, 2005; Duysens et al., 2000; Pearson, 1993), while on the other hand their relatively simple nervous systems facilitate the examination of the underlying neural control mechanisms (Bidaye et al., 2018).

Insects have six legs attached pairwise to the three thoracic segments and each leg consists of five main segments: the coxa, the trochanter, the femur, the tibia, and the tarsus which comprises at least four tarsal segments. In addition, the trochanter is fused to the femur in some insect species such as e.g. the stick insect and the locust (Cruse et al., 2009; Frantsevich and Wang, 2009), whereas the joint between the trochanter and femur is mobile in other species, e.g. the cockroach (Bender et al., 2010). Movements of segments about the leg joints are driven by sets of antagonistic muscles (Bidaye et al., 2018; Büschges, 2005; Mantziaris et al., 2020), except for the tarsus which is under control of a single tripartite muscle (Radnikov and Bässler, 1991; Soler et al., 2004).

Neural control of leg stepping in insects is currently best understood in the middle leg of the stick insect (for review: Bidaye et al., 2018; Büschges et al., 2008; Mantziaris et al., 2020). Here, each of the main leg joints for walking, i.e. the thorax-coxa, the coxa-trochanter, and the femur-tibia joint, is controlled by a distinct CPG that generate and/or support alternating activity between motor neuron pools, which in turn drive the muscle contractions of the antagonistic

muscle groups (Büschges et al., 1995; Mantziaris et al., 2020). For proper stepping, the required temporal sequence of leg segments movements, i.e. intraleg coordination, is largely shaped by sensory feedback signals that couple the activities of the individual CPGs (Bidaye et al., 2018; Büschges et al., 2008; Mantziaris et al., 2020).

Insect legs are equipped with a variety of mechanoreceptors that monitor the position and movement of the legs or sensing external stimuli (Tuthill and Wilson, 2016). For instance, campaniform sensilla sense strain and stress in the cuticle and thus provide feedback on the muscle forces and load exerted on the legs (Zill et al., 2004). When considering that the mechanical load on a leg changes drastically during the transition between swing and stance phase, it is not surprising that sensory feedback from campaniform sensilla has been found to assist the initiation and maintenance of stance movements in multiple ways (Akay et al., 2001; Akay et al., 2007; Borgmann et al., 2011). In contrast, flexion and extension of leg segments is monitored by chordotonal organs (Field and Matheson, 1998). For example, the femoral chordotonal organ (fCO) provides detailed information about the movements of the tibia in terms of position, velocity, and acceleration (Büschges, 1994; Mamiya et al., 2018; Matheson, 1990; Usherwood et al., 1968; Zill, 1985) and detects vibrations of the tibia (Mamiya et al., 2018; Stein and Sauer, 1999). Evidence for the involvement of the fCO in stepping emerges from the findings that experimental manipulations of fCO feedback strongly affect tibial movements in active animals (Weiland and Koch, 1987; Weiland et al., 1986; Zill, 1987). Moreover, in reduced preparations of the stick insect, flexion and extension signals from the fCO had opposite effects on the antagonistic muscles that control leg levation and depression, i.e. the trochanter muscles, suggesting that the fCO is involved in the transitions from swing to stance and vice versa (Hess and Büschges, 1999). In addition, hair plates and rows, which consists of multiple tactile bristles and are commonly located directly at the leg joints, signal when a joint is fully flexed (Pearson et al., 1976; Pringle, 1938; Wong and Pearson, 1976) as well as multipolar stretch receptors may monitor leg flexion (Desai et al., 2014) and could be involved in leg reflex responses (Guthrie, 1967). Altogether, a substantial body of knowledge has accumulated on how the combined sensory feedback from the various sensory organs contributes to intraleg coordination (Bidaye et al., 2018; Büschges, 2005; Büschges et al., 2008). In a nutshell, the transition from swing to stance is initiated by position and movement signals, while a reduction in load and position signals of a leg mediate stance to swing

transition, and load and movement signals reinforce stance movements. Importantly, sensory feedback signals do not only shape the motor output by affecting the activity of CPGs (e.g. Akay et al., 2004; Akay et al., 2007; Hess and Büschges, 1999), but can also act directly on motor neurons (e.g. Burrows and Pflüger, 1988; Gebehart and Büschges, 2021). Sensory feedback can therefore adjust both the timing and the magnitude of the motor output during walking (Büschges, 2005).

In terms of interleg coordination, it is well-established that insects move their legs in different prototypical coordination patterns depending on their walking speed (Bidaye et al., 2018; Graham, 1972; Wahl et al., 2015; Wilson, 1966; Wosnitza et al., 2013). Insects use a wave gait in which the legs step in a sequence from the back to the front along each body side at low walking speeds (Hughes, 1952). Consequently, only a single leg is in swing phase at a given time, while the remaining five legs are in stance phase. At intermediate, insects use a tetrapod coordination pattern (Burns, 1973; Graham, 1972; Wosnitza et al., 2013). Here, four legs are in stance phase all the time, while two legs are simultaneously in swing phase. At high speeds, the coordination pattern switches to tripod in which the ipsilateral front and hind legs as well as the contralateral middle leg are simultaneously in swing phase, while the remaining three legs are in stance phase (Delcomyn, 1971; Graham, 1985; Strauß and Heisenberg, 1990; Wahl et al., 2015; Wosnitza et al., 2013). In addition, cockroaches uses also a bipedal anti-phase coordination pattern of their hind legs during high-speed escape as the anterior body part of the animal is lifted and consequently the front and hind legs do not contact the ground (Full and Tu, 1991). Remarkably, in contrast to the discontinuous transition between gaits in vertebrates, speed-dependent transition between interleg coordination patterns can occur seamlessly in insects (Szczecinski et al., 2018; Wosnitza et al., 2013).

It was shown that interleg coordination in insects mainly emerges through to two neural mechanisms, i.e. direct coupling between intersegmental CPGs (Ayali et al., 2015; David et al., 2016; Fuchs et al., 2011; Johnston and Levine, 2002) and sensory feedback from other body segments (Borgmann et al., 2009; Ludwar et al., 2005; Stein et al., 2006; Zill et al., 2009). However, the contribution of each mechanism appears to differ between species or to depend on walking speed. In the complete absence of sensory and descending input, CPG coordination resemble a tripod walking pattern in fast walking species such as the hawk moth

and the cockroach, arguing for strong coupling between the CPGs involved (David et al., 2016; Johnston and Levine, 2002). In contrast, only weak coupling between intersegmental CPGs was observed in the stick insect, which walks rather slowly (Borgmann et al., 2009; Mantziaris et al., 2017). Moreover, when all leg sensory organs were genetically disabled in *Drosophila*, which exhibit a wide range of walking speeds (Wosnitza et al., 2013), the animals were still able to walk in a coordinated manner, but the variability in their leg kinematics was much higher at slow walking speeds than at high walking speeds (Mendes et al., 2013). All of this supports the notion that sensory feedback is more important at low walking speeds, whereas interleg coordination is mainly mediated by CPG coupling at high walking speeds (Mantziaris et al., 2020).

In addition, descending control from the brain to the motor circuits in the ventral nerve cord play a crucial role for the generation of goal-orientated locomotor behaviors such as initiation, maintenance, and termination of walking, as well as for adjusting the walking speed or walking direction, i.e. forward, backward, and turning (Bidaye et al., 2018). To date, however, little is known about how descending neuronal pathways in insects are structured and contribute to walking. Nevertheless, some descending neurons associated to forward and backwards walking were recently identified in *Drosophila* (see **1.3**). From the behavioral perspective, it is however clear that leg kinematics have to be altered to allow for adjustment of walking direction and speed. As walking speed increases, the cycle period and stance duration are decreased, while the swing duration remain largely constant across the whole range of walking speeds (Mendes et al., 2013; Wosnitza et al., 2013). In contrast, the step frequency, stride length, and stance direction in each leg is independently modified when insects perform curve walking (Dürr and Ebeling, 2005; Gruhn et al., 2009).

1.3 *Drosophila* as model organism to study walking

The fruit fly *Drosophila melanogaster* represents an excellent model organism for studying motor control of walking because animal husbandry is simple and cost effective, there is an extensive knowledge base about their genetics, physiology and development, as well as they

exhibit robust walking behavior over a wide range of speeds. Furthermore, since the anatomy of the brain is well investigated in *Drosophila* (Ito et al., 2014; Rein et al., 2002; Scheffer and Meinertzhagen, 2019) and recent work has begun to focused on capturing the whole connectome of the brain (Scheffer et al., 2020) and the motor circuits in the ventral nerve cord (Phelps et al., 2021), *Drosophila* offers tremendous potential to link anatomy, physiology, and behavior in respect to the nervous system.

Research on *Drosophila* has already led to key discoveries in the field of neuroscience in terms of e.g. sleep, learning and memory, circadian rhythm, courtship, and aggressiveness (Bellen et al., 2010; Hales et al., 2015), not at least because of the large and versatile genetic toolbox available (Hales et al., 2015; Kazama, 2015; Venken et al., 2011). For example, binary expression systems such as GAL4/UAS (Duffy, 2002) or LexA/LexAop (Chang et al., 2022) allows the exclusive expression of a gene of interest in any targeted cell population including neurons or muscles. Both systems work with two components: a transcriptional activator transgene (GAL4 or LexA) and a DNA binding sequence (UAS or LexAop). When the transcriptional activator is expressed, it binds specifically to its binding sequence which in turns drives the expression of a responder gene located directly downstream of the binding sequence. Consequently, when the transcriptional activator transgene is linked to a regulatory DNA sequence specific for a certain neuron population, the protein synthesis of the responder gene is also restricted to those neurons. For *Drosophila*, the main advantage of these expression systems is that flies carrying a transcriptional activator transgene can be crossed with another fly strain that has a responder gene with the respective binding sequence in its promoter. That allows the study of specific neuron populations or muscles using a wide range of experimental techniques in a straightforward manner. The arsenal of commonly used responder genes includes, among others, fluorescence proteins for morphological studies, calcium indicator proteins for functional imaging of neuronal or muscle activity, or channelrhodopsins that allows the transient optogenetic activation or inhibition of neurons by exposure to light (Venken et al., 2011).

These methods already helped to decipher components of the neuronal control of walking in *Drosophila* in the last decade. For instance, descending neurons were identified that drive backward walking (Bidaye et al., 2014) or are associated with the initiation of object-directed

forward steering or fast straight forward walking (Bidaye et al., 2020). Further investigations on Moonwalker Descending Neurons, which are the command-like neurons responsible for initiation and maintenance of backward walking, revealed that these target over 30 neuronal cell types with diverse responsibilities in the motor circuits of the ventral nerve cord and that they act mainly by a distributed low-level modulation of the motor circuit dynamics to generate a clear and coordinated transition to backward walking (Feng et al., 2020). Another example is the study of sensory organs in the legs and the impact of sensory feedback on walking. In this context, the role of the fCO for leg coordination was investigated extensively in *Drosophila* in recent years (Akitake et al., 2015; Chockley et al., 2022; Mamiya et al., 2018; Mendes et al., 2013). Several subpopulations of fCO neurons were found that can be distinguished by their stereotyped axonal projection patterns in the ventral nerve cord and encode different features of tibial movements, i.e. flexion and extension, movement direction, and vibrations (Mamiya et al., 2018). Strikingly, while inhibition of all fCO neurons leads to profound changes in walking kinematics (Chockley et al., 2022; Mendes et al., 2013), inhibition of some subpopulations had surprisingly mild effects on the leg kinematics, suggesting that there might be also functionally distinct subgroups of fCO neurons in addition to the anatomically identified subpopulations (Chockley et al., 2022).

The latter finding also supports the notion that investigating individual parts of the nervous system in isolation can be misleading and we need to consider also changes in behavior to fully understand how the nervous system works (Krakauer et al., 2017; Marom, 2009). In this vain, a comprehensive behavioral map of natural leg kinematics is required to link the findings from experimental manipulations of the nervous system to the behavioral aspects of walking in *Drosophila*. To date, numerous studies already investigated the kinematics of interleg coordination in *Drosophila* in terms of forward and backward walking, turning and curve walking, speed-dependent changes, role of sensory feedback, static stability, gravitational load, and leg amputation (Berendes, 2016; Chockley et al., 2022; Feng et al., 2020; Mendes et al., 2013; Mendes et al., 2014; Strauß and Heisenberg, 1990; Szczecinski et al., 2018; Wosnitza et al., 2013). In contrast, until very recently, the tiny size of *Drosophila* and its capability for relatively rapid movements hampered three-dimensional (3D) motion capture at the level of leg joints which is, however, necessary to accurately study also the kinematics of intraleg coordination (see **3.1** for more details).

1.4 The redundancy problem of motor control and motor synergies

One of the hallmarks of animal behavior is its enormous flexibility and adaptability. In terms of walking, animals can traverse diverse substrates with different speeds, change their heading direction, or can even compensate for the loss of a leg (Bidaye et al., 2018; Biewener and Patek, 2018; Bockemühl, 2017). This versatility emerges from the fact that the motor apparatus has a tremendous number of independent elemental units or degrees of freedom (DOFs) at all levels of the motor control chain that can be employed in numerous combinations to produce a diversity of complex movement patterns. For instance, each leg in *Drosophila* has nine joints and leg movements are driven by about 14 muscles (Soler et al., 2004) which are innervated by approximately 50 motor neurons (Enriquez et al., 2015). In terms of joint DOFs, the number of available DOFs may be even higher, since biological joints can allow rotations about up to three axes depending on their morphology. While this neuromechanical complexity is crucial for motor flexibility, it also entails that there is no simple one-to-one correspondence between a motor task and a motor solution, or in other words: There are multiple or redundant movement solutions for achieving the same task (Bruton and O'Dwyer, 2018). For example, animal legs have more joint DOFs than minimally required for pure walking (Full and Koditschek, 1999), implying that multiple, or even infinitely many, joint configuration can result in the same leg stepping pattern. Although this problem of redundancy in motor control was already formulated by Nicolai Bernstein over 70 years ago (Bernstein, 1967; Bernstein and Latash, 2021), the question of how the nervous system revolves it remains an important aspect of the field of neurosciences.

Motor synergies represent a proposed conceptional framework for solving the redundancy problem (for review: Bruton and O'Dwyer, 2018; Latash, 2010; Singh et al., 2018; Ting and McKay, 2007; Tresch and Jarc, 2009). The basic idea behind motor synergies is that the nervous system couples or links individual DOFs instead of controlling them independently. By using flexible combinations of such groups of anatomical or functional DOFs as building blocks for complex movements, the number of control variables for a behavioral task can be largely reduced. Following this line of thought further, motor synergies can be seen as a way to shift the control of the motor system from a redundant control space, e.g. the joint angle space, to

a hypothetical lower-dimensional motor synergy space that is non-redundant and thus more controllable (Bockemühl, 2017).

Experimental evidence for the existence of motor synergies arises from the fact that after applying statistical dimension reduction methods to electromyogram (EMG) data sets from frogs (d'Avella et al., 2003; Hart and Giszter, 2004; Tresch et al., 1999), rats (Castillo-Escario et al., 2020), cats (Torres-Oviedo et al., 2006), primates (Overduin et al., 2008), and humans (Ivanenko et al., 2004; Krishnamoorthy et al., 2003), researchers found consistently that a much smaller set of variables, i.e. muscles synergies, can be used to largely reproduce the activity time courses of a large number of muscles. For example, d'Avella et al. (2003) showed that combinations of three time-varying muscle synergies extracted from recordings of 13 hindlimb muscles, allowed the reconstruction of the entire spectrum of defensive kicking behavior in the frog. In terms of walking, Ivanenko et al. (2004) demonstrated that five muscle synergies could reproduce the temporal activation pattern of 32 muscles in humans during treadmill walking.

Some knowledge about how motor synergies might be implemented in the nervous system comes from microstimulation experiments in the spinal cord of frogs (Bizzi et al., 1991; Giszter et al., 1993) and rats (Tresch and Bizzi, 1999). These studies showed that microstimulation elicited activity in groups of muscles that moved the hind limbs of the animals to an equilibrium point in space and the final position depended on the location of the stimulation in the spinal cord. Strikingly, co-stimulation of two sites in the spinal cord resulted in vector summation of the muscle forces generated by each site separately (Mussa-Ivaldi and Bizzi, 2000). In addition, Overduin et al. (2012) could show that microstimulation in the motor cortex of primates evoked muscle synergies in the forelimbs similar to those observed in natural reaching and grasping.

However, it is important to note that the term motor synergies serves as an umbrella term for various conceptions and theories of how the elements of the motor apparatus might act together (for comprehensive summary: Bruton and O'Dwyer, 2018). Broadly speaking, motor synergies are used in the literature either as a descriptive concept, i.e. describing systematic correlations between DOFs which in turn indicate reduced dimensionality, or as an explanatory concept, i.e. formulating a hypothetical organizing structure in the nervous

system for motor control (Diedrichsen et al., 2010). The fact that both concepts are intertwined to some degree, complicates the interpretation of the role of the nervous system (explanatory concept) for synergies found in empirical data sets (descriptive concept). For instance, kinematic synergies obtained by dimension reduction methods on kinematic parameters such as e.g. joint angles also show that a smaller set of variables can explain the majority of the observed movement patterns in a variety of animals and tasks (Bockemühl et al., 2010; Catavitello et al., 2018; Federolf, 2016; Huang et al., 2021; Stetter et al., 2020). This does not only demonstrate the existence of coordinative structures in the movements studied, but also argues for an underlying control structure in the nervous system. However, since other biomechanical coupling mechanisms such as sensory feedback, muscle activation pattern, or other biomechanical constraints could also contribute to the coordination pattern found (Bockemühl et al., 2010), it is difficult to determine the actual involvement of the nervous system in movement coordination. Nevertheless, since kinematic synergies can be readily obtained from freely behaving animals, they are relevant for identification of hidden patterns in the coordination of movements. These coordinative structures can in turn be used to formulate hypothesis for the underlying motor control mechanisms of the nervous system.

1.5 Outline of the present work

As I outlined in the introduction, despite the extensive knowledge of the neural mechanisms contributing to walking in insects, there are still many gaps in our understanding of how the nervous system ultimately generates walking behavior. One problem might be that it can be very difficult to apply findings obtained under experimental constraints and at the level of the nervous system to the many manifestations of observable behavior (Krakauer et al., 2017; Marom, 2009). *Drosophila* offers the possibility to study transient manipulations of the nervous system in animals that otherwise behave normally (see **1.3**). However, this also entails that we need to understand all aspects of normal behaviors, such as walking, in order to assess the significance of behavioral changes observed during experimental manipulations.

Although leg kinematics have been extensively studied in terms of interleg coordination in *Drosophila*, there is a gap in our knowledge of the leg joint kinematics due to technical

limitations that have only recently been overcome. Thus, the main objective of the present work was to investigate the 3D leg joint kinematics of *Drosophila* during straight forward walking. For this purpose, I first established a motion capture setup for *Drosophila* capable of accurate reconstructing the positions of the leg joints in 3D with high temporal resolution (**chapter 3**).

Afterwards, I created a kinematic leg model of *Drosophila* based on anatomical joint axes to decompose the 3D joint angles from the motion capture data (**chapter 4**). This step was essential insofar that the actual DOFs of the leg joints in *Drosophila* are currently unknown. For example, there is controversy about whether the trochanter-femur joint is mobile or fused in *Drosophila* (Goldsmith et al., 2022). Moreover, kinematic models can not only serve as experimental platform for studying the requirement of individual joint DOFs, but also provide a more accurate description of joint angles and allow reconstruction of movements based on joint angle sets (see **chapter 4** for details). By using this kinematic model, I have found that a mobile trochanter-femur joint can best explain the leg movements of the front legs, but is not mandatory in the other leg pairs. Additionally, the model shows that rotations of the femur-tibia plane in the middle legs arise from two joint DOFs in the thorax-coxa joint and the coxa-trochanter joint, demonstrating that interactions between joints can extent the leg movement repertoire without increasing the number of elements to be controlled.

Although motor synergies have been studied in many species and behavioral tasks, the possibility of motor synergies as a mechanism for reducing the demands on motor control in insect walking has been rather ignored to date. Therefore, I finally aimed to identify kinematic synergies based on the obtained joint angles from the kinematic model (**chapter 5**). By using principal component analysis (PCA, introduced in **chapter 5**) on mean joint angle sets of leg steps, I found that three kinematic synergies are sufficient to reconstruct the movements of the tarsus tip during stepping for all leg pairs. This suggests that the problem of controlling seven to eight joint DOFs can be in principal reduced to three control parameters.

Chapter 2

General material and methods

2.1 Experimental animals

Experiments were performed with three to eight days-old adult male (N=7) and female (N=5) Bolt-GAL4>UAS-CsChrimson *Drosophila melanogaster* flies. This fly strain was genetically modified in such that the channelrhodopsin Chrimson (Klapoetke et al., 2014) was exclusively expressed in the Bolt protocerebral neurons (BPNs) in the brain of the flies by using the GAL4-UAS binary expression system (for review: Duffy, 2002). While BPNs are descending neurons that project to the ventral nerve cord and are associated with the induction and maintenance of straight forward walking (Bidaye et al., 2020), CsChrimson is a light-gated cation channel and exposure to red light results in the depolarization of neurons expressing CsChrimson (Klapoetke et al., 2014). Therefore, walking in experiments could simply be induced by exposure to red light in the here used fly strain. Since there are no evidence that BPN activation affects the leg kinematics in any aspect (Bidaye et al., 2020), no specific control conditions or comparisons with wild-type flies were considered in this thesis.

Animals were reared in an incubator at a constant temperature of 25°C and 65% humidity in a 12h:12h day:night cycle. Nutrition consisted of a semi-synthetic medium prepared as described in Backhaus et al. (1984).

For producing GAL4-UAS progeny, three to ten days old Bolt-GAL4 males (kindly provided by Dr. Salil Bidaye) were mated with two to three days old UAS-CsChrimson female virgins (#55134, Bloomington Drosophila Stock Center). The animals were kept in vials with fresh food and were removed after an egg laying period of three to four days. Since CsChrimson requires all-trans-Retinal for proper functioning which cannot be synthesized by the animals (Klapoetke et al., 2014), flies were transferred to fresh vials in which the food was soaked with 50 µL of a 100 mmol L^{-1} all-trans-Retinal solution. Prior to experiments, the flies were kept under all-trans-Retinal conditions and in the dark for at least three days.

2.2 Software development

All and analysis routines and graphical user interfaces used in this thesis were written in Python (version 3.9.5, Python Software Foundation, Delaware, USA, available at: https://www.python.org/), if not otherwise stated. Graphical user interfaces based on the PyQt5 library version 5.12.3 (Riverbank Computing, Dorchester, UK) and PyQtGraph framework (version 0.11.0, PyQtGraph developers, available at: https://www.pyqtgraph .org/). Numerical computations and statistical analyses were performed using NumPy version 1.20.3 (Harris et al., 2020), SciPy version 1.6.2 (Virtanen et al., 2020), and pandas version 1.3.1 (McKinney, 2010) frameworks. Data visualizations were created with seaborn version 0.11.2 (Waskom, 2021) and Matplotlib version 3.4.2 (Hunter, 2007), except for Figure 3.1B and Figure 3.2D which were created with MATLAB (release R2021a, The MathWorks Inc., Natick, USA). In addition, images of 3D model postures were created with PyQtGraph. Additional used Python frameworks, libraries, or modules are indicated in the material and methods sections of the respective chapters.

2.3 Statistical analysis

Data was expressed as mean ± standard deviation (SD), if not otherwise stated. While N denoted the number of experimental animals, n indicated the number of an analyzed feature. When the median was used, variability of the data set was indicated by the interquartile range (IQR) which was defined as the difference between the 75th and 25th percentiles. Coefficient of quartile variation (CQV) served as robust measure for dispersion in data sets and was computed using the first (Q1) and third (Q3) quartiles of the respective data set (**Eq. 2.1**).

$$CQV = \frac{Q3 - Q1}{Q3 + Q1} \tag{2.1}$$

For boxplots, whiskers represent the smallest and largest values of the data set which were not considered as outliers (**Eq. 2.2**).

$$data(i) = \begin{cases} outlier, & \text{if } data_i < Q1 - 1.5IQR \text{ OR } data_i > Q3 + 1.5IQR \\ valid, & \text{otherwise} \end{cases} \quad (2.2)$$

In this thesis, no traditional null-hypothesis significance testing was performed because of the problem that for data sets with larger n-numbers even meaninglessly small effect sizes are often deemed as statistically significant accompanied by very small p values (Altman and Krzywinski, 2017; Goodman, 2008; Hubbard and Lindsay, 2008; Nakagawa and Cuthill, 2007; Sullivan and Feinn, 2012). Since most of the n-numbers of here analyzed data sets were larger than 200, decisions about statistical significance based on p-values might therefore be misleading. Thus, 95% confidence intervals (CIs) for mean values were used here as an alternative to inform the reader about statistical significance in this thesis (**Eq. 2.3;** SEM, standard error of the mean).

$$95\%\ \text{CI} = mean \pm 1.96SEM \quad (2.3)$$

CIs indicate the precision of a point estimate to represent the underlying population, e.g. how precisely the obtained sample mean reflects the true mean of the population (Cumming and Finch, 2005; Greenfield et al., 1998; Nakagawa and Cuthill, 2007). In other words, CIs are an estimated range of values which includes the true population value at a specified probability level such as 95% (Cumming and Finch, 2005; Hays, 1973). Importantly, this does not mean that there is a 95% chance that the true parameter is covered by a 95% CI obtained from a single experiment, but it can be expected that 95% of all calculated CIs from repeating the same experiment will contain the true parameter. In addition to providing an indicator for the precision of a point estimate by the extent of the range of values covered, CIs can also be used to compare independent data sets. For instance, when testing for any value as null hypothesis, the resulting p-value would be larger than or smaller than 0.05 depending on whether this value is included in or excluded from a 95% CI, respectively (Cumming and Finch, 2005). Consequently, when zero is not covered by a 95% CI of the mean of differences between two data sets, the differences can be interpreted as statistically significant at a 0.05 level, and vice versa (Cumming and Finch, 2005; Nakagawa and Cuthill, 2007; Sullivan and Feinn, 2012). The same hold true to some extent when examining the overlap of 95% CIs of means from different

data sets. While two means are always significantly different when their 95% CIs do not overlap ($p < 0.05$), the decision of whether the null hypothesis cannot be rejected depends on the extent of an existing overlap (Austin and Hux, 2002; Cumming and Finch, 2005; Greenfield et al., 1998).

2.4 Data storage and availability

For this thesis, primary data, i.e. video recordings, were acquired and subsequently analyzed with custom-written computer routines/ graphical user interfaces. The used experimental and analysis routines are described in detail in this thesis. The primary data, intermediate data, and the source code of all analysis routines were archived on the online storage file system for institutions of the University of Cologne (https://rrzk.uni-koeln.de/en/data-storage-and-share/online-storage-sofs). Data integrity is ensured by a routinely backup procedure. Data and analysis routines are available from Moritz Haustein or Prof. Dr. Ansgar Büschges upon reasonable request.

Chapter 3

3D motion capture of forward walking *Drosophila*

3.1 Introduction

The essential prerequisite for meaningful study of animal kinematics is the accurate recording and tracking of movements. For humans, the most widely used motion capture systems today rely on the use of reflective markers attached to anatomical landmarks of the body and subsequent recording of their movements with cameras (Cheze, 2014; Colyer et al., 2018; Mündermann et al., 2006; Robertson et al., 2014). The main reason for the popularity of reflective markers is that computer vision algorithms permit their fast, straight-forward and robust tracking (Holstein and Li, 2002; Jiménez Bascones et al., 2019; Silaghi et al., 1998). This drastically reduces the workload of researchers compared to traditional methods relying on the manual annotation of each video frame. Moreover, the reconstruction of movements in 3D can simply be achieved by using multiple cameras recording the scene from different viewpoints (Cheze, 2014; Hartley and Zisserman, 2004; Jiménez Bascones et al., 2019).

Although the use of reflective markers is principally possible for capturing the motion of animals, their use is often impractical because attachment of the markers must be done under anesthesia and the markers might not be tolerated by the animal or interfere otherwise with natural behavior (Jiang et al., 2022; Sellers and Hirasaki, 2014). Moreover, reliable marker placement is very challenging in tiny animals such as insects, although some marker-based 3D motion capture systems have been developed to study locomotion at the joint level for e.g. the stick insect (Theunissen and Dürr, 2013), the cockroach (Bender et al., 2010), and the cricket (Petrou and Webb, 2012). Given that the body size of *Drosophila* is only approximately 2 mm, it is incredibly difficult to precisely attach markers always at the same positions without damaging the legs or sensory organs on them. As a result, most previous studies of *Drosophila* leg kinematics relied on the labor-intensive manual annotation of recorded high-speed videos. Consequently, analyses were restricted to a few two-dimensional (2D) anatomical positions,

commonly the tarsi tips, taken from a single camera view (e.g. Berendes, 2016; DeAngelis et al., 2019; Martin, 2004; Mendes et al., 2013; Strauß and Heisenberg, 1990; Wosnitza et al., 2013).

To date, only a single study introduced a marker-based method to track leg movements of fruit flies using custom-made marker pads soaked with a fluorescent dye (Kain et al., 2013). However, the required setup is rather sophisticated as well as expensive and it can only support two synchronized cameras with a maximum frame rate of 80 Hz. Moreover, the method is limited in that only a single segment per leg, i.e. the femur of the front and hind legs and the tibia of the middle legs, can be tracked. However, a suitable 3D motion capture system for studying the leg kinematics in *Drosophila* must not only be able to capture movements at the joint level, but also provide higher frame rates to accurately capture the rapid movements of fruit fly legs during walking.

Only recently have advances in deep learning-based pose estimation algorithms permitted fast and robust markerless tracking of body parts, referred to in this context as keypoints to distinguish from marker-based methods, in animals from video recordings (Colyer et al., 2018; Cronin, 2021; Mathis et al., 2020). Fundamentally, deep learning is based on the supervised training of artificial neural networks (ANNs) which are built from layers of interconnected artificial neurons. These neurons mathematically mimic the functioning of their biological equivalents, i.e. when the input of an artificial neuron from preceding neurons exceeds a threshold value, the neuron generates an output to all subsequently connected neurons (Emmert-Streib et al., 2020; Jain et al., 1996). The output-input relationship between two neurons is shaped by a connection weight representing the strength of synaptic coupling between them. Learning in the context of an ANN means that the proper connection weights have to been determined to enable the network to perform a specific task, i.e. providing the appropriated result for a given input (Jain et al., 1996). This is typically accomplished by supervised training, i.e. the networks are trained with data for which the correct outcome is known and the discrepancy between the desired output and the network's prediction is used to optimize the weights via a backpropagation algorithm until the network prediction error is minimal (Cunningham et al., 2008; LeCun et al., 2015).

Current pose estimation algorithms rely on a specific network architecture, termed convolution neural networks (CNNs). This architecture was inspired by the visual cortex

ventral pathway, i.e. the first two layers are similar in function to simple cells and complex cells (Hubel and Wiesel, 1962), and is therefore very well suited for computer vision tasks (Krizhevsky et al., 2012; LeCun et al., 2015; Lindsay, 2021). The first layer comprises a set of convolutional filters which are used to extract features such as edges from the image, for instance. Since the filters are not applied globally but slide over the image (mathematically, this corresponds to a convolution), the output of this layer results in a features map for each filter in which spatial relationships of the image are preserved. In the following pooling layer, the feature maps are down sampled which reduces their spatial dimensionality while retaining the most of the feature information. This step improves the robustness of the network and helps to prevent overfitting or false detections by distortions (LeCun et al., 2015; Lindsay, 2021). Additionally, some CNNs have two or more convolutional and pooling layer units in sequence to boost task performance (Mathis et al., 2020). The final layers are based on a classical ANN structure, i.e. all neurons are fully connected with each other, and are used to predict where the learned body parts are on the image. The final output of a CNN is a confidence map which shows for each pixel of the image the probability whether this pixel is part of the searched body part.

An important feature of deep learning networks for their usability is their transfer learning capability, i.e. while training of a network for a specific tasks from scratch requires a huge amount of training data sets and computational time, modifying an already trained network to perform a similar, but novel, task can be accomplished by just a few hundred training examples (Colyer et al., 2018; Cronin, 2021; Mathis et al., 2020). This has led to the deployment of a large number of networks and user-friendly toolboxes for pose estimation of various of animals, including *Drosophila,* in recent years (Arac et al., 2019; Graving et al., 2019; Günel et al., 2019; Insafutdinov et al., 2016; Karashchuk et al., 2021; Mathis et al., 2018; Nath et al., 2019; Newell et al., 2016; Pereira et al., 2020).

Hence, to analyze the leg kinematics of walking fruit flies in this thesis, a 3D motion capture setup was established based on a deep learning toolbox for pose estimation in combination with multiple state-of-the-art digital cameras that allow capturing leg joints at a high frame rate and video resolution.

3.2 Material and methods

3.2.1 Motion capture setup

To capture leg movements, tethered fruit flies walked stationarily on a spherical treadmill setup (**Figure 3.1A**). For this purpose, the flies were cold-anesthetized and placed carefully in a fly-sized hollow cut into a custom-built coolable aluminum block. Under visual control using a dissection microscope, an L-shaped copper wire (Ø: 0.15 mm) was attached to the dorsal side of the thorax with a small drop of light-curing adhesive (ESPE Sinfony, 3M ESPE AG, Seefeld, Germany). Emitting blue laser light (460 nm) for a few seconds served to light-cure the adhesive. Afterwards, the tethered flies were positioned on top of a polypropylene ball (Ø: 6 mm; Spherotech GmbH, Fulda, Germany) using a 3D-micromanipulator. As the ball was air-suspended, it could be moved freely by the flies in every possible direction during walking. To promote natural walking behavior, the flies were centered on the ball so that their lateral and vertical orientations were straight relative to the ball surface and their ground clearance was adjusted accordingly. Due to the rigidity of the copper wire, a fly's orientation and ground clearance were constant during the experiments.

Walking behavior was recorded with six synchronized high-speed cameras (acA1300-200um, Basler AG, Ahrensburg, Germany) equipped with lenses with 50 mm focal length (LM50JC1MS, Kowa Optical Products Co. Ltd., Nagoya, Japan). Cameras were arranged such that multi-view images were obtained from either body side with a front, side, and hind aspect for subsequent 3D reconstruction (**Figure 3.1A**). Videos were acquired at 400 Hz and a resolution of 896 x 540 pixels (width x height) and camera exposure time was set to 500 µs. A supplementary camera (acA1300-200 um) recording the scene from above was used for adjusting the animals on the ball and for camera calibration, but not for kinematics data acquisition. To illuminate the scene, a custom-built infra-red light emitting diode (IR-LED, 880nm; wavelength was invisible for the flies (Yamaguchi et al., 2010)) ring was mounted above the setup.

To obtain only straight walking sequences at a relative constant walking speed for subsequent analysis, rotations of the ball around all three axes of space were measured by two optical sensors (ADNS-9500; Avago Technologies, San Jose, USA) pointing at the ball's equator and

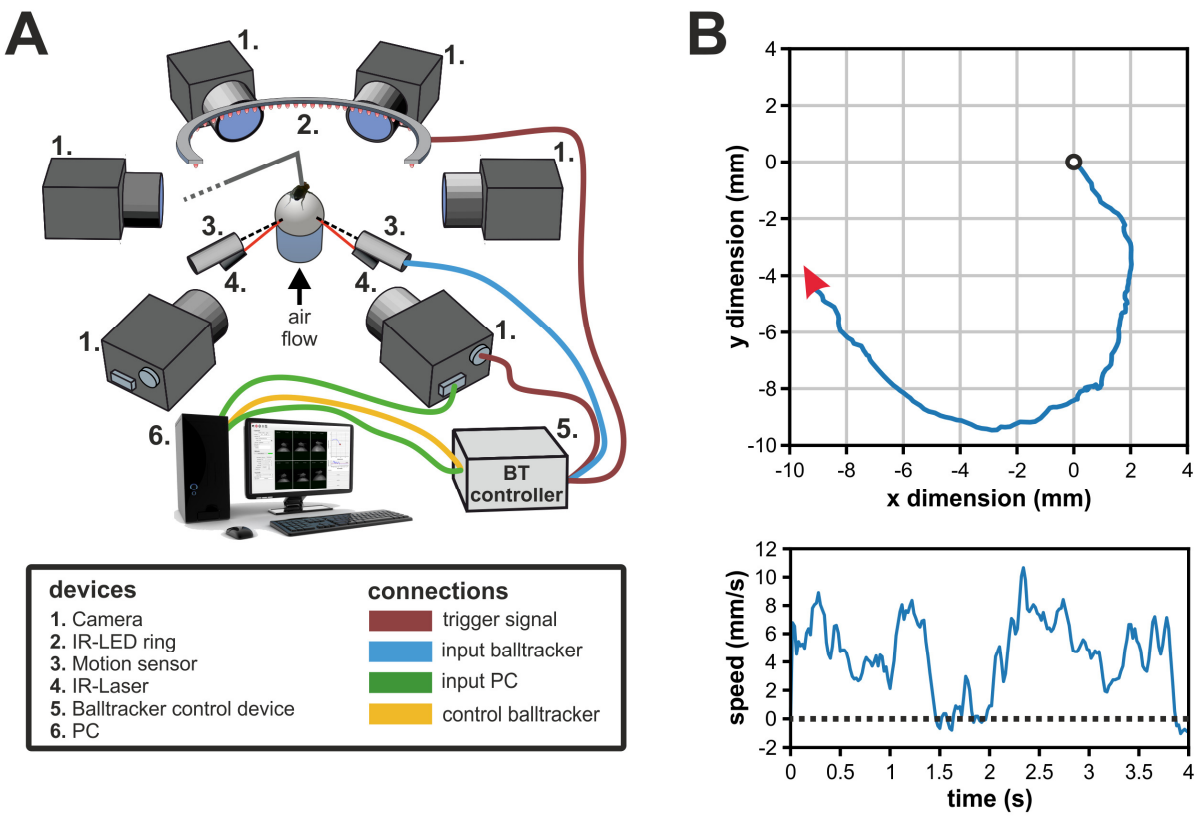

Figure 3.1. Motion capture setup. (**A**) Schematic illustration of the motion capture system. (**B**) Representative example of a recorded walking trial. The upper panel shows the virtual walking trajectory, while the lower panel depicts the forward rotational speed of the ball.

placed orthogonally to each other. The sensor areas were illuminated by two red diode laser (660 nm, 1mW; LG series, Lasertechs, Aschaffenburg, Germany) and changes in surface of the sensor areas (sampling frequency: 50 Hz) were used to calculate the global rotation of the ball (Berendes, 2016; Seelig et al., 2010). This allowed for the reconstruction of the virtual walking trajectory and the forward speed of the flies (**Figure 3.1B**).

Synchronization of cameras, the motion sensors, and IR-LED ring was achieved via transistor-transistor logic (TTL) signals send by a custom-built controller device. To adjust for the lower sampling frequency of the motion sensors, ball motion data was acquired for every 8th TTL signal and interpolated after experiments to obtain the trajectory position and walking speed for each video frame.

To initiate walking in the Bolt-Gal4>UAS-CsChrimson flies used in this thesis (for details see **2.1**), red laser light (658 nm) was emitted through an optical fiber targeting the animal's head. Walking trials were recorded for four seconds and afterwards straight walking sequences with at least five steps of each leg were extracted from the trial by manual inspection of the walking trajectory and speed. Mean stepping speed for all analyzed walking sequences was 14.7 ± 4.0 mm per second (n = 2250 steps). A custom-written non-linear contrast enhancement function was applied to the videos to improve leg joint and the tarsus tip visibility for subsequent tracking. To save hard disc space, videos were compressed using the FFmpeg library (version N-93252-gf948082e5f; codex: libx264, constant rate factor: 12, preset: ultrafast). Compression settings resulted in a reduction in file size of about 90%, while maintaining over 98% of the video quality as measured by the structural similarity index (Wang et al., 2004). Video acquisition and post-processing were accomplished with a custom-written graphical user interface. Camera control was implemented by using Harvester image acquisition library (version 1.3.1, available at: https://github.com/genicam/harvesters). If not otherwise stated, all devices were designed and built by the Electronics workshop of Zoological Institute of the University of Cologne.

3.2.2 Automated tracking of keypoints

The convolutional neural network toolbox DeepLabCut (DLC) was used (Mathis et al., 2018) for time efficient and robust detection of keypoints in the videos. For each leg, six keypoints were tracked: the thorax-coxa joint (ThCx), the coxa-trochanter joint (CxTr), the trochanter-femur joint (FeTi), the tibia-tarsus joint (TiTar), and the tip of the tarsus (Tar). In addition, the posterior scutellum apex on the thorax (ThAp), the wing hinges (left, lWH; right, rWH), and the antennae (left, lAnt; right, rAnt) were tracked as body reference keypoints. For this, three independent ResNet-50 (He et al., 2016) networks were trained to detect the keypoints in videos from cameras having the same viewpoint for both sides of the body, i.e. a single network was trained for either the both front, both side, and both hind camera views, respectively. The training sets for each network were generated by manual annotation of walking sequences of three male and three female flies with a total number of 628, 755, 753 images for the front, side, and hind network, respectively. Since transient occlusion of

proximal joint keypoints, i.e. the ThCx, CxTr, and FeTi, by movements of leg segments could not be prevented in individual camera views, estimates for occluded keypoints were added to the training sets to obtain complete positional sets for subsequent 3D reconstruction. Although this was a potential source of inaccuracies of tracked positions for these keypoints, the resulting impact can be considered minor because the proximal joints of the legs did not change their position much compared to the more distal joints during walking and the area of occlusion was relatively small.

To improve the robustness and generalizability of the networks to detect keypoints in previously unseen videos, the training sets were expanded by data augmentation techniques, i.e. manipulations such as cropping, rotation, brightness, blur, scaling were randomly applied to images and the related annotations of the original training set and subsequently added to the set as new data (Shorten and Khoshgoftaar, 2019). For this, the default in-built augmentation algorithm of DLC was used.

After training, the networks were used to predict the keypoint positions in all recorded walking sequences. All walking sequences were inspected visually and erroneous keypoint estimates were corrected manually afterwards. To evaluate the performance of the networks, the Euclidian distance between DLC predicted and manually annotated keypoint positions was calculated. All annotations of keypoints and corrections of erroneous estimates were carried out with a custom-written graphical user interface.

3.2.3 3D reconstruction of tracked keypoints

Since images depict the 2D projections of 3D world objects, inversing the camera's projective transformation allows for the extraction of depth information from images (Hartley and Zisserman, 2004). In the context of this thesis, this means that since the same keypoint was tracked from three different synchronized camera perspectives, it was possible to reconstruct the corresponding 3D positions of the keypoints by triangulation. For this, a projective model was created for each camera at first. To describe the relationship between the homogenous 3D coordinates [X, Y, Z, 1] of a point in space and its corresponding homogeneous 2D pixel coordinates [x, y, 1] on the image plane, the cameras were modeled as pinhole camera with

lens distortion (Günel et al., 2019; Hartley and Zisserman, 2004; Karashchuk et al., 2021) (**Eq. 3.1**).

$$\begin{bmatrix} x \\ y \\ 1 \end{bmatrix} = d(P \begin{bmatrix} X \\ Y \\ Z \\ 1 \end{bmatrix}) \tag{3.1}$$

In the pinhole camera model, the projection matrix P represents a map from 3D coordinates to the corresponding 2D image coordinates and is constructed by multiplying the camera intrinsics matrix K and the camera extrinsics matrix M (**Eq. 3.2**).

$$P = KM \tag{3.2}$$

The projection of a light ray onto the image plane of the camera (**Figure 3.2A**) is described by the camera intrinsics matrix (**Eq.3.3**), which encompasses the focal length f, the principal point c, i.e. the optical center of the camera, and the skew coefficient s between x- and y- axes of the image plane. However, as image plane skewing due to an incorrectly installed camera sensor is very unlikely in modern cameras (Hartley and Zisserman, 2004), it was generally set to zero.

$$K = \begin{bmatrix} f_x & s & c_x \\ 0 & f_y & c_y \\ 0 & 0 & 1 \end{bmatrix} \tag{3.3}$$

The location of the camera and the direction in which it is pointing is represented by the camera extrinsics matrix (**Eq. 3.4**). With respect to the global coordinate system, the orientation of the camera is defined by the rotational matrix R, while its position is described by the translation vector t.

$$M = [\mathbf{R}|\mathbf{t}] = \begin{bmatrix} R_{11} & R_{12} & R_{13} & t_1 \\ R_{21} & R_{22} & R_{23} & t_2 \\ R_{31} & R_{32} & R_{33} & t_3 \end{bmatrix} \tag{3.4}$$

Optical distortion describes the deformation or bending of the straight light rays by the camera lens before they reach the camera sensor. The two main types of lens distortion are radial and tangential distortion (Brown, 1971). Radial distortion describes the effect that light rays are bent more at the edges of a lens than near the center, resulting in a non-linear

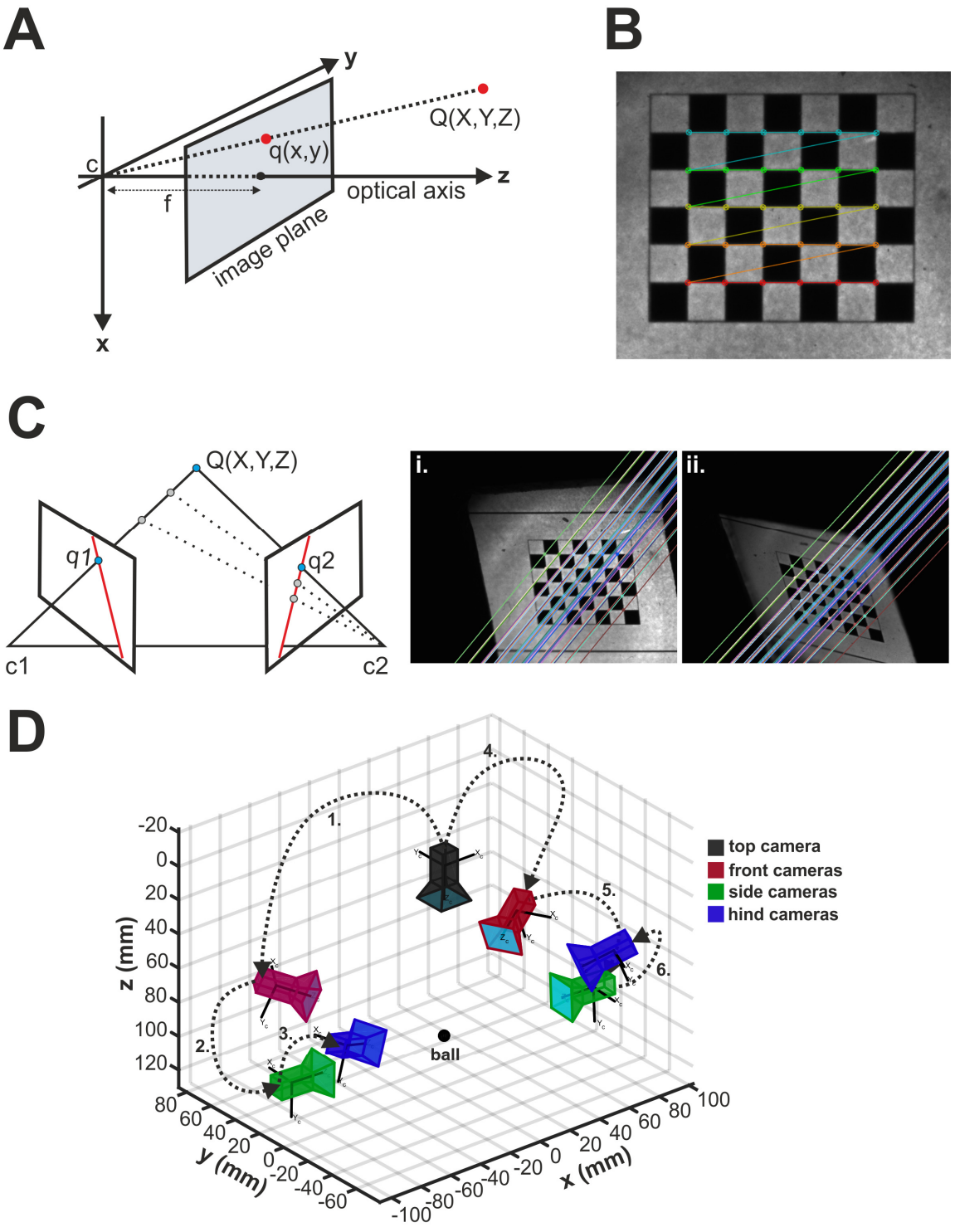

Figure 3.2. Camera calibration. (**A**) Projections in the pinhole camera model. The light ray from the world point Q is followed to the principal point c. By using the focus length f, the projected point q on the image plane can be calculated. (**B**) Example image for corner detection from used checkerboard pattern by OpenCV. (**C**) Stereo calibration relies on epipolar geometry. The world point Q (colored in blue) is projected in both image planes (q1 and q2). While all points (exemplified by the gray circles) on the line from the principal point c1 of the left camera to point Q are projected on the same point on the

image plane, i.e. q1, the points are depicted on the image plane of the right camera and lie on a line called the epipolar line (red). Consequently, points on the image plane of the right camera are on an epipolar line on the image plane of the left camera. This relationship is exploited to find the rotation and translation parameters for which the epipolar lines intersecting with their corresponding detected points. Example images for the result of a real stereo calibration are shown in **i.** and **ii.**. The checkerboard was detected in the reference camera (**i.**) and the camera for which the extrinsics parameters were determined (**ii.**). The resulting epipolar lines intersect with the detected corners of the checkerboard for both cameras, confirming an accurate calibration result. (**D**) Resulting camera poses after camera calibration of the whole setup. The global coordinate system based on the coordinate system of the top camera filming the scene from above. For the left and right camera groups, the camera extrinsics were determined pairwise (numbered dashed arrows), from the top to the front camera, from the front to the side camera, and from the side to the hind camera. This allowed to reconstruct the pose of each camera in the global coordinate system by multiplying the respective camera extrinsics matrices. Schemes in **A** and **C** were modified from Bradski and Kaehler (2008).

curvature of straight lines in the image. In contrast, tangential distortion emerges when the lens and the camera sensor are not perfectly parallel which leads to stretching and/or tilting of objects on the image. The distortion function d (**Eq. 3.5**) was used to model both types of distortion by using the coefficients k_1 ,k_2, k_3 and p_1, p_2 to account for radial and tangential distortion, respectively (Bradski and Kaehler, 2008).

$$d(\begin{bmatrix} x \\ y \end{bmatrix}) = \begin{bmatrix} x(1 + k_1 r^2 + k_2 r^4 + k_3 r^6) + 2p_1 xy + p_2(r^2 + 2x^2) \\ y(1 + k_1 r^2 + k_2 r^4 + k_3 r^6) + p_1(r^2 + 2y^2) + 2p_2 xy \end{bmatrix} \tag{3.5}$$

Camera calibration is the process for determination of the camera model parameters. Although various approaches were developed to accomplish camera calibration, the methods that yield high precision rely on imaging a 3D calibration object with a well-known geometry (Long and Dongri, 2019; Wang Qi et al., 2010). One of the most popular calibration algorithms at present was proposed by Zhang (2000) and is based on the use of planar patterns such as checkerboards. In brief, a checkerboard is presented to the camera from various viewing angles. Since the distances between the corners of the squares are known and constant, the camera parameters can be determined by optimization. For this purpose, the reprojection

error, i.e. the distance between corner positions on an image and obtained from the camera model for the same image, is minimized for all images by iteratively adjusting the camera parameters until a set of parameters is found that can model all captured poses of the checkerboard. The root mean squared reprojection errors serves as quality measure, where values of less than three pixels are acceptable, but ideally should be less than one pixel (Karashchuk et al., 2021). To obtain a checkerboard that was small enough for camera calibration of the setup used here, a custom-made checkerboard pattern with 7 x 6 squares (square dimension: 399 x 399 μm) was developed on a photographic slide (Gerstenberg Atelier für Visuelle Medien, Templin, Germany). The checkerboard pattern was cut out and clamped in a custom-made metal frame to flatten the pattern.

All camera calibration calculations were carried out with the OpenCV software library (Bradski, 2000; Bradski and Kaehler, 2008). To calibrate the camera intrinsics, images of the checkerboard were acquired at full camera resolution (1280 x 1024 pixels) with positions and angles of the checkerboard changing from image to image (n > 60 per camera). For high accuracy, subsequent detection of the checkerboard corners was performed on a sub-pixel level by using the cornerSubPix function (**Figure 3.2B**). Afterwards, the intrinsic matrix and the distortion parameters were determined with the calibrateCamera function, resulting in reprojection errors of 0.37 ± 0.07 pixels. Importantly, since camera sensors in modern machine vision cameras are very accurately installed, the principal point was fixed to the center of the calibration images (c_x=640, c_y=512) and only the focal length was estimated to define the camera intrinsics. Determination of the camera extrinsics based on stereo calibration (stereoCalibrate function), i.e. the spatial relationship between adjacent cameras, was determined. For this, the checkerboard was positioned in a way that it was imaged by two cameras (n > 20 per camera pair) and the differences between the corner positions due to the different viewing angles were used to derived the rotation matrix and translation vector required to match the reference camera to the other camera (**Figure 3.2C**). The resulting reprojection errors were 0.76 ± 0.19 pixels. The global coordinate system was defined by the camera recording the scene from above (see **3.2.1**) and the results of the pairwise stereo calibration calculations were used to determine the position and orientation of each individual camera in the global coordinate system (**Figure 3.2D**).

3D reconstruction of keypoint positions was achieved by triangulation. In principle, when the orientation and position of multiple cameras are known, the 2D projective coordinates of the same 3D object on the image planes of two or more cameras can be used to compute the intersection point of the corresponding light rays in space (Hartley and Zisserman, 2004). However, since already low levels of noise, as expected in real camera systems, can prevent the crossing of the rays in mathematical terms, finding the corresponding 3D locations in multi-camera setups is commonly defined as a linear least-squares minimization problem, i.e. the reprojection error from the approximated 3D position onto the image planes is minimized (Günel et al., 2019; Hartley and Zisserman, 2004). For this, a linear system of equations was constructed by using the relationship between the projection matrix P and the corresponding image plane coordinates of each camera c in that a certain keypoint was observable (**Eq. 3.6**). To eventually approximate the underlying 3D coordinates, the constructed linear system was solved by singular value decomposition (SVD) (Günel et al., 2019; Hartley and Zisserman, 2004; Karashchuk et al., 2021).

$$d_c^{-1}\left(\begin{bmatrix} x_c \\ y_c \end{bmatrix}\right) = P_c \begin{bmatrix} X \\ Y \\ Z \end{bmatrix} \tag{3.6}$$

To correct for lens distortion, the inverse distortion function (d^{-1}) of each camera was used to convert the 2D coordinates obtained from the video frames to the image plane of the respective pinhole camera model (OpenCV undistort function) prior to the SVD procedure. Additionally, since the walking sequences were recorded within a cropped region of the camera's full resolution (see **3.2.1**), the offset position of the recording region was added to the 2D coordinates. The code used for the SVD procedure was based on the open source 'Python Projective Camera Model' module (author: Matej Smid, https://github.com/smidm/camera.py).

3.2.4 Establishment of a 3D body coordinate system

To allow for the analysis of the obtained 3D keypoint positions in relation to the body of the animals, a body coordinate system was created for each fly by using the three tracked body references keypoints (**see 3.2.2**). The origin of the body coordinate system was defined by the position of the ThAp and the y-axis vector y was the vector between the wing hinges and pointed towards the left body side (**Eq. 3.7**).

$$\vec{y} = lWH - rWH \tag{3.7}$$

To obtain an x-axis pointing towards the anterior direction of the body, the vector between the ThAp and the midpoint between the wing hinges was calculated at first (**Eq. 3.8**), but the resulting vector was skewed (x_{skewed}) because the wing hinges were situated ventrally in relation to the ThAp (**Figure 3.3**).

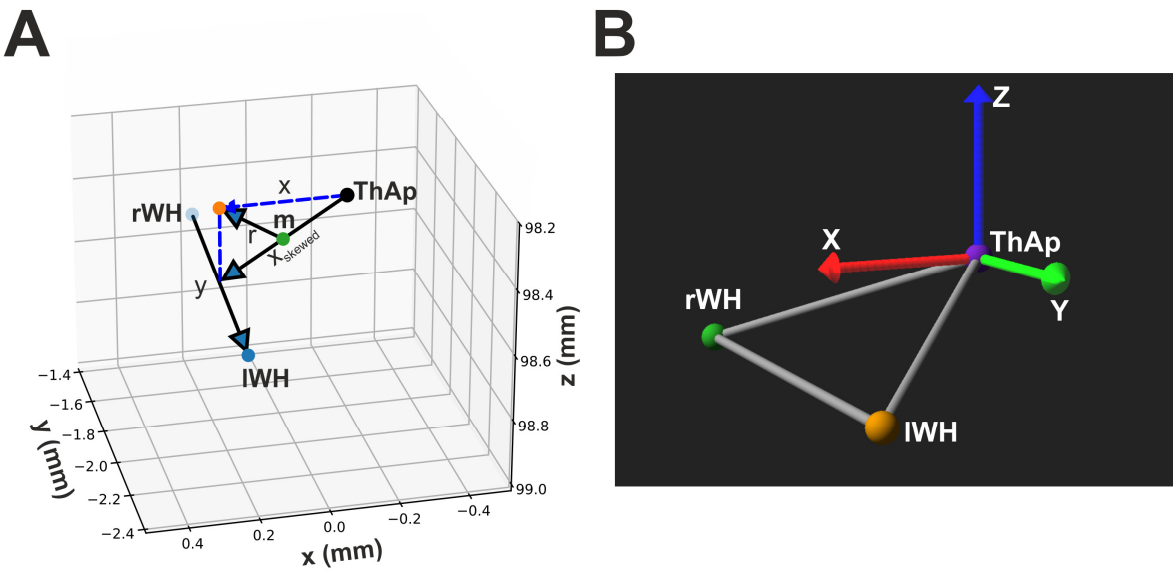

Figure 3.3. Body coordinate system. (**A**) Graph displaying the vectors used to calculate the body coordinate system axes. (**B**) Example image of the body coordinate system and the body reference keypoints.

$$\vec{x}_{skewed} = (rWH + \frac{\vec{y}}{2}) - ThAp \tag{3.8}$$

However, given that x_{skewed} is the hypotenuse of a right triangle, the adjacent leg lies on the desired x-axis. Moreover, by calculating the reflection vector from the vector between the midpoint m of x_{skewed} to the midpoint between the wing hinges, it was possible to obtain the intersection point of the adjacent and the opposite legs which in turn served to define the x-axis vector x (**Figure 3.3**). The plane of reflection was defined by the y-axis vector y and the axis vector g of the global coordinate system describing the posterior-anterior axis of the flies, i.e. the y-axis in the camera coordinate system (see **Figure 3.2**). By calculating the cross product between both vectors, the plane normal n_r was obtained and was used to determine the reflection vector r (**Eqs. 3.9**).

$$\hat{n}_r = \frac{\vec{g} \times \vec{y}}{|\vec{g} \times \vec{y}|} \tag{3.9}$$
$$\vec{r} = \vec{x}_{skewed} - 2(\vec{x}_{skewed} \cdot \hat{n}_r)\hat{n}_r$$

Afterwards, the x-axis vector x was calculated (**Eq. 3.10**). To obtain a right-handed coordinate system the cross product of the y-axis vector and the x-axis vector was calculated (**Eq. 3.11**).

$$\vec{x} = (m + \frac{\vec{r}}{2}) - ThAp \tag{3.10}$$

$$\vec{z} = \vec{Y} \times \vec{X} \tag{3.11}$$

However, the obtained axes vectors were not absolutely orthogonal due to small tracking errors of the keypoints. To correct for this, the vectors were orthonormalized by the Gram-Schmidt process (Leon et al., 2013) using a QR factorization algorithm (qr function, linalg module, NumPy). It is worth noting that, since no scaling operations were applied, the body coordinate system is in the same metric scale as the camera calibration coordinate system, i.e. in millimeters.

3.3 Results

3.3.1 Performance of automated tracking of keypoints

To evaluate the accuracy and robustness of the automated tracking of keypoints by DLC, the tracking error was analyzed, i.e. the Euclidean distance between the predicted position of a keypoint by the ResNet-50 networks and the corresponding manual annotation. Additionally, although small residual tracking errors are associated even with good tracking performance, the main objective for using automated tracking was to reduce human labor. For this, the percentage of required manual corrections based on the total number of predicted positions for each keypoint served as measure of the human workload, regardless of the magnitude of the individual misdetection.

The ResNet-50 networks were generally able to track accurately all keypoints as demonstrated by the small tracking error of the training set data (**Figure 3.4A**). For keypoints tracked in video frames of the training sets, the median error was 1.9 pixels (IQR: 1.2 pixels), 2.5 pixels (IQR: 1.1 pixels), and 1.6 pixels (IQR: 0.8 pixels) for the front, side, and hind ResNet-50 network, respectively. Furthermore, the error was smaller than 10 pixels for 98% of all keypoints in the training sets. In contrast, in video frames that the networks had never seen before and required corrections, the median error was about six to ten times higher with 11.2 pixels (IQR: 51.8 pixels), 7.2 pixels (IQR: 10.2 pixels), 15.0 pixels (IQR: 59.9 pixels) for front, side, and hind ResNet-50 network, respectively.

While all three ResNet-50 networks showed similar errors for the tracking of the same keypoint, the size of error differed for individual keypoints. The tracking error was generally larger for most leg keypoints than for the body keypoints (**Figure 3.4A**). The maximum tracking error for body keypoints, i.e. the ThAp, the wing hinges, and the antennae, ranged from 7.0 to 27.1 pixels. In contrast, the maximum tracking error for the leg keypoints ranged from 128.6 to 766.4 pixels. The largest tracking errors were found for the distal leg parts, i.e. the TiTar and the Tar, while the ThCx showed with a maximum error of 12.9 pixels a similar tracking error compared to the error observed for the body keypoints. However, the tracking error was smaller than 12 pixels for 93% of all tracked keypoints from frames which were not part of the training sets, excluding the TiTar and the Tar. While the error for the TiTar was

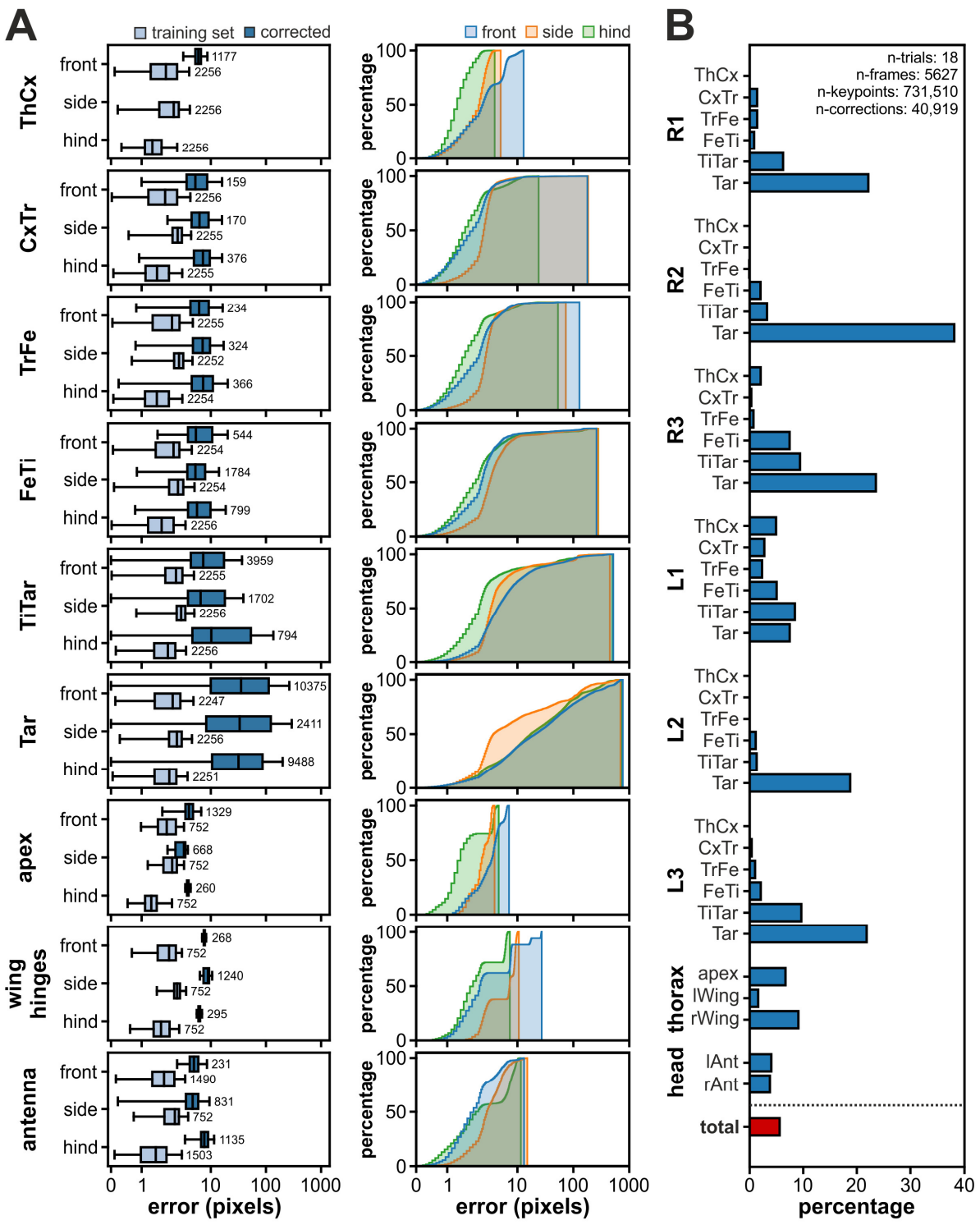

Figure 3.4. Evaluation of the tracking error. (**A**) In the left panels, the absolute error for individual tracked keypoints of the front, side, and hind DLC networks is shown for video frames of the complete training sets (light blue) and frames from videos not previously seen by the networks that required manual corrections (dark blue). Number of evaluated keypoint positions is indicated to the right to the boxplots. In the right panels, the cumulative percentage of the error distribution including errors for

the training set and corrected keypoints is shown for the front (blue), side (orange), and hind (green) networks. Note that the error is plotted on a logarithmic scale on the x-axis. (**B**) Percentage of required corrections for individual keypoints in all fly postures, i.e. video frames, analyzed in this thesis. Percentage is shown for right (R) and left (L) front, middle, and hind legs (1,2,3), for additional thorax and head markers as well as for the total amount of required corrections.

smaller than 12 pixels in at least 65% of the tracked positions analyzed, this was the case for only 30% of Tar positions. In addition, the observed large tracking inaccuracy of Tar positions was often accompanied with assignment of the Tar position to the wrong leg. For instance, the Tar for the front legs was frequently detected on the hind legs and vice versa. Nevertheless, the majority of keypoints were detected accurately in the experimental walking sequences. In total, only 5.6% of all tracked keypoints (n=731,510) in all analyzed video frames required manual corrections (**Figure 3.4B**). The frequency of required corrections for individual keypoints was, however, related to the observed tracking error for those keypoints. For instance, tracked positions for the Tar that required correction did not only show the largest error, but also 22% of all Tar positions from all six legs had to be corrected.

In summary, the ResNet-50 networks were essentially able to robustly track leg and body keypoints, even though their accuracy rate was lower for video frames not included in the respective training set. However, although very large tracking errors for individual keypoints were observed occasionally, the frequency of required manual corrections was very low. This, together with the high video processing rate of approximately 20 Hz, demonstrates the efficiency of DLC to reduce substantially the human workload for tracking leg and body keypoints in walking fruit flies.

3.3.2 Evaluation of 3D posture reconstruction

Based on the tracked 2D positions of leg and body keypoints, their 3D positions were reconstructed by triangulation (**Figure 3.5**). It was, however, challenging to evaluate the accuracy of the obtained 3D reconstruction of *Drosophila* leg postures based on the present motion capture approach since there is no real ground truth data available. Even if 2D position

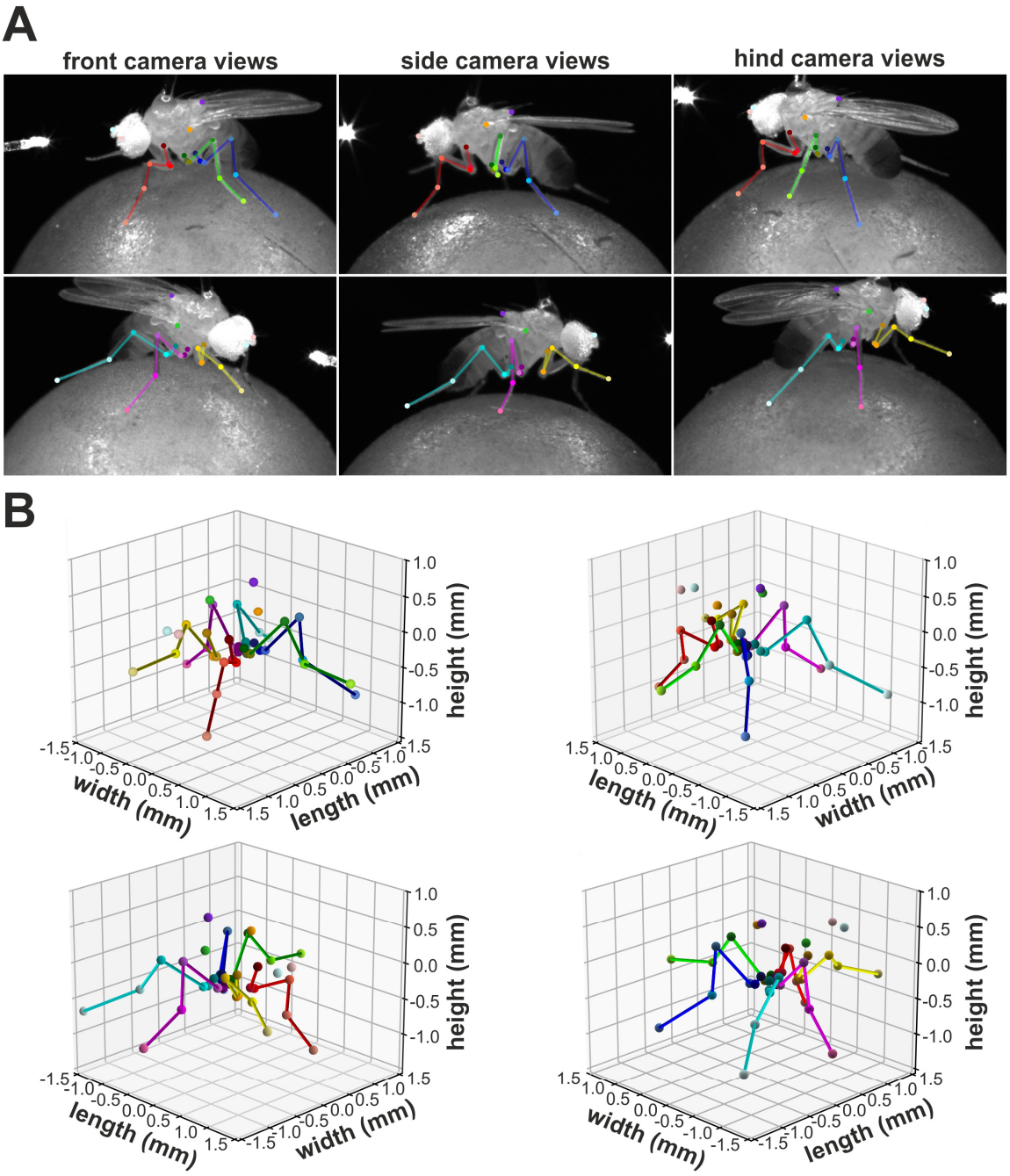

Figure 3.5. Representative example for 3D pose reconstruction. (**A**) Annotated video frames for all six camera views of the same time point. Upper and lower panels display left and right body sides of one male fly, respectively. (**B**) Corresponding 3D reconstruction from the same fly and posture from different views. Left and right panels resemble the views from the front and hind cameras, respectively. In the upper and lower panels, the left and right body sides of the animal is in the foreground, respectively.

annotated by humans would be used for comparison, there is no guarantee that the resulting 3D reconstructions would not be biased by factors such as the human observer variability, for instance. However, since the leg segments can be assumed to be rigid in *Drosophila* due to their exoskeleton, the variability of their length was used to assess the quality of 3D reconstructions. For this, the length of the coxa, trochanter, femur, tibia, and, tarsus was determined for all analyzed 3D postures by calculating the Euclidean distance between the respective connecting joints. To prevent bias by sex-specific body size differences (Carreira et al., 2009), the variability in the length of segments was separately analyzed for males and females. For the comparison of the variability of the length of segments, the coefficient of quartile variation (CQV) was used (see **2.3**).

The resulting median lengths for the analyzed segments of the female flies (**Figure 3.6**) were comparable to reported leg segment lengths for female adult flies (Lobato-Rios et al., 2022). This demonstrates that the motion capture approach used here was able to reconstruct 3D positions in the correct order of magnitude within the metric scale. In addition, ratio of the median segment length between female and male flies ranged from 0.97 to 1.03 for almost all leg segments except for the tarsus of hind legs, which showed a slightly higher ratio of 1.09, indicating that the leg segment length is very similar in both sexes. A similar range of variation in the median length was found for the most leg segments, when the right and left body side were compared. However, the median length of coxa and trochanter showed larger discrepancies between the body sides. For the coxa of the middle and hind legs, the right-left ratio of the median length ranged from 0.92 to 1.21. In addition, right-left ratio of the median length of the trochanter for all leg pairs ranged from 0.82 to 1.41 and from 0.94 to 1.31 in female and male flies, respectively.

However, the large observed discrepancy was unlikely to result from a poor 3D reconstruction, but rather emerges from the fact that the trochanter of all legs and the coxa of the middle and hind legs are relatively short compared to the other leg segments (**Figure 3.6**). The variability of the measured length of the individual segments was generally low as revealed by the small CQV which ranged from 1.35% to 10.6% for almost all segments irrespective of sex and body side. Additionally, the CQV was smaller than 5% for 85.4% of

those segments. However, the CQV for the length of the trochanter was larger and ranged from 11.1% to 31.6%, which was again explainable by the small length of this segment.

Taken together, these findings show that 3D reconstruction based on the tracked 2D keypoints was reliably achieved. Although the observed differences in the lengths of segments indicate that tracked keypoint positions "wobble" around its true position from frame to frame, the resulting impact for subsequent kinematic analysis can be considered as neglectable.

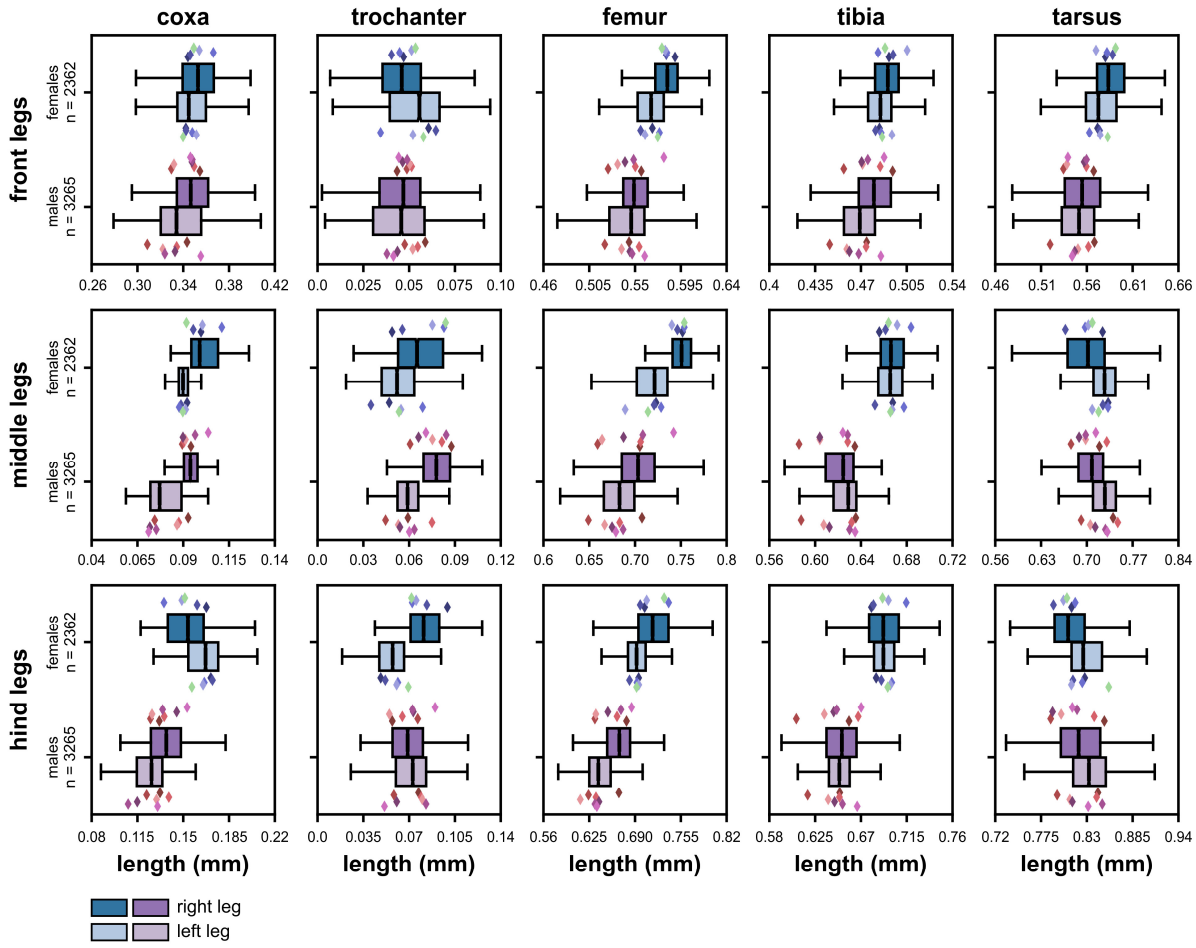

Figure 3.6. Evaluation of leg segment length. Due to sex-specific differences in body sizes, separated boxplots show data for females (N = 5, upper boxplots) and males (N = 7, lower boxplots). Boxplots for right and left legs are darker and lighter colored, respectively. Colored diamonds represent the median of individual flies. The total number (n) of analyzed postures is indicated in the labels of the y-axis.

3.4 Discussion

The motion capture system implemented here allows for the robust and reliable 3D reconstruction of leg postures from walking fruit flies. The system runs stably with six cameras recording at a high frame capturing rate of 400 Hz and a high video resolution of 896 x 540 pixels. While other reported 3D motion capture systems for *Drosophila* walking have a similar spatial resolution, these systems achieve only 100 Hz (Günel et al., 2019) or 300 Hz (Karashchuk et al., 2021). However, a high temporal resolution is required to adequately capture the behavior of rapid moving animals such as *Drosophila*. For instance, the mean leg swing duration of fruit flies is about 31 ms (Szczecinski et al., 2018). Since the motion capture system presented here acquires a video frame every 2.5 ms, the time course of leg movements during swing phases are not only captured more accurately, but also the timing of transitions from swing to stance and vice versa can be determined more precisely.

The main intention for using automated tracking by DLC was to reduce the human workload. However, to obtain high-quality data for subsequent kinematic modeling (see **chapter 4**), all tracked keypoints of the analyzed data set were manually validated afterwards and this work did not aim to optimize the performance of the ResNet-50 networks. Nevertheless, the trained networks achieved a high tracking accuracy as demonstrated by the fact that less than 6% of keypoints had to be corrected manually and the corresponding tracking error was smaller than 12 pixels for the majority of them. This level in error is comparable to other pose estimation approaches used for *Drosophila* so far (Günel et al., 2019; Karashchuk et al., 2021; Mathis et al., 2018) and is believed to represent the current limit of accuracy for markerless tracking (Karashchuk et al., 2021).

However, the correction rate and tracking error were much larger for the most distal leg parts, i.e. the TiTar and Tar. Günel et al. (2019) also reported larger tracking errors for the Tar, which they attributed to occlusions from the spherical treadmill and a higher positional variance. In addition, the ResNet-50 networks employed here often assigned the TiTar or Tar to the correct limb location, but to the wrong leg. Although each network was trained to detect keypoints in video frames from an equivalent camera position for both the left and right body side, i.e. the input video frames were basically mirrored (see **Figure 3.5A**), this implies that the

networks failed to learn correctly the spatial relationship between these keypoints and the general body orientation. That further means that the networks must be optimized to allow for robust tracking for large data sets in the future without increasing the workload by human validation to an unreasonable level.

The simplest approach to improve the robustness of deep learning-based pose estimation algorithms is to retrain the networks with the video frames that required manual corrections, commonly referred to as active learning (Mathis et al., 2018; Nath et al., 2019). In general, a diverse training set is the key to prevent overfitting of a CNN. Overfitting refers to the fact that, although the network learned to efficiently track keypoints in video frames of the training set, it fails to track these keypoints in new and previously unseen frames since it learned rather specific features of the training set instead of the general pattern of the keypoints (Mathis et al., 2020; Nath et al., 2019). Since frames that exhibit false detections obviously contain atypical poses or image features with respect to the current training set, the generalizability of the networks benefits particularly from adding these frames to the training set. The training set can be further enriched by data augmentation techniques (Shorten and Khoshgoftaar, 2019). Although the default data augmentation settings from DLC were already used for the training of the current networks (see **3.2.2**), there are several different algorithms and parameters available which can affect the final tracking efficiency (Mathis et al., 2020; Nath et al., 2019). In addition, the wobble of keypoint positions by small tracking errors can be also reduced by applying filters to the tracked data. Karashuck et al. (2021) examined the effects of multiple filter algorithms on 2D and 3D keypoint positions and found a significant improvement of their pose estimation results.

Nevertheless, a general challenge for the robustness of the approach presented here for 3D motion capture might be that CNNs only learn to detect keypoints in 2D video frames and reconstruction of the 3D positions is achieved by triangulation from 2D positions of multiple views afterwards. A recent and very promising approach for 3D pose estimation of animals is to train CNNs to directly predict the 3D locations of keypoints, without the detour of first detecting 2D positions. For instance, DANNCE uses projective geometry to construct a 3D feature space that allows training of a CNN with shared features across multiple camera views

and results in a 30-fold higher efficiency for 3D pose reconstruction compared to current triangulation approaches (Dunn et al., 2021).

However, it is also questionable whether automated tracking algorithms will ever reach 100% reliability, i.e. the tracked positions show only very small errors which can be interpreted as noise and no further human monitoring of the tracked data set is required. Therefore, it would be also important to develop user-friendly and efficient validation pipelines for motion capture data. One approach to this problem is to automate the identification of misdetections. Several strategies were already proposed to facilitate the detection of frames containing such tracking outliers. Straight forward methods rely on identifying tracked keypoints for which the estimation likelihood of the networks is low or which exhibit large position jumps in consecutive video frames (Nath et al., 2019). It is, however, challenging to define efficient thresholds for these methods because low likelihoods could also indicate occlusions by other moving body parts or the velocity of body parts is not constant, e.g. the tarsus tip moves typically faster during the swing phase compared to the stance phase. More sophisticated methods exploit the geometric relationship between keypoints to detect outliers or to reduce tracking errors. For instance, Graving et al. (2019) trained a CNN to predict not only the locations of keypoints, but also the connecting segments between them. Thus, the additional information of the resulting likelihood maps can be used to also identify tracking outliers. Another approach uses a probabilistic graphical model based on pictorial structures to infer the most likely 3D pose from all connected keypoints of a specific body part (Günel et al., 2019) and discrepancies between the inferred and tracked poses are indicative of misdetections.

Chapter 4

Decomposition of 3D joint angles by kinematic modeling of *Drosophila* legs

4.1 Introduction

Since biological legs typically have more joints and/or more degrees of freedom (DOF), i.e. independent directions of movements, than required for pure walking, a detailed kinematic analysis is required to understand the demands on the underlying motor control system. The movements of limbs emerge from joint torques which cause angular motion of the individual segments of the limb about the respective joint rotational axes. Thus, joint angles describing the extent of these rotations are a natural choice to measure the kinematics of limbs. Moreover, the nervous system generates muscle activity to drive angular joint movements and processes proprioceptive sensory feedback from these movements to modify the muscle commands to accomplish the desired motor task (Büschges, 2005; Nielsen, 2003; Nishikawa et al., 2007). Therefore, changes in joint angles are also thought to be better correlated to the underlying neuronal activity than changes in the position of the limb segments themselves (Bender et al., 2010).

Although leg joint angles for *Drosophila* can in principle be derived directly from 3D reconstructions of markerless motion capture data (Günel et al., 2019; Karashchuk et al., 2021; Lobato-Rios et al., 2022), there are limitations regarding the accuracy and interpretability of the resulting angles due to the way markerless tracking is usually implemented and subsequent angle calculations are performed. Typically, only one keypoint per joint is tracked during motion capture and the angle between two segments is calculated by the arccosine of the dot product from the vectors of both segments which are defined by three keypoints, i.e. the proximal end of the first segment, the joint of interest, and the distal end of the second segment (Karashchuk et al., 2021). Although this method is straight-forward and intuitive, one has to consider that the resulting angle is derived from a plane formed by the positions of

the keypoints and thus the rotational axis is always strictly orthogonal to this plane. However, not only can the wobble of tracked markers (see **3.3.2**) affect the formed plane and thus the spatial orientation of the rotational axis from video frame to video frame, but more importantly, the real anatomical joint rotational axis might be skewed with respect to the segments. The situation becomes even more complex when considering joints with two or three DOFs such as e.g. for the thorax-coxa joint in insects, which is a spherical joint with three DOFs (Hughes, 1952; Snodgrass, 1935). To solve this problem of determining three angles from only one keypoint, i.e. the thorax-coxa joint, researchers typically construct a body coordinate system and use it either to calculate angles from the projections of the coxa on the individual body planes (Lobato-Rios et al., 2022) or to calculate an Euler angle sequence to fit the body coordinate system to the coxa (Bender et al., 2010; Karashchuk et al., 2021). Although this results in conceptually intuitive joint angles which represent movements in relation to the body, these methods again do not take into account real anatomical joint axes. Additionally, projection angles should generally not be considered as true 3D angles (Robertson et al., 2014) and they yield kinematically useful results only under a limited number of conditions (Woltring, 1991).

These issues can be circumvented by using a local Cartesian coordinate system (LCS) for each joint and calculating the orientation angles between two subsequent LCSs. For this, at least three markers are attached to each segment in a specific non-collinear arrangement that allows for the alignment of an LCS to the anatomical joint axis (Robertson et al., 2014). Afterwards, the orientation angles are calculated, which represent basically a Euler or Cardan sequence describing the required rotations from each axis of the first LCS to match its counterpart from the next LCS. This method is widely used in studies of human kinematics (Colyer et al., 2018; Robertson et al., 2014) and it has been shown to perform better than markerless pose estimation, particularly for rotations about the longitudinal axis of segments (Ceseracciu et al., 2014; Colyer et al., 2018; Mathis et al., 2020). However, since the methodological difference is not the use of attached markers per se, but simply the number of tracked locations on the segments, pose estimation networks could in principle be also trained to detect three or more keypoints for each segment. Although this would allow to construct an LCS for each joint, clear visual distinguishable anatomical landmarks on each segment are required. These might not exist or, in the case of *Drosophila*, cannot be recognized in current video recordings due to

limited optical magnification. In addition, even though Euler or Cardan angles are widely used in kinematic studies, it must be mentioned that they are not unique because the resulting angles can be significantly different depending on which axes sequence is used for their calculation (Crawford et al., 1996; Crawford et al., 1999; Woltring, 1991). Therefore, it is somewhat questionable whether Euler/Cardan angles represent the true occurring movements of limbs or just an equivalent path of motion (Crawford et al., 1999).

Kinematic modeling of articulated limbs was originally introduced by engineers to facilitate the control of robotic arms (Craig, 2005; Spong et al., 2020a), but was adopted in the biomechanical field due to the shared problem of comprehending limb motions. Under the assumption that a limb is a series of rigid segments interconnected by joints, a mathematical representation of the limb, called kinematic chain, can be constructed and movements of segments about the joints are introduced by changing the angles of the related joint DOFs in the kinematic chain. For this, however, two further mathematical problems need to be addressed: forward and inverse kinematics. Forward kinematics deals with the geometrical problem of computing the position and orientation of the end-effector of the kinematic chain for a given set of joint angles. Inverse kinematic approaches, on the other hand, attempt to solve the problem of determining an appropriated joint angle configuration that results in a given position and orientation of the end-effector (Craig, 2005; Singh et al., 2021; Spong et al., 2020a). In contrast to the computation of forward kinematics, which is well-defined and straight-forward because there is always a unique solution, finding solutions for inverse kinematics is more complicated. Particularly for kinematic chains with redundant DOFs, there might be multiple, or even infinitely many, joint configurations that lead to the very same end-effector position (Aristidou et al., 2018). For kinematic studies of biological limbs, this issue can be mitigated by using tracked joint positions as additional constraints for the computation of the joint angles. Under the term multibody kinematics optimization, this strategy has gained more attention in recent decades to alleviate soft tissue artefacts in human kinematic studies (Begon et al., 2018). Since markers are usually attached to the skin of the probands, movements of the soft tissue between the markers and the bones lead to errors that can have the same order of magnitude as the underlying joint motions (Camomilla et al., 2017). To compensate for this, a kinematic model of the bones of a limb of interest is constructed and the distance between the tracked and the model-derived markers is minimized by applying a

global optimization algorithm (Begon et al., 2018; Lu and O'Connor, 1999). In other words, the forward kinematics of the model is iteratively optimized until a joint configuration is found that results in a model posture that closely matches the tracked marker positions. Since the structure of the kinematic chain, i.e. the length of segments and the joint rotational axes, is preserved during movements, it is assumed that the resulting model posture is a better representation of the orientation of the bones than the posture obtained by the tracked markers alone. Another advantage of the resulting joint angles is that these are directly related to the anatomical joint rotational axes used in the model.

Although soft-tissue artefacts do not occur in insects due to their exoskeleton, kinematic modeling is promising for circumventing the aforementioned issue of having too few tracked joint keypoints per leg segment for computation of real 3D angles. In fact, several kinematic leg models were implemented in the last decades to study locomotion of the stick insect (Dallmann et al., 2016; Theunissen and Dürr, 2013; Zakotnik et al., 2004), the cockroach (Szczecinski et al., 2014), the cricket (Petrou and Webb, 2012), the ant (Arroyave-Tobon et al., 2022), and more recently *Drosophila* (Goldsmith et al., 2022; Lobato-Rios et al., 2022). It should be kept in mind, however, that even if a model can very closely match the tracked posture of an animal leg, the resulting joint angles are highly dependent on the design decisions of the model, i.e. the location of the joints, the number of DOFs of each joint, and the orientation of their rotational axes (Begon et al., 2018). This also means that a meaningful kinematic model must be based on detailed morphological knowledge of the joints, which is challenging in insects due to their small size. Thus, most insect leg models relied on assumptions from previous kinematic studies and/or anatomical descriptions from morphological studies. However, extremely detailed 3D body models of insects can now be created due to recent advances in micro-computed tomography (μCT), which allow the precise extraction of joint condyle positions (Arroyave-Tobon et al., 2022; Blanke et al., 2017).

Nevertheless, even though the construction of detailed kinematic model of *Drosophila* legs can be facilitated by μCT data, there is also a huge lack of knowledge about the functionality of joints and their DOFs in *Drosophila*. For example, the functional role of the trochanter-femur joint in *Drosophila* is controversial, with opinions ranging from being fused and immobile (Lobato-Rios et al., 2022; Sink, 2006) to at least limited mobility (Feng et al., 2020).

In this chapter, to decompose the leg joint kinematics of *Drosophila*, at first a 3D kinematic leg model based on anatomical landmarks, i.e. the joint condyles, was constructed and the number of required DOFs to model forward walking was determined by comparing models with different DOF configurations. Afterwards, the joint angle time courses were evaluated from the model with the most plausible DOF configuration of the kinematic chains.

4.2 Material and methods

4.2.1 Kinematic leg model based on anatomical landmarks

To model the motion of articulated limbs, a mathematical representation of the limbs must be formulated. In this thesis, all six legs were modeled as kinematic chains, consisting of multiple joints interconnected by rigid segments of specified lengths in a Cartesian coordinate system. Each kinematic leg chain consisted of a thorax-coxa joint (ThCx), coxa-trochanter joint (CxTr), trochanter-femur joint (TrFe), femur-tibia joint (FeTi), tibia-tarsus joint (TiTar) and the tarsus tip (Tar). The joints were linked by five leg segments: the coxa (CX), trochanter (TR), femur (FE), tibia (TI), and tarsus (TAR). To obtain an anatomical correct model, joint rotational axes (for method see: Blanke et al., 2017) and leg segment lengths were extracted from a μCT scan of a single adult female wild-type *Drosophila melanogaster* specimen which was acquired in a previous study (Dinges et al., 2021) (**Figure 4.1A**). Joint rotational axes and positions were derived from the vector between the joint condyles and its center, respectively. Leg segments were defined as the vector between consecutive joint positions or tarsus tip position. Due to bilateral symmetry of the insect bauplan, the front, middle, and hind leg of the right body side were analyzed and positions were mirrored to the left side. Since the actual DOFs in leg joint of *Drosophila* are not yet known, each model joint was defined as spherical joint equipped with three DOFs, namely yaw, pitch, and roll (**Figure 4.1B**). The yaw axis was defined by the rotational axis of the joint. To describe longitudinal rotations, i.e. rotations around the leg segment, the segment vector was used to specify the roll axis. The pitch axis was introduced to complete the full range of motion of a spherical joint and was defined by the cross product of the yaw and roll axes. Importantly, single DOFs could be set as movable or fixed, so that they could or could not contribute to leg movements, respectively.

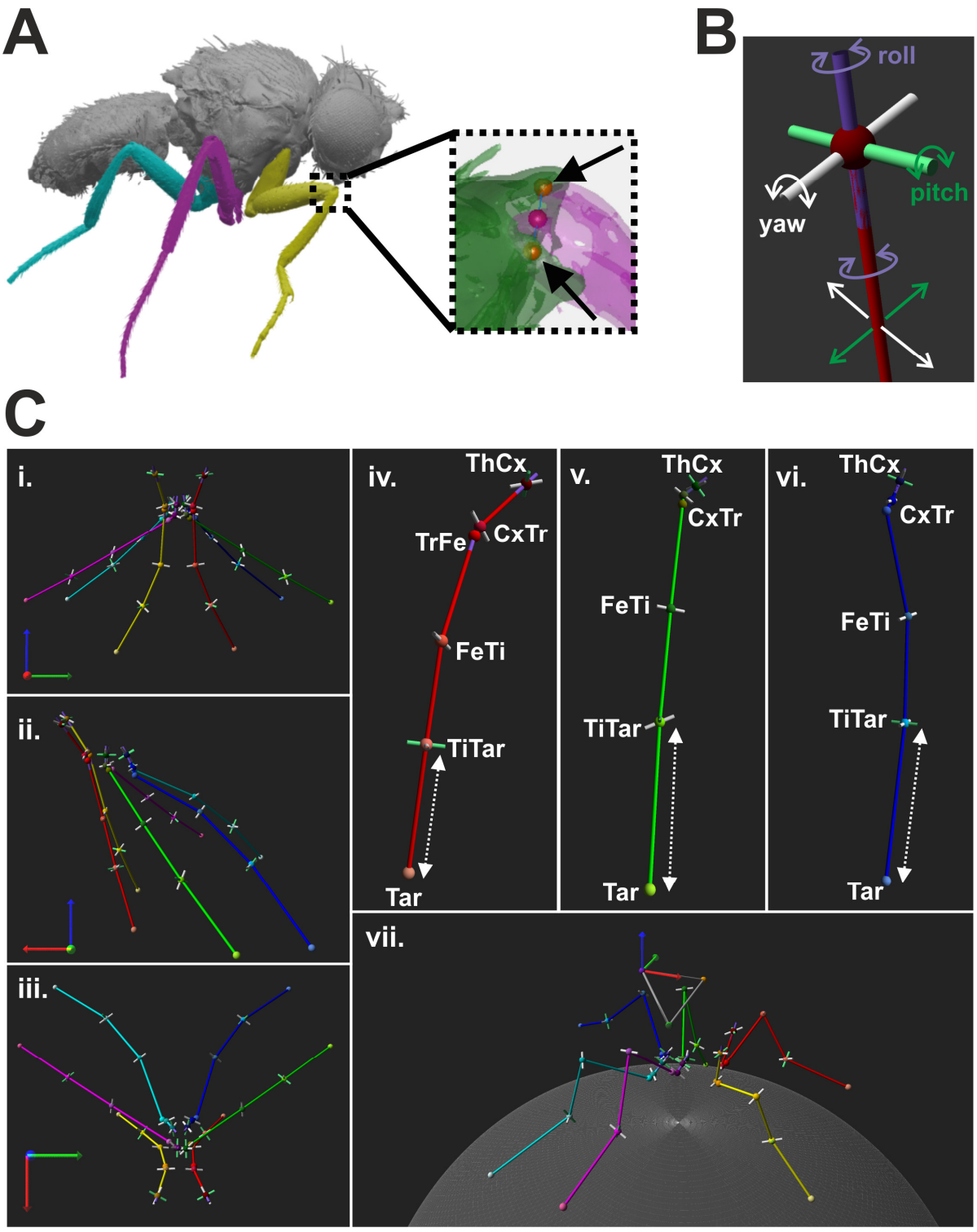

Figure 4.1. Kinematic leg model. (**A**) Image of μCT scan used to extract the joint condyles for creating the model. Example for joint condyles of the femur-tibia (FeTi) is shown in the dashed box. Black arrows point to the joint condyles which are displayed as orange spheres. The magenta-colored sphere indicates the position of the joint center. (**B**) A model joint with three DOFs, i.e. yaw, pitch, roll. Movement directions by angle changes in the DOFs are indicated by arrows of the same color. (**C**) Images of the model. The initial posture of the model is shown in front (**i.**), side (**ii.**), and top (**iii.**) view.

Close-up view on the left front (**iv.**), middle (**v.**), and hind (**vi.**) leg display the joint positions and the rotational axes of the DOFs for each joint. Note that the TrFe-roll was only movable in the front legs of the final model, but not in the reference model. Dashed arrows indicate that the tarsus length was variable in the model (see text for details). An example walking posture of the model is shown in **vii**. 3D coordinate systems indicate directions. The red (x-axis), green (y-axis), and blue (z-axis) arrows point towards anterior, left, and dorsal with respect to the fly body.

Fixing of DOFs was achieved by excluding them from global optimization during inverse kinematics or omitting updating the respective joint angles generated by inverse kinematics (see **4.2.3**). Although it was not assumed that all leg joints in *Drosophila* have three DOFs, this approach facilitated the identification of the actual DOF configuration of the legs. Additionally, thorax posterior scutellum apex, left wing hinge, and right wing hinge, were extracted from the μCT scan data. These positions were used for constructing a body coordinate system and for adapting the model to the motion capture data of individual flies (see **3.2.4**). Positions of joint condyles from μCT data were provided by Prof. Dr. Alexander Blanke.

4.2.2 Forward kinematics of kinematic leg chains

To solve the forward kinematics of the leg chains, i.e. determining the position and orientation of each joint and the tarsus tip by a given set of joint angles, DOFs of joints and the tarsus tip were represented by LCSs which were constructed according to the standard Denavit-Hartenberg (D-H) convention (Denavit and Hartenberg, 1955; Lynch and Park, 2017; Spong et al., 2020b). The base concept is that the geometrical relationship between LCSs of two consecutive DOFs can be described by a homogeneous transformation matrix. As a result, the position of any point expressed in an LCS can be considered as constant and its coordinates in the global coordinate system depends on orientation and position of the LCS. Moreover, since the position and orientation of each LCS of a DOF depends on the LCS of the preceding DOF in the chain, joint movements are propagated through the chain by changing the joint angle parameter in the respective transformation matrix. The product of transformation

matrices from all preceding DOFs to any joint or the end effector of the kinematic chain (**Eq. 4.1**) gives eventually the position in coordinates of the first LCS in the chain.

$$T_n^0 = \prod_{i=1}^{n} T_i^{i-1} \tag{4.1}$$

The D-H convention provides specific rules for constructing LCSs:

1) The z-axis is the rotational axes of the respective DOF.
2) The x-axis and the origin of the LCS depend on the relationship between the z-axis and the rotational axis of the previous DOF:
    a. There is no previous DOF for the first DOF in the kinematic chain. In this case, the x-axis and the origin of the LCS can be chosen arbitrarily as long as the origin is a point on the z-axis and the x-axis is perpendicular to the z-axis.
    b. When both axes are not coplanar, only a unique common normal, i.e. a line that orthogonally intersects the z-axis and the rotational axis of the previous DOF, exists. The x-axis coincides with the common normal and points towards the next DOF. The origin is determined by the point of intersection on the z-axis.
    c. When both axes intersect, the x-axis is defined by the normal of the plane formed by the z-axis and the rotational axis of the previous DOF. The origin is the point of intersection of both axes. The direction of the x-axis can be chosen arbitrarily in this situation.
    d. When both axes are parallel to each other, there is no single common normal, but infinitely many. In this case, the x-axis can be derived from the common normal that passes through the joint position of the respective DOF and consequently the origin is the joint position.
3) The y-axis is defined by the cross product of the z-axis and the x-axis to form a right-handed LCS.

When assigning LCSs in this manner, each transformation matrix can be formulated with the four D-H parameters (**Eq. 4.2**):

1) The joint angle (θ) is the angle between x-axis and the x-axis of the previous DOF about the z-axis of the previous DOF. It therefore describes the required rotation about the z-axis of the previous DOF to align both x-axes. Additionally, joint movements are achieved by adding the desired angle of rotation to the initial joint angle.
2) The link twist (α) is the angle between the z-axis and the z-axis of the previous DOF about the x-axis. It therefore describes the required rotation about the x-axis to align both z-axes.
3) The link length (r) is the distance between the points of intersection of the common normal with the z-axis and the z-axis of the previous DOF. In case of intersecting DOF axes, the link length can be set to zero.
4) The link offset (d) is the distance between the origin and the intersection point of the common normal on the z-axis of the previous DOF. In case of intersecting DOF axes, the link length can be set to zero.

$$T_i^{i-1} = \begin{bmatrix} \cos\theta & -\sin\theta\cos\alpha & \sin\theta\sin\alpha & r\cos\theta \\ \sin\theta & \cos\theta\cos\alpha & -cos\theta\sin\alpha & r\sin\theta \\ 0 & \sin\alpha & \cos\alpha & d \\ 0 & 0 & 0 & 1 \end{bmatrix} \tag{4.2}$$

In the present leg model, the sequence of DOFs was yaw, pitch, and roll for each leg joint. LCSs of the DOFs and the D-H parameters for transformations from yaw to pitch, pitch to roll, and roll to the yaw LCS of the next joint were derived iteratively from the positions of joint condyles of a joint (J_n) and its following joint (J_{n+1}). At first, the z-axes (Z-hat) for each DOF were defined (**Eqs. 4.3**).

$$\begin{aligned} yaw_{\vec{Z}_{J_n}} &= condyle2_{J_n} - condyle1_{J_n} \\ yaw_{\hat{Z}_{J_n}} &= \frac{yaw_{\vec{Z}_{J_n}}}{|yaw_{\vec{Z}_{J_n}}|} \\ roll_{\vec{Z}_{J_n}} &= center_{J_{n+1}} - center_{J_n} \\ roll_{\hat{Z}_{J_n}} &= \frac{roll_{\vec{Z}_{J_n}}}{|roll_{\vec{Z}_{J_n}}|} \end{aligned} \tag{4.3}$$

$$pitch_{\vec{Z}_{J_n}} = yaw_{\hat{Z}_{J_n}} \times roll_{\hat{Z}_{J_n}}$$
$$pitch_{\hat{Z}_{J_n}} = \frac{pitch_{\vec{Z}_{J_n}}}{|pitch_{\vec{Z}_{J_n}}|}$$

Since z-axes of all DOFs of a joint intersect by definition, the origin of the yaw-LCS was also used for all subsequent LCSs. The x-axes (X-hat) of the pitch and roll LCSs were derived from the cross product of the respective z-axes (**Eqs. 4.4**).

$$\begin{aligned} pitch_{\vec{X}_{J_n}} &= yaw_{\hat{Z}_{J_n}} \times pitch_{\hat{Z}_{J_n}} \\ pitch_{\hat{X}_{J_n}} &= \frac{pitch_{\vec{X}_{J_n}}}{|pitch_{\vec{X}_{J_n}}|} \\ roll_{\vec{X}_{J_n}} &= pitch_{\hat{Z}_{J_n}} \times roll_{\hat{Z}_{J_n}} \\ roll_{\hat{X}_{J_n}} &= \frac{roll_{\vec{X}_{J_n}}}{|roll_{\vec{X}_{J_n}}|} \end{aligned} \tag{4.4}$$

In contrast, the origin and x-axis of the yaw-LCS had to be defined in relation to the roll-LCS of the preceding joint. Since both rotational axes were always skew, i.e. they were non-coplanar and non-parallel, the intersection points (c_1, c_2) of the common normal (n) of both z-axes were calculated and used to define the x-axis of the yaw-LCS of J_{n+1} (**Eq. 4.5**).

$$\begin{aligned} \vec{n} &= roll_{\hat{X}_{J_n}} \times yaw_{\hat{Z}_{J_{n+1}}} \\ \vec{n}_{roll_{J_n}} &= roll_{\hat{X}_{J_n}} \times \vec{n} \\ \vec{n}_{yaw_{J_{n+1}}} &= yaw_{\hat{Z}_{J_{n+1}}} \times \vec{n} \\ c_1 &= center_{J_n} + \frac{(center_{J_{n+1}} - center_{J_n}) \cdot \vec{n}_{yaw_{J_{n+1}}}}{roll_{\hat{X}_{J_n}} \cdot \vec{n}_{yaw_{J_{n+1}}}} roll_{\hat{X}_{J_n}} \\ c_2 &= center_{J_{n+1}} + \frac{(center_{J_{n+1}} - center_{J_n}) \cdot \vec{n}_{roll_{J_n}}}{yaw_{\hat{Z}_{J_{n+1}}} \cdot \vec{n}_{roll_{J_n}}} yaw_{\hat{Z}_{J_{n+1}}} \\ yaw_{\hat{X}_{J_{n+1}}} &= \frac{c_2 - c_1}{|c_2 - c_1|} \end{aligned} \tag{4.5}$$

There were two LCSs in the kinematic leg chains which could not be defined by this approach:

1) The LCS of ThCx-yaw was the first LCS in the chain and thus it did not have a preceding roll-LCS. Therefore, the x-axis was defined by the cross product of its z-axis

and the x-axis of the body coordinate system and the origin was set to the joint center (**Eq. 4.6)**.

2) Since the tarsus tip was the end effector of the kinematic chain, it did not have a rotational axis. The TiTar-roll LCS was duplicated and its origin was translated to the tarsus tip position. The intersection point c_2 was the tarsus tip position and c_1 was the point on the TiTar-yaw z-axis with the smallest distance to the tarsus tip position. The position of c_1 was derived by the facts that the z-axis and the vector between c_1 and c_2 are perpendicular to each other, i.e. their dot product must be zero, and that c_1 is a point on the z-axis. This allowed to solve for c_1 by substituting c_1 with the line equation for the z-axis in the dot product calculation to solve for λ and to use the resulting λ in the line equation (**Eqs. 4.7**).

$$yaw_{\vec{X}_{ThCx}} = \begin{bmatrix} 1 \\ 0 \\ 0 \end{bmatrix} \times yaw_{\hat{Z}_{ThCx}} \tag{4.6}$$

$$yaw_{\hat{X}_{ThCx}} = \frac{yaw_{\vec{X}_{ThCx}}}{|yaw_{\vec{X}_{ThCx}}|}$$

$$\begin{aligned} c_1 &= center_{TiTar} + \lambda * yaw_{\hat{Z}_{TiTar}} \\ 0 &= yaw_{\hat{Z}_{TiTar}} \cdot (c_2 - c_1) \\ 0 &= yaw_{\hat{Z}_{TiTar}} \cdot (c_2 - (center_{TiTar} + \lambda * yaw_{\hat{Z}_{TiTar}})) \end{aligned} \tag{4.7}$$

Y-axes (Y-hat) of each LCS were based on the cross product of the z-axis and the x-axes of the respective LCS (**Eq. 4.8**).

$$\hat{Y} = \frac{\hat{Z} \times \hat{X}}{|\hat{Z} \times \hat{X}|} \tag{4.8}$$

After LCSs of the kinematic chain were constructed, the D-H parameters were calculated from two successive DOF-LCSs (**Eqs. 4.9**). Since both θ and α described the required rotational angle between two axes about a third rotational axis, they were calculated by constructing two planes (Π_1: 1st axis x 3rd axis, Π_2: 2nd axis x 3rd axis) and determining the angle between

their plane normal vectors. The parameters d and r were set to zero when both z-axes intersected or otherwise had to be calculated using the common normal.

$$\theta = atan2(\frac{|(\hat{X}_n \times \hat{Z}_n) \times (\hat{X}_{n+1} \times \hat{Z}_n)|}{(\hat{X}_n \times \hat{Z}_n) \cdot (\hat{X}_{n+1} \times \hat{Z}_n)} \tag{4.9}$$

$$\theta = \begin{cases} -\theta, & \text{if } (\hat{X}_n \times \hat{Z}_n) \times (\hat{X}_{n+1} \times \hat{Z}_n) \cdot \hat{Z}_n < 0 \\ \theta, & \text{otherwise} \end{cases}$$

$$\alpha = atan2(\frac{|(\hat{Z}_n \times \hat{X}_{n+1}) \times (\hat{Z}_{n+1} \times \hat{X}_{n+1})|}{(\hat{Z}_n \times \hat{X}_{n+1}) \cdot (\hat{Z}_{n+1} \times \hat{X}_{n+1})}$$

$$\alpha = \begin{cases} -\alpha, & \text{if } (\hat{Z}_n \times \hat{X}_{n+1}) \times (\hat{Z}_{n+1} \times \hat{X}_{n+1}) \cdot \hat{X}_{n+1} < 0 \\ \alpha, & \text{otherwise} \end{cases}$$

$$d = \begin{cases} 0, & \text{if } \hat{Z}_n \cap \hat{Z}_{n+1} \\ |c_1 - origin_n|, & \text{otherwise} \end{cases}$$

$$r = \begin{cases} 0, & \text{if } \hat{Z}_n \cap \hat{Z}_{n+1} \\ |c_2 - c_1|, & \text{otherwise} \end{cases}$$

Importantly, the origin of a LCS must be on the joint rotational axis but is not necessarily the joint center according to the D-H convention, joint positions (x',y',z') were stored in coordinates of the yaw-LCS of the respective joint. To calculate the body coordinates of each joint (x,y,z), its position in the joint-yaw LCS was multiplied by the product of all preceding transformation matrices (T) in the kinematic chain and the coordinate space transformation matrix B (**Eq. 4.10**) derived from the ThCX-yaw LCS (**Eq. 4.11**).

$$\begin{bmatrix} x \\ y \\ z \\ 1 \end{bmatrix} = BT \begin{bmatrix} x' \\ y' \\ z' \\ 1 \end{bmatrix} \tag{4.10}$$

$$B = \begin{bmatrix} \hat{X}_{ThCx-yaw_x} & \hat{Y}_{ThCx-yaw_x} & \hat{Z}_{ThCx-yaw_x} & origin_{ThCx-yaw_x} \\ \hat{X}_{ThCx-yaw_y} & \hat{Y}_{ThCx-yaw_y} & \hat{Z}_{ThCx-yaw_y} & origin_{ThCx-yaw_y} \\ \hat{X}_{ThCx-yaw_z} & \hat{Y}_{ThCx-yaw_z} & \hat{Z}_{ThCx-yaw_z} & origin_{ThCx-yaw_z} \\ 0 & 0 & 0 & 1 \end{bmatrix} \tag{4.11}$$

Since the resulting posture of the model was predetermined by the posture of the legs in the μCT scan, further adjustments were made to obtain a reference default posture (**Figure 4.1C**) which facilitated the interpretation of the resulting model joint angles. For this, the model legs were straightened by manually adjusting the angles of the yaw-DOFs. A classical T-pose, as commonly used in computer animation, was not possible because this would have required additional adjustments of the pitch and roll DOF orientations. This, however, would have disrupted the anatomical relationship between leg segments when these DOFs were immobile in the model.

4.2.3 Inverse kinematics by global optimization

To determine the joint angle configurations of leg poses that the animals adopted during walking, the kinematic leg chains were fitted to motion capture data of walking sequences. For this, forward kinematics of the leg chains were optimized by using an iterative conjugate gradient descent approach that minimized the sum of squared distances between tracked and model-derived keypoint positions. For this purpose, a nonlinear trust-region reflective algorithm (Branch et al., 1999) was applied (least_squares function, SciPy optimization package version 1.6.2, The SciPy community). Termination conditions for changes in the cost function, the resulting joint angles, and the norm of the gradient were set to 10^{-3} and the maximum number of iterations was 100-times the number of moveable DOFs in the used model. These conditions were validated with a smaller subset of leg postures (see **4.2.6**) and showed costs of final solutions that were comparable to more strictly defined termination criteria, but at a 4.8-times higher computational speed. Joint angle constraints (**Table 4.1**) were introduced to prevent solutions that result in unnatural leg postures. Since the actual angular ranges of leg joints in *Drosophila* are not known, joint constraints were empirically adjusted to ensure an appropriated model fit, but did not result in solutions that reached the range limits. Pitch DOFs were generally restricted to a range of 170° to prevent gimbal lock, i.e. the loss of one DOF of the joint when the pitch and yaw rotational axes are aligned in parallel. In contrast, angular ranges for yaw and roll DOFs were stepwise restricted until unnatural leg poses did not occur. The cost function (**Eq. 4.12**) based on the distances between the CxTr, TrFe, FeTi, TiTar, and Tar positions (P) of the model and their motion captured counterparts. Initial

experiments showed that weighting (w) the distances between TrFe, FeTi, and TiTar positions by 1.5, 2.0, and 1.5, respectively, improved the model fit for front legs, but was not required for inverse kinematics of middle and hind legs.

$$costs = \sum_{i=1}^{n} w_i |(P_{motion-captured_i} - P_{model_i})|^2 \tag{4.12}$$

For each motion captured walking sequence, an initial estimate of model positions was determined by individually optimizing each model joint angle to fit the respective model joint position with its corresponding motion captured position for the first leg poses in a walking sequence. This reduced the chance that the subsequent global optimization procedure was directed to an imperfect local minimum. Afterwards, the optimization algorithm was applied globally, i.e. all model joint angles were optimized simultaneously to fit the model leg positions with the motion captured data. For all following leg poses of an experiment, the model joint angles determined from the previous time point served as initial estimate for the global optimization procedure.

Table 4.1 Joint angle constraints of the kinematic model

legs	**joint**	**angle constraints**					
		yaw (°)		pitch (°)		roll (°)	
		min	max	min	max	min	max
front	ThCx	-70	70	-28	142	-50	-160
	CxTr	-160	20	-103	67	-120	120
	TrFe	-90	90	-103	67	-90	90
	FeTi	10	180	-92	78	-90	90
	TiTar	-60	20	-77	78	n.a.	n.a.
middle	ThCx	-60	90	-35	135	-90	90
	CxTr	-10	140	-49	121	-90	90
	TrFe	-110	110	-118	52	-90	110
	FeTi	-170	0	-92	78	-90	90
	TiTar	-60	20	-77	93	n.a.	n.a.
hind	ThCx	-60	90	-34	136	-100	100
	CxTr	-30	110	-116	54	-90	110
	TrFe	-90	90	-49	121	-90	90
	FeTi	-180	-10	-98	72	-90	90
	TiTar	-90	5	-80	90	n.a.	n.a.

Note that values indicate constraints for joint DOFs of right legs. The sign had to be inverted to obtain values for yaw and roll DOFs of left legs, but not for pitch DOFs.

4.2.4 Adaptation of model and tracked animal data

Since flies differed in their body size and length of leg segments, prior adjustments of the model and the motion capture data were required for each fly to facilitate the inverse kinematic procedure.

To ensure equal body coordinate systems, reference triangles for the model and the motion capture data were formed by connecting the median positions of the thorax posterior scutellum apex (A), left wing hinge (L), and right wing hinge (R). A scale matrix (S) was calculated for scaling the model to fit it to the motion capture data (**Eqs. 4.13**).

$$
\begin{aligned}
k_x &= \left(\frac{\overrightarrow{AR}_{model_x}}{\overrightarrow{AR}_{motion-capture_x}} + \frac{\overrightarrow{AL}_{model_x}}{\overrightarrow{AL}_{motion-capture_x}}\right) * 0.5 \\
k_y &= \frac{\overrightarrow{RL}_{model_y}}{\overrightarrow{RL}_{motion-capture_y}} \\
k_z &= \left(\frac{\overrightarrow{AR}_{model_z}}{\overrightarrow{AR}_{motion-capture_z}} + \frac{\overrightarrow{AL}_{model_z}}{\overrightarrow{AL}_{motion-capture_z}}\right) * 0.5 \\
S &= \begin{bmatrix} k_x & 0 & 0 \\ 0 & k_y & 0 \\ 0 & 0 & k_z \end{bmatrix}
\end{aligned}
\tag{4.13}
$$

Afterwards, positions of the motion captured keypoints of each leg were translated to ensure comparable initial locations of the kinematic leg chains and the motion captured leg positions. For this, the vector (v) between the ThCx position of the kinematic leg chain and the median motion captured ThCx position was subtracted from each subsequent keypoint position of the same leg (**Eqs. 4.14**).

$$
\begin{aligned}
\vec{v} &= ThCx_{leg_{motion-capture}} - ThCx_{leg_{model}} \\
T_{\vec{v}}(i) &= i - \vec{v}, \forall\{i \in ThCx_{leg}, CxTr_{leg}, TrFe_{leg}, FeTi_{leg}, TiTar_{leg}, Tar_{leg}\}
\end{aligned}
\tag{4.14}
$$

As a final step, the leg segment lengths of the model were adjusted to the median lengths of the motion captured leg segments. For each segment, the segment vector between the proximal and distal keypoint positions (P) was calculated and scaled to the desired length. To adjust the length of the model segment, the distal keypoint position was translated in direction

of the scaled segment vector (**Eqs. 4.15**). All adjustments were carried out prior to the construction of the kinematic model for each individual fly.

$$\overrightarrow{segment} = P_{distal} - P_{proximal} \tag{4.15}$$

$$\vec{v} = (P_{model_{proximal}} + \frac{median(|\overrightarrow{segment}_{motion-captured}|)}{|\overrightarrow{segment}_{model}|} \overrightarrow{segment}_{model}) - P_{model_{distal}}$$

$$T_{\vec{v}}(P_{model_{distal}}) = P_{model_{distal}} + \vec{v}$$

4.2.5 Analysis of the model error and joint angles

The model error of a leg keypoint was the distance between its position in the model and its tracked position. Since the positions were in body coordinates after inverse kinematics, they were first converted to world coordinates of the motion capture system for scaling the error to metric units (µm or mm). Afterwards, the Euclidian distance between both positions was calculated (**Eq. 4.16**).

$$error = \sqrt{(x_{tracked} - x_{model})^2 + (y_{tracked} - y_{model})^2 + (z_{tracked} - z_{model})^2} \tag{4.16}$$

Since there is no defined zero angle position for the joint DOFs of *Drosophila*, most resulting joint angles of the model were reported in relation to the initial posture of the model (**Figure 4.1C**). To simplify the interpretation for movements the angles of two main DOFs, namely the CxTr-yaw and the FeTi-yaw, were post-processed. Because the leg segments were straightened at the zero-angle position for these DOFs, subtracting or adding the resulting angles for the CxTr-yaw and the FeTi-yaw to 180 degrees, respectively, allowed to obtain zero degrees for a fully flexed posture and 180 degrees for a fully extended posture. Furthermore, to combine joint angles for contralateral legs, the sign of angles for the yaw and roll DOFs of the left legs were inverted, but not for angles of pitch DOFs.

To compare model errors and joint movements of different flies, the time courses were normalized to the swing and stance phases. For this, lift-of and touch-down events for each step were determined from the motion capture data set. Since the flies walked on a ball with a known diameter (see **3.2.1**), it was assumed that during the stance phase the distance of the

tarsus tip of the legs to the center of the ball must be approximately the radius of the ball, while the distance must be larger when the legs were in swing phase. To estimate the center of the ball, an optimization function for the center position and radius of a sphere was used to minimize distance of the tracked tarsus tips to the radius of the sphere (least_squares function, SciPy optimization package version 1.6.2, The SciPy community). A penalty factor of 100 was multiplied to distances of the tarsus tip positions smaller than the sphere radius within the cost function to ensure that the tracked tarsus tip positions of legs in stance phase were on the surface of the sphere but not inside the sphere. Afterwards, a leg was assumed to be in swing phase when the tarsus tip positions showed a larger distance than 1.05-times the estimated radius of the sphere. To eventually obtain normalized phases with equal durations ranging from zero to one, data sets of the individual swing and stance phases were linearly interpolated to a sample size of 100.

4.2.6 Hierarchical cluster analysis of DOF configurations

To explore a wide variety of DOF configurations of the kinematic leg chains and their potential to explain forward stepping in *Drosophila*, an agglomerative hierarchical cluster analysis (AHCA) was performed. In AHCA, data objects are grouped based on their proximity in a hierarchical cluster tree, also known as dendrogram, by using an iterative bottom-up algorithm (Hastie et al., 2009). To determine the proximity, the distance of features between a pair of data objects or clusters is calculated and the resulting values are recorded in a distance matrix for all possible pairs. The algorithm starts with each object as a single cluster and then iteratively merges the closest clusters, i.e. with the smallest distance, until only one cluster is left. After each iteration, the distances between the new set of clusters is calculated and used for the next iteration. The resulting dendrogram visualizes the hierarchy of clusters by highlighting at which distance two clusters were merged. Finally, to obtain a definite number of separated clusters, the dendrogram is cut at a certain threshold level.

In this thesis, AHCA was used to cluster 112 DOF configurations based on the similarity of their DOF states and the resulting model error. DOF configurations were represented as binary feature vectors, i.e. the state of each DOF in the configuration was described by zero or

one, depending on whether it was fixed or moveable, respectively. The hamming distance, which counts the number of differences between two DOF vectors (**Eq. 4.17**), served as measure for the distance of DOF states between DOF configuration pairs.

$$D_H(x,y) = \sum_{i=1}^{n} \begin{cases} 0, & \text{if } x_i = y_i \\ 1, & \text{if } x_i \neq y_i \end{cases} \tag{4.17}$$

To determine the pairwise distance of the model error, the absolute difference between the mean error of DOF configuration pairs was calculated. The mean error was calculated from a subset of leg postures in order to minimize the computational time for inverse kinematics. Therefore, the first, middle, and last leg posture of the swing and stance phases of the first two steps from each leg of each examined fly were extracted, i.e. in total 288 leg postures for each leg pair were analyzed for each DOF configuration.

Distance matrices for the DOF states and the model error of each leg pair were formed and normalized by dividing by the largest distance value in each distance matrix. For each leg pair, the average distance matrix of the DOF states and respective leg pair model error distance matrices was used as input for the AHCA algorithm (linkage function, SciPy cluster package version 1.6.2, The SciPy community). To compute the distance between two clusters, the Ward variance minimalization criterion was used (Ward, 1963). The cut threshold for each dendrogram was set manually to define a reasonable number of clusters for the following analysis. The threshold was chosen to obtain clusters which predominantly contained DOF configurations showing similar mean model errors.

For a detailed analysis of the obtained clusters, clusters were sorted by their minimum, mean, and maximum model error and the DOF configurations within each cluster were sorted by their mean error. This resulted in an ascending order of DOF configurations with respect to their mean model error, but while preserving the DOF state similarity obtained from clustering. To group DOF configurations exhibiting a similar model error beyond cluster boundaries, the 95% CI of the model error was used as criterion (see **2.3**). Sets with similar model errors were formed sequentially. When the 95% CI of the mean error of a DOF configuration did not include the mean error of the first DOF configuration in a set, it was

assumed that the two mean errors were different. Consequently, the mean error of a DOF configuration was used to define a new set if it could not be assigned to an existing set.

4.3 Results

4.3.1 Creation of a reference model to study leg kinematics

Since the actual DOF configuration of the *Drosophila* legs is not known, an initial reference model based on reported DOFs for *Drosophila* and other insects (Bender et al., 2010; Cruse and Bartling, 1995; Lobato-Rios et al., 2022; Soler et al., 2004) was created at first (**Figure 4.1C**).

The ThCx was implemented as ball-and-socket joint with all three DOFs (yaw, pitch, and roll). All other major joints in insect' legs are usually described as hinge joints with one DOF (Ritzmann and Bender, 2010). Thus, only the yaw DOF which represented the rotational axis derived from joint condyles was set to be moveable in the CxTr and FeTi. Because whether the TrFe is moveable in *Drosophila* is unknown, it was not considered in the reference model.

Since motion capture of all tarsal joints was not feasible, the tarsus was implemented as a single segment in the present model. During initial modeling attempts using only the yaw DOF for the TiTar, it became clear that tarsal motion could not be fitted well with a single DOF and a constant length of the tarsus. This was mainly due to the fact that the tarsus bent during stance phase (**Figure 4.2A**). Consequently, the model tarsus was often too short or too long for an optimal fit of the TiTar and the Tar positions. To compensate for this, the length of the tarsus was adjusted in a frame-by-frame manner to the length of the tracked tarsus. Furthermore, since tarsal bending occurred also bi-directionally, the pitch DOF of the TiTar was added to all models by default. This allowed to model the complexity of tarsal motion with only three parameters.

4.3.2 Evaluation of the reference model fit to tracked animal leg postures

To measure how well the reference model can adopt natural leg postures, the model error, i.e. the distance between model and tracked animal keypoints, was determined after the model was fitted by inverse kinematics.

The summed mean model error was largest for front legs (**Figure 4.3**). Moreover, the error was not constant during step phases, but showed a minimum of 281 ± 82 μm at the middle of the stance phase and a maximum 553 ± 131 μm at the end of the swing phase (n: 241/242, swing/stance). The increase in error during swing phase was mainly caused by the inability of the model to accurately adopt the positions of TrFe, FeTi, and TiTar. While the errors for the TrFe and FeTi model positions increased at the stance-to-swing transition and were relatively constant afterwards, the model error for the TiTar increased gradually during the swing phase. That was accompanied by a misalignment of model and tracked leg segments, which was particularly evident in the late swing phase. Here, the model's tibia did not align properly with its tracked counterpart, but the two were crossed over (**Figure 4.2B**). In addition, the misalignment of segments also affected the model's ability to fit the tracked Tar position, resulting in a 2- to 3-fold increase of model error for the Tar during the late swing phase (**Figure 4.3**).

For middle and hind legs, the mean model error for all leg keypoints was consistently smaller than for the front legs (**Figure 4.3**). The summed mean model error was similar for middle and hind legs and ranged from 104 ± 35 μm to 132 ± 40 μm (n: 256/258, swing/stance) and from 111 ± 56 μm to 152 ± 47 μm (n: 263/272, swing/stance), respectively. Furthermore, there was no strong relationship to phase of the model error for either middle or hind legs as observed for the front legs, and consequently a proper alignment of model and tracked leg segments was achieved throughout the stepping cycle (**Figure 4.2B**).

In summary, the reference model was already able to adopt very well to the tracked leg postures of the middle and hind legs. For the front legs, however, it showed only an acceptable fit to tracked keypoints during the stance phase, but failed to adopt to the tracked leg postures during the swing phase.

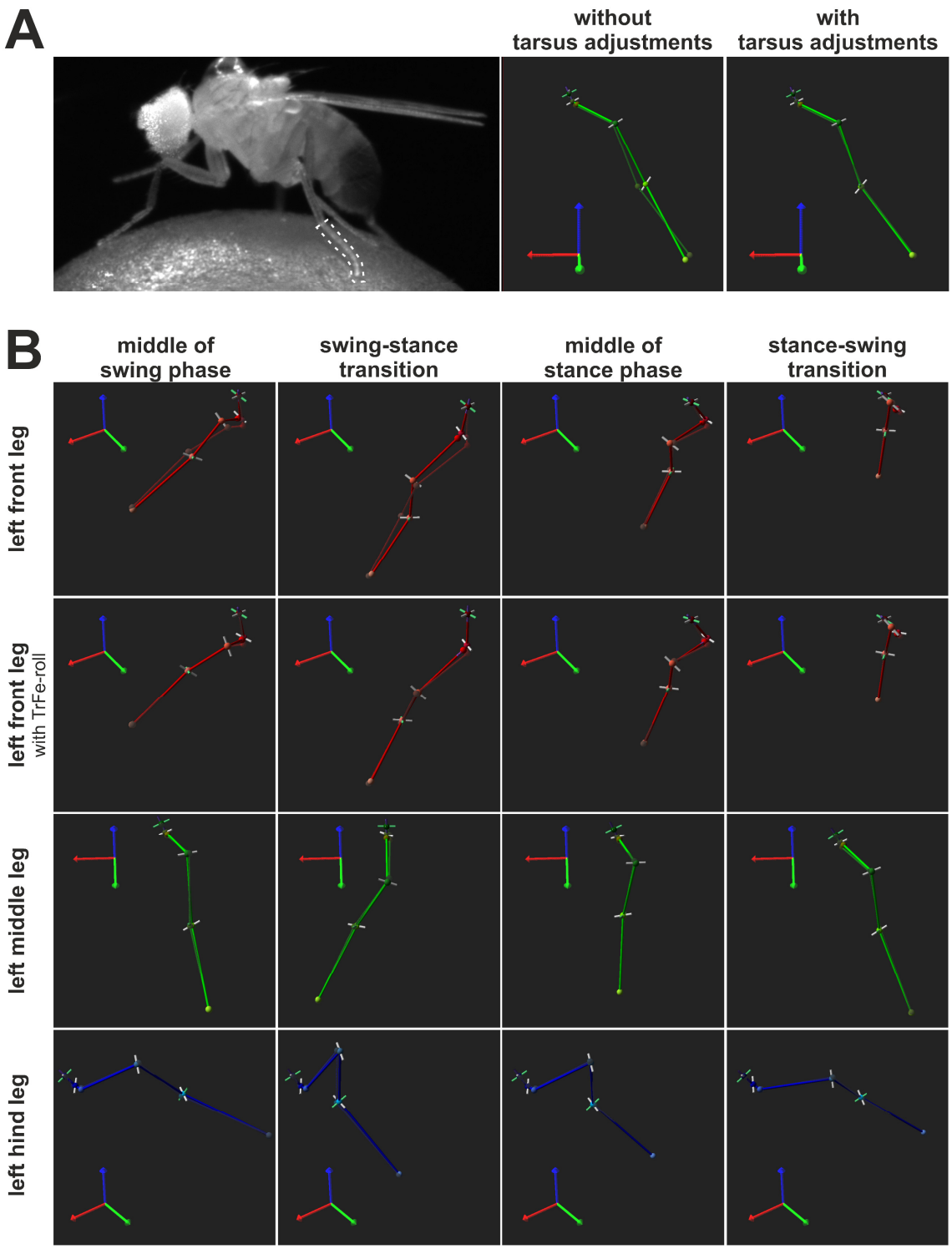

Figure 4.2. Representative model leg postures. (**A**) Example for bending of the tarsus and its influence on the model. The left panel depicts a video frame showing a walking fly with a bent middle leg tarsus. The dashed white outline indicates shape of the tarsus. The resulting posture for a model without (middle panel) and with adjustments for tarsus fitting (left panel). Note that the model cannot fit accurately the leg posture without adjustments, i.e. equipping the TiTar with two DOFs and adjusting the length of the tarsus for each frame. (**B**) Example model postures for front, middle, and hind legs for

middle of swing phase, swing to stance transition, middle of the stance phase, and stance to swing transition. For front legs, resulting postures for the reference model without (1st row) or with an additional TrFe-roll DOF. Joints/tarsus tip and leg segments of the model (solid) and the tracked fly legs (pale, transparent) are displayed as spheres and cylinders, respectively. 3D coordinate systems indicate directions. The red (x-axis), green (y-axis), and blue (z-axis) arrows point towards anterior, left, and dorsal with respect to the fly body.

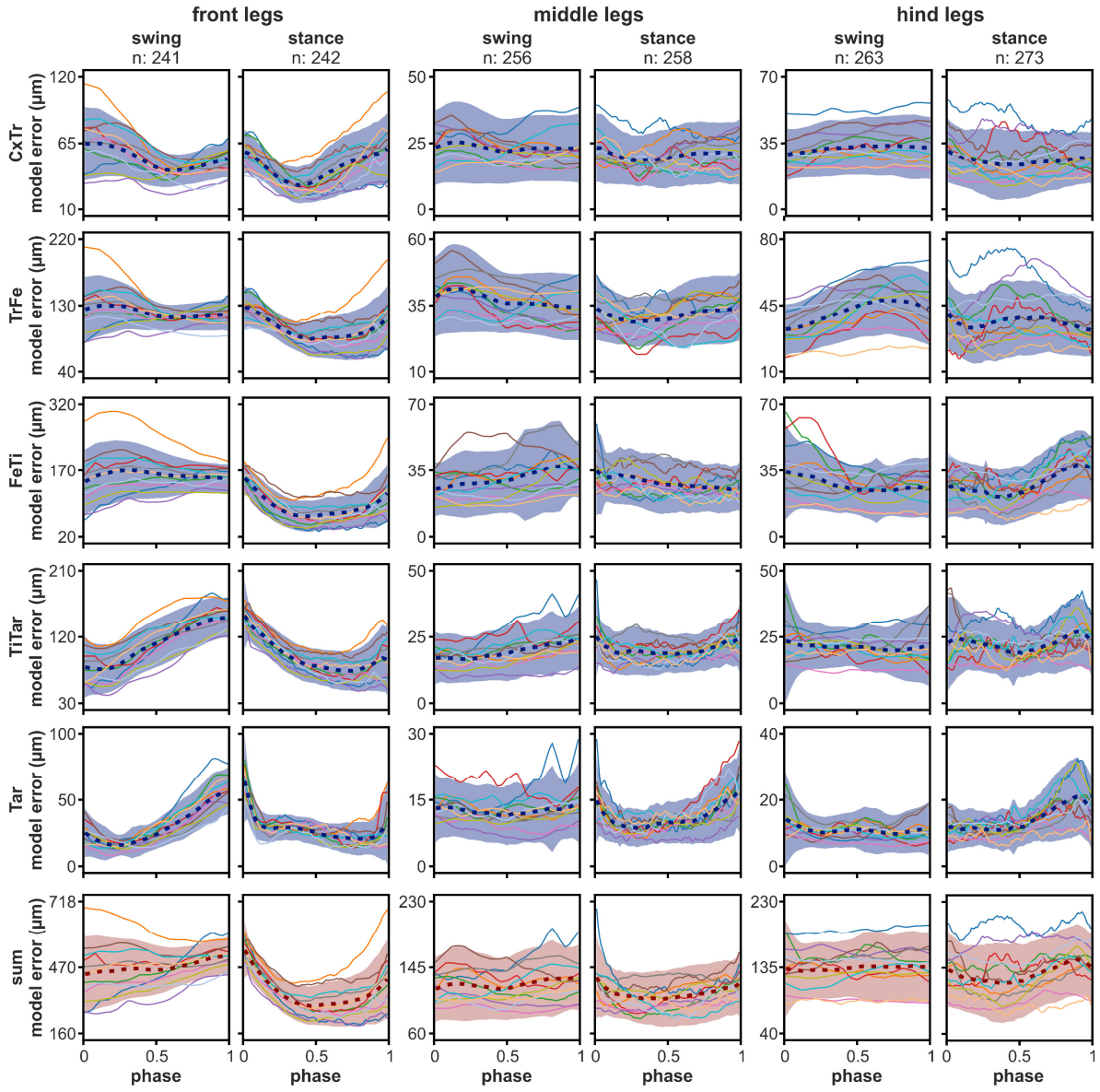

Figure 4.3. Evaluation of model error. Model error for front, middle, and hind legs during swing or stance phase. Dashed lines represent the mean time course of the model error for individual leg keypoint positions (blue) or their sum (red) during swing and stance. The colored (red/blue) areas indicate the standard deviation. Solid colored lines show the mean time courses of single flies.

4.3.3 Impact of fixing DOFs of the ThCx on the model error

Next, it was examined whether all three DOFs of the ThCx were required for modeling the tracked leg postures. For this purpose, one or two DOFs were systematically fixed by excluding them from inverse kinematics procedure and the relative percent change of the resulting mean model error to the reference mean model error was evaluated. On average, the elimination of one or two DOFs always resulted in a by 10% to 333% higher model error for all three leg pairs compared to the reference model error, but effects varied between leg pairs (**Figure 4.4A**).

For the front legs, the pitch DOF was most important for the model fit around the swing-to-stance transition, while the roll DOF influenced mainly the model error around the stance-to-swing transition (**Figure 4.4A**). Removal of the pitch DOF had the strongest influence on the model error which was approximately 287% higher compared to the reference model error at the end of the swing phase. All tested DOF combinations without pitch showed a similar time course, beginning with a steady increase of the error at the middle of the swing phase, a peak at the swing-to-stance transition, and a steady decrease until the late stance phase (**Figure 4.4A**: yaw, roll, yaw + roll). In contrast, when the roll DOF was eliminated, the model showed higher errors around the transition from stance-to-swing (**Figure 4.4A:** yaw, pitch, yaw + pitch), but the error decreased during the remaining step phase for DOF combinations containing the pitch DOF. Moreover, the model error was only ~ 23% to 54% higher when the model ThCX was equipped with both, i.e. pitch and roll DOFs, while the model error showed a combinational adverse effect when both were missing, i.e. the ThCx had only the yaw DOF. Although that argues for a less important role of the yaw DOF for forward stepping of the front legs, the yaw-DOF was able to reduce the model error when the roll DOF was absent. During the late stance phase, the error was more pronounced when the ThCx was equipped with the pitch DOF only compared to all other DOF combinations tested, but adding the yaw DOF partially improved the model fit (**Figure 4.4A**: yaw + pitch).

In contrast to the front legs, the yaw DOF was more important for the model fit of the middle legs throughout the step cycle. The model error was similar for ThCx configurations including the yaw DOF which was about 15% to 83% higher than the reference model error and did not show a strong phase dependency (**Figure 4.4A**: yaw, yaw + pitch, yaw + roll). The model error

was most increased when the ThCx was equipped with the roll or the pitch DOF only (**Figure 4.4A**). When only the roll DOF was available, the increase of the model error was highest from the middle of the stance phase to the stance-to-swing transition with a peak increase of 333% at the begin of the swing phase followed by a decline during the swing phase. It rose again at the begin of the stance phase. In contrast, the error increase was biphasic, peaking at the middle of the stance and swing phases and was minimal at the transitions between the step phases when the ThCx had the pitch DOF only. Except during the late the swing phase and during the early stance phase, the increase in error was also much smaller for this ThCx configuration compared when only the roll DOF was available. Interestingly, combining roll and pitch DOFs resulted in a model error relatively similar to joint configurations including the yaw DOF during most of the swing phase and the early stance phase (**Figure 4.4A**).

For the hind legs, the model fit was most affected when the ThCx was equipped with the pitch DOF, only resulting in an 73% to 251% higher error. Here, the error increased steadily from the beginning of the swing phase until it reached its peak during the early stance phase and decreased steadily until the end of the stance phase (**Figure 4.4A**). In contrast, the error for all other tested configurations showed a relative constant or only a slight gradual increase during the swing phase and was 13% to 91% higher than the error of the reference model. During the stance phase, the relative increase in error exhibited a hump between the beginning and the middle of the stance phase which was differently pronounced for individual DOF combinations. Additionally, the increase of model error was lowest when the roll and pitch DOFs were moveable in the ThCx.

Taken together, these findings show that individual DOFs of the ThCx contribute differentially to leg stepping of the leg pairs in a step phase-dependent manner. Additionally, the best model fit for all leg pairs was always achieved when all three DOFs were moveable in the ThCx.

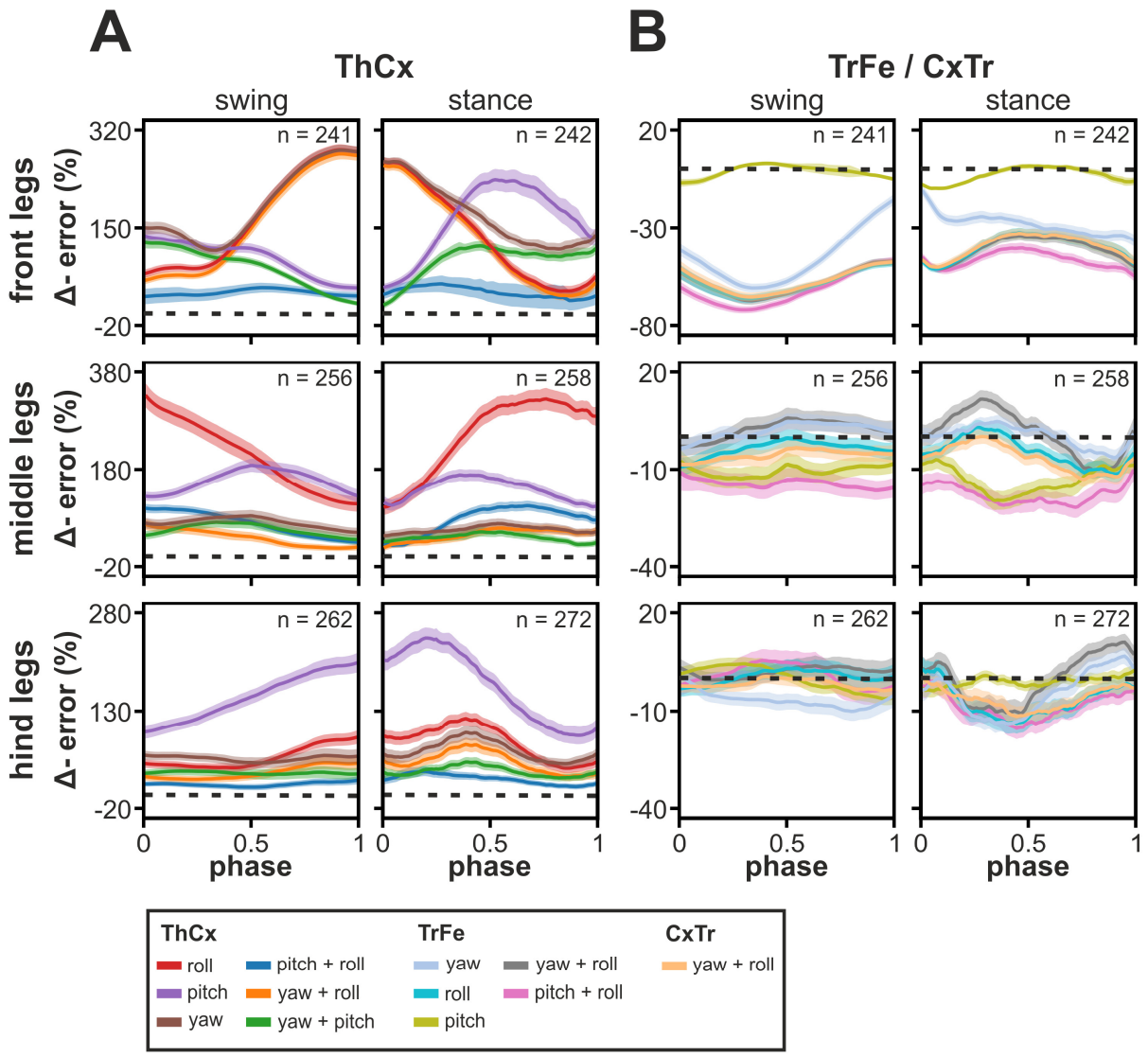

Figure 4.4. Change of model error by removal or addition of DOFs compared to reference model. (**A**) Removal of one or two DOFs of the ThCX joint. (**B**) Addition of one to two DOFs in the TrFe joint or addition of the roll DOF in CxTr joint. Error is represented as relative difference to reference model error in percent. Colored lines and areas show the mean change and the 95% CI during swing or stance phase, respectively. Dashed black lines indicate zero change, i.e. no difference to the error of the reference model. n indicates the number of phases used for the analysis.

4.3.4 Impact of adding DOFs to the TrFe or the CxTr on the model error

To test whether the TrFe could play a role in straight forward walking of *Drosophila*, the relative mean change of the model error was evaluated when one DOF of the TrFe was set moveable during the inverse kinematics procedure at first.

For the front legs, the model error was drastically reduced throughout the step cycle when the TrFe was equipped with either the yaw or the roll DOF, while utilizing of the pitch DOF showed only a slight decrease of the error at the step phase transitions (**Figure 4.4B**). The maximum reduction occurred at about one-third of the swing phase with a relative mean decrease of -62% and -67% when the yaw or roll DOF was added to the TrFe, respectively. The reduction was, however, smaller at the transitions between swing and stance and vice versa. This was particularly apparent at the swing to stance transition when the TrFe was equipped with the yaw DOF with a relative error reduction of -11%. Moreover, the relative error reduction was smaller almost throughout the entire stance phase compared to the swing phase, but the maximal reduction was still -37% and -51% when the yaw or the pitch DOF were moveable, respectively (**Figure 4.4B**). Strikingly, when the roll DOF was moveable, the observed misalignment between the model and the tracked animal tibia during the swing phase disappeared, but was still present when one of the other DOFs was moveable.

Based on the finding that the roll DOF improved the model fit most, it was further tested whether a second DOF in the TrFe, in addition to the roll DOF, would result in an even better fit. Additionally, the relative change of the model was investigated when, in addition to the yaw DOF, the CxTr was provided with a roll DOF, since existence of this DOF in *Drosophila* was suggested by Lobato-Rios et al. (2022). For a combination of a jaw and a roll DOF in either the TrFe or the CxTr, the reduction in model error was very similar to the situation when the TrFe was equipped with the roll DOF only. Additionally, the model fit was only slightly more improved when the pitch and roll DOFs were together moveable in the TrFe (**Figure 4.4B**).

In contrast to the front legs, addition of one or two DOFs did not remarkably improve the model fit for neither the middle legs nor the hind legs (**Figure 4.4B**). For the middle legs, there was a consistent but only small reduction of the model error throughout the step cycle when

a pitch DOF was added to the TrFe, i.e. pitch or pitch + roll, with a relative change of the model error ranging from -4% to maximal -17%. All other tested DOF configurations did not improve the model fit or even showed a slight increase of error. This was also observed for the hind legs for which only addition of a yaw DOF to the TrFe could improve consistently the model fit throughout the swing phase. Additionally, all tested DOF configuration, except for the TrFe having a pitch DOF only, exhibited a temporary relative reduction of the model error for the hind legs at the early stance phase which was maximally about -12% to -18%.

In summary, these findings indicate that a roll DOF in the TrFe or CxTr is required to explain forward leg stepping of the front legs. For the middle or hind legs, despite the fact that some DOF configurations resulted in an up to maximal -18% lower model error compared to the reference model error, this reduction was often not consistent throughout the step cycle. Moreover, the impact on the model fit might be rather negligible when considering that the absolute model error was already low for the reference model. This suggests that the addition of DOFs to the kinematic leg chains of these leg pairs might not be necessary to properly model forward stepping.

4.3.5 Systematical evaluation of putative DOF configurations

Although removing or adding individual DOFs had already provided vital information for determining the natural DOF configuration of *Drosophila* legs, this approach was limited in that only a small number of DOF configurations could be meaningfully compared. Moreover, the interpretation of results could be complicated when considering the compensating effects of redundant systems such as kinematic chains, e.g. the absence of an individual DOF could be compensated by the remaining DOFs. To obtain a comprehensive picture of the requirement of individual DOFs for explaining forward stepping, various putative DOF configurations were examined using a systematical approach.

In principle, 4096 combinations of DOF states would be possible, ranging from no moving joint to all joints are ball and socket joints with three DOFs, considering only the ThCx, CxTr, TrFe, and FeTi. However, because many of these combinations are not biologically plausible,

a subset of 112 DOF configurations was selected. The following assumptions were used to define and constrain this set:

1) The ThCx has one to three DOFs.
2) The CxTr is usually described as hinge joint and thus always has the yaw DOF.
3) The CxTr might have a roll DOF (Lobato-Rios et al., 2022), but no pitch DOF.
4) The TrFe might be movable with one to three DOFs. However, it might also be fixed with no DOF.
5) The FeTi is commonly described as hinge joint and thus always has the yaw DOF, but no other DOF.
6) The TiTar was always modeled with a yaw and a pitch DOF (see **4.3.1**).

Inverse kinematics were performed on a leg posture subset (n=288, see **4.2.6**) for all 112 DOF configurations. Front legs exhibited the largest mean model errors for DOF configurations ranging from 153 ± 63 μm to 1,000 ± 614 μm, while middle and hind legs showed comparable smaller ranges of mean errors with 120 ± 34 μm to 332 ± 131 μm and 134 ± 49 μm to 311 ± 113 μm, respectively. To group DOF configurations with respect to their DOF state similarity and the resulting model error, a hierarchical cluster analysis was performed (**Figure 4.5**). The resulting dendrograms displayed that DOF configurations were differently grouped for each leg pair (**Figure 4.5B**). Moreover, the model fit of the front legs was affected by larger number of DOF configurations than the other leg pairs. For the front legs, 41% of DOF configurations resulted in a relative model error higher than 0.5. In contrast, this was the case for only 4% and 2% of DOF configurations for the middle and hind legs, respectively. This indicates that the kinematics of front leg were more dependent on specific DOFs, while the movement of the other leg pairs can be modeled relatively accurately by a large variety of DOF configurations.

To obtain clusters for further analysis, cutting the dendrograms at a distance of 0.04, 0.05, and 0.03 resulted in 38, 35, and 46 clusters for front, middle, and hind legs, respectively. The clusters were predominately homogenous in terms of their minimum, mean, and maximum relative model error, demonstrating that the used clustering method was efficient in grouping DOF configurations with similar model errors (**Figure 4.6**). After sorting the clusters according to their relative model errors and the DOF configurations within each cluster according to

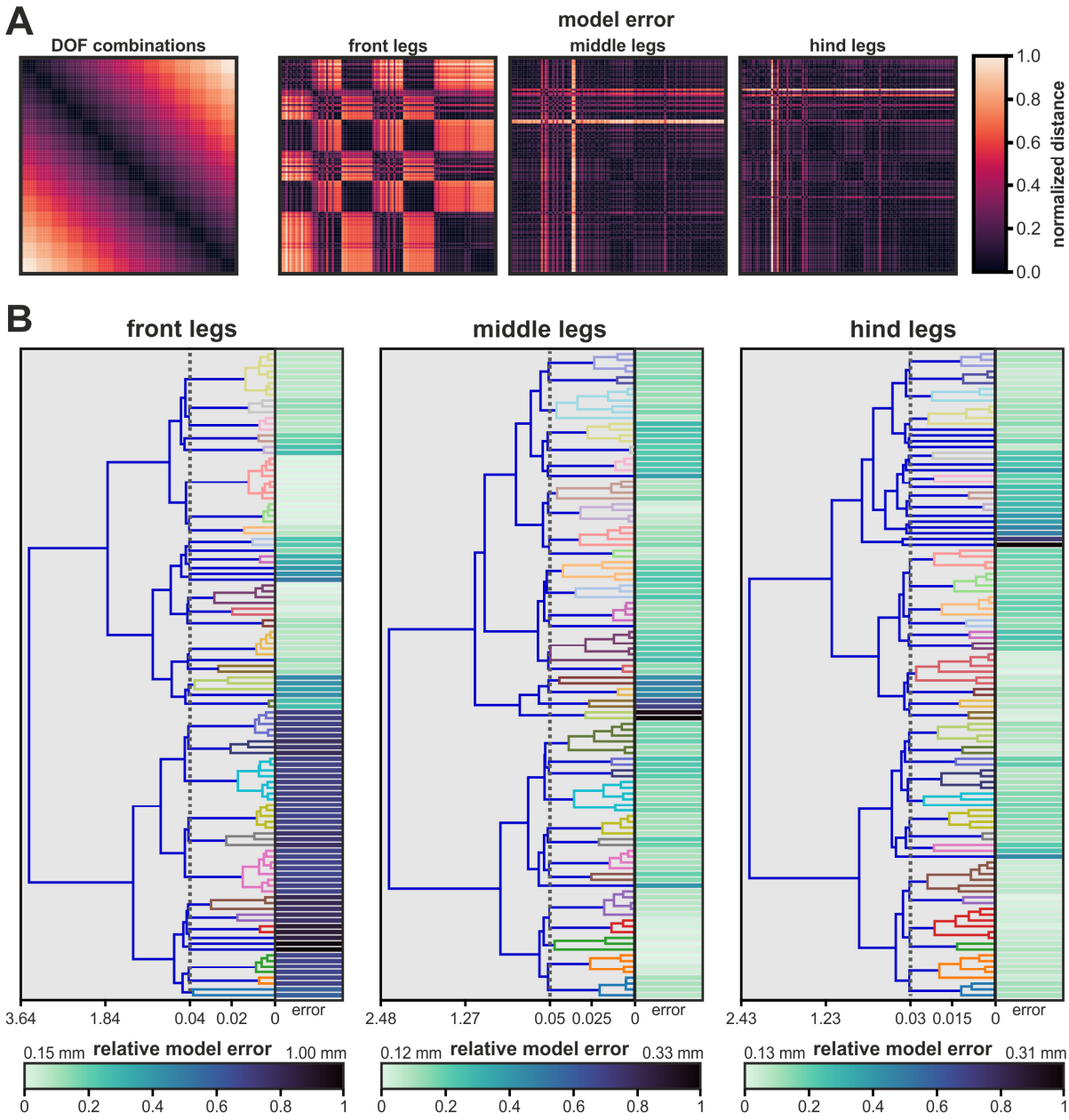

Figure 4.5. Hierarchical clustering of DOF configurations. (**A**) Normalized distance matrices for DOF configuration and model error of the front, middle, and hind legs. (**B**) Dendrograms resulting from hierarchical cluster analysis for front (left panel), middle (middle panel), and hind (right panel) legs and the relative model error for each DOF configuration. Relative error ranged from zero to one and based on the minimum and maximal observed absolute error, respectively. Absolute observed errors were indicated above the color bars for each leg pair. The dashed gray lines in the dendrograms indicate the used cut distance threshold for obtaining a defined number of clusters (color-coded). For clarity, the x-axes were scaled differently before and after the cut threshold.

their absolute mean model error, the resulting order of DOF configurations revealed that many configurations exhibited very similar error levels even beyond the cluster boundaries with numerically only slightly different means. That, however, implied that the quality of model fit cannot be meaningfully distinguished within subsets of DOF configurations. Hence, in the next step, these subsets of model error were identified by using the 95% CI of the absolute mean errors as criterion (**Figure 4.6**, color-coded bars showing the mean of the absolute error), i.e. a DOF configuration was assigned to a subset when its CI of the mean included the first mean of the respective subset (see **4.2.6** for details). Since DOF configurations of the same subset were considered equivalent in terms of model error, their DOF state compositions were further examined to gain insight into the necessity of individual DOFs for explaining forward stepping of the leg pairs.

The subsets with the smallest model error included 16, 12, and 38 DOF configurations for the front, middle, and hind legs, respectively. Eight DOF configurations were shared among all leg pairs, but there were also configurations unique for each leg pair (front: 2, middle: 1, hind: 21). With six to nine movable DOFs all of the shared configurations had a larger number of available DOFs than the reference model (5 DOFs, without TiTar which was identical in all configurations). It is, however, important to bear in mind that a larger number of available DOFs generally increases the flexibility of kinematic chains in fitting data points, and consequently, a better fit does not necessarily mean that the model reflects reality more closely. For example, it was not surprising that the DOF configuration in which all nine tested DOFs were moveable was always found in the subset with the smallest model error for all leg pairs. On the other hand, and also not surprisingly, configurations with a small number of DOFs were more often associated with a larger model error and thus accumulated at the bottom of the sorted order of configurations (**Figure 4.6**), indicating that a minimum number of DOFs is required for proper kinematic modeling. Further evaluation of the subsets showing the best model fit was therefore focused on identifying a minimum set of DOFs to model appropriately the kinematics of each leg pair and drawing conclusions for the potential of specific DOFs to compensate the absence of others. Additionally, configurations with many moveable DOFs were also considered to provide information about the importance of individual DOFs when they resulted in a higher model error, as this was indicative for the lack of an essential DOF that could not be compensated for by the remaining DOFs.

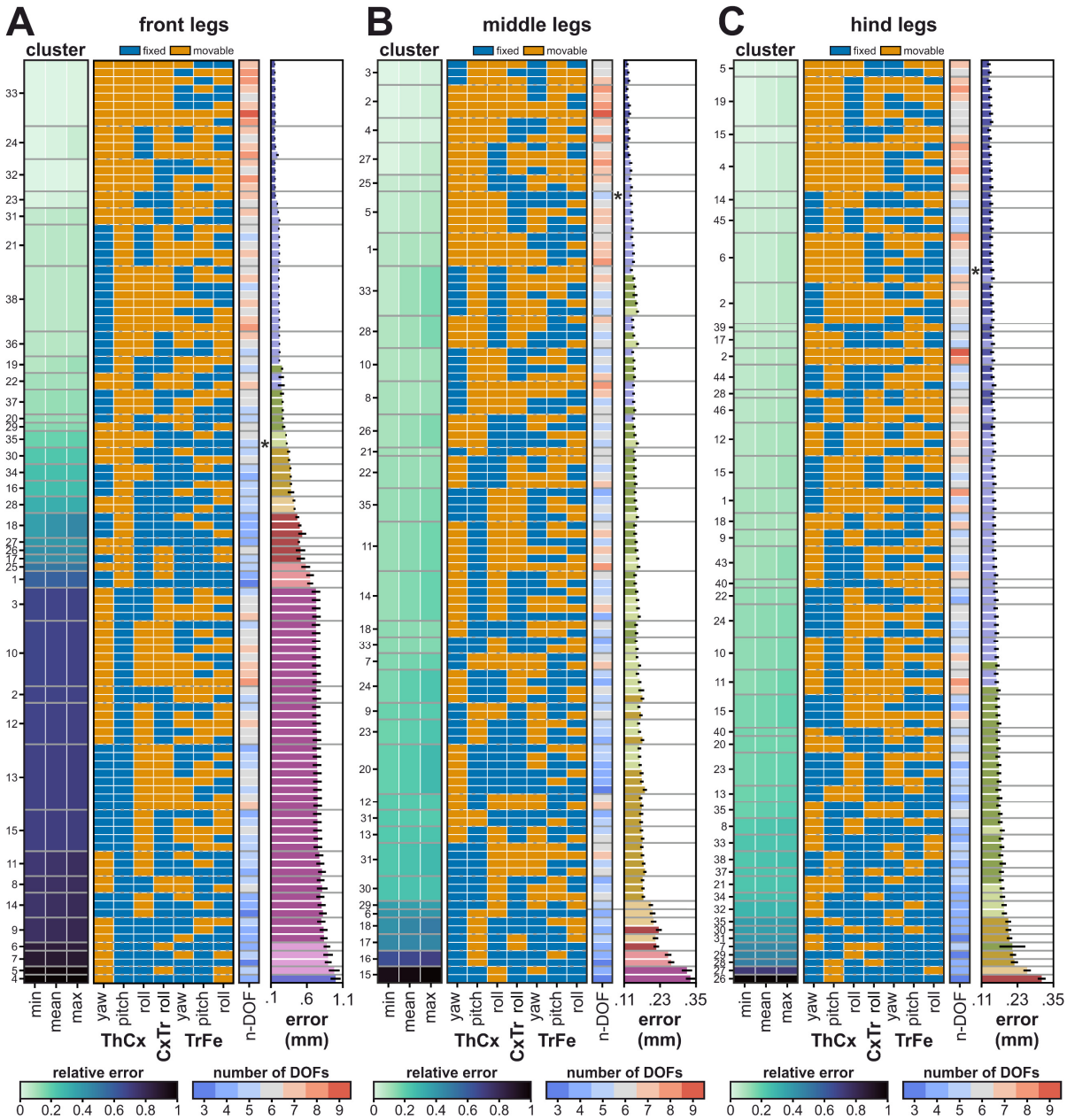

Figure 4.6. Sorting of clusters obtained by hierarchical cluster analysis. Sorted order of clusters and DOF configurations are shown for front (**A**), middle (**B**), and hind (**C**) legs. The left panel displays the relative minimum, mean, and maximum model error (color-coded) for each cluster. The following panels from left to right depict the movable (orange) and fixed (blue) DOFs (for clarity, only tested DOFs are displayed, other moveable DOFs in each configuration were CxTr-yaw, FeTi-yaw, TiTar-yaw, and, TiTar-pitch), the number of movable DOFs including all DOFs in the kinematic chains, and the mean ± 95% CI of the absolute error for each DOF configuration which were sorted in ascending order with respect to their model error. To highlight equivalent model errors, i.e. those that were indistinguishable from each other, between DOF configuration, the same color was used for the mean error bars. The asterisks indicate the position of the reference model. n: 288 leg postures.

For the front legs, the ThCx was equipped with all three DOFs in 75% of configurations within the subset with the smallest model errors, while in the remaining 25% the roll DOF was absent. At least two additional DOFs were, however, required to compensate the lack of the roll-DOF. Strikingly, all configurations of the best model subset included a moveable roll DOF in either the CxTr or the TrFe supporting the previous finding that an additional roll-DOF is required for proper kinematic modeling of the front legs. Additionally, it was found that the ThCx-pitch DOF was most importantly for modeling of front leg kinematics. Generally, its absence resulted in a dramatical increase of the model error (**Figure 4.6A**), while fixing the yaw or roll DOF only moderately increase the error as long as the ThCx-pitch DOF and an additional roll DOF were available (e.g. see cluster 21 in **Figure 4.6A**). Moreover, the model error was 3.44 and 4.74 times higher when only the pitch DOF was missing compared to when only the yaw or roll DOF was absent, respectively (last configurations in cluster 38, cluster 10, cluster 24).

In contrast to the front legs, drawing conclusions for the other leg pairs was much more challenging. This was mainly because the model error for the order of DOF configurations did not increase as dramatically as for the front legs. For the middle legs, in the subset of configurations exhibiting the smallest model errors, all configurations had at least two moveable DOFs in the ThCx, but the pitch DOF was always included (**Figure 4.6B**). When a DOF was absent in the ThCx, an additional roll DOF in either the CxTr or TrFe was required to compensate (see cluster 3 and cluster 27). Interestingly, in all configurations the TrFe was equipped with the pitch DOF. However, when it was added to the reference model, it only slightly reduced the model error by 4% (error with TrFe-pitch: 125 ± 35 μm vs. error without TrFe-pitch: 131 ± 39 μm).

For the hind legs, The DOF configuration subset with the smallest error for the hind legs already comprised 31% of all tested configurations including the reference model (**Figure 4.6C**). This effectively prevented this analytic approach from providing more meaningful insights into the specific requirements of DOFs for modeling walking. On the other hand, these findings suggest that the joint movements of the hind legs are more simplistic compared to the other leg pairs, at least for forward walking.

In conclusion, there were two minimal DOF configurations with a small model error which contained all three DOFs in the ThCx and an additional roll-DOF in the CxTr or the TrFe for

the front legs. Since the CxTr is commonly reported to have only one DOF in insects and the TrFe is not fixed in all insects, the TrFe-roll DOF was added to the model in all following experiments. This improved the model fit substantially as already described in **4.3.4**. However, it is noteworthy that despite the better model fit, the model of the front legs still had problems to reach the tracked TrFe position in the swing phase with high accuracy. For the middle and hind legs, there was no strong evidence to support the addition of an additional DOF or the explicit exclusion of a specific DOF to model forward stepping and thus the reference model kinematic chains were kept unchanged.

4.3.6 Joint angle time courses and leg segment movements

After defining the DOF configurations capable of fitting properly the model to the tracked animal leg postures of each leg pair, the resulting joint angle trajectories and their significance for the associated leg segment motion were evaluated to provide a detailed description of the kinematics. The yaw and pitch DOF of the TiTar were not included in this analysis, because the way the tarsal movements were modeled allowed only limited conclusions to be drawn for the natural contribution of the TiTar to leg stepping. For completeness, however, joint angle time courses for are shown in **Figure 4.7**.

The coxa of the front legs was vigorously moved during forward stepping and its motion was primarily associated with protraction and retraction of the leg. The main contribution to this motion was generated by rotation about ThCx-pitch DOF axis. The mean angle increased gradually from 18.3 ± 4.2 degrees to 51.1 ± 7.0 degrees during swing phase and decreased afterwards to 6.6 ± 4.2 degrees until the late stance phase (**Figure 4.7A**). Interestingly, promotion of the coxa already begun shortly before the lift-off of the tarsus. The ThCx-yaw DOF allowed abduction and adduction of the coxa within a range of 33.2 ± 11.6 degrees. The coxa was moved rapidly towards the body midline between the late stance phase and the beginning of the swing phase. During swing phase, slight adduction was maintained until the middle of the swing phase and was moved gradually away from the midline afterwards until the late stance phase. Rolling of the coxa about the ThCx-roll DOF within a range of 79.1 ± 9.0

degrees was further found. During the swing phase, the coxa was rotated counterclockwise (medial), while the rotation in the stance phase was clockwise (lateral).

The front legs were the only leg pair equipped with an additional TrFe-roll DOF in the model which governed rotation of the femur-tibia plane. There was a counterclockwise (lateral) rotation which started early in the swing phase and was completed at the middle of the swing phase (**Figure 4.7A**). During the stance phase, the counterclockwise (lateral) rotation was resumed until the middle of the stance phase and turned into a clockwise rotation (medial) which lasted until the end of stance.

Rotation about the CxTr-yaw DOF ranging from 31.6 ± 4.5 degrees to 136.0 ± 11.5 degrees in average (**Figure 4.7A**) resulted in elevation and depression of the trochanter and femur segments. During the swing phase, the femur was depressed which contributed to the straightening of the leg, while it was elevated in the stance phase which moved the femur towards the coxa. Additionally, the tibia was extended in relation to the femur during the swing phase, while flexion at the FeTi occurred during the stance phase. This was governed by rotations about FeTi-yaw DOF within a range of 130.5 ± 10.8 degrees.

In the middle legs, protraction and retraction was mainly achieved by promotion and remotion of the coxa as well as rotating the femur-tibia plane. This rotational motion effectively resulted in an anteriorly pointing of the tarsus tip at the end of the swing phase which was reversed during the stance phase. Unexpectedly, both motions were mainly carried out by rotations about ThCx-yaw DOF axis (see also **4.3.7**) with a rotational range of 56.0 ± 13.0 degrees (**Figure 4.7B**). Although the pitch and roll DOFs of the ThCx contributed less to stepping, both affected the leg movements. ThCx-roll DOF led to a slight back and forth swing of the leg (**Figure 4.7B**: clockwise was towards posterior, counterclockwise was towards anterior). Additionally, abduction and adduction movements by the ThCx-pitch DOF supported elevation and depression of the leg during the swing phase, respectively. Rotations about the CxTr-yaw DOF axis within a range of 62.7 ± 15.3 degrees resulted again in elevation and depression of the trochanter-femur segments. Interestingly, this cyclic motion was not separated by the transitions of the leg cycle as in the other legs, but instead elevation was carried out from the beginning of the swing phase until the late swing phase, while depression started only in the middle of stance phase (**Figure 4.7B**). Additionally, extension and flexion

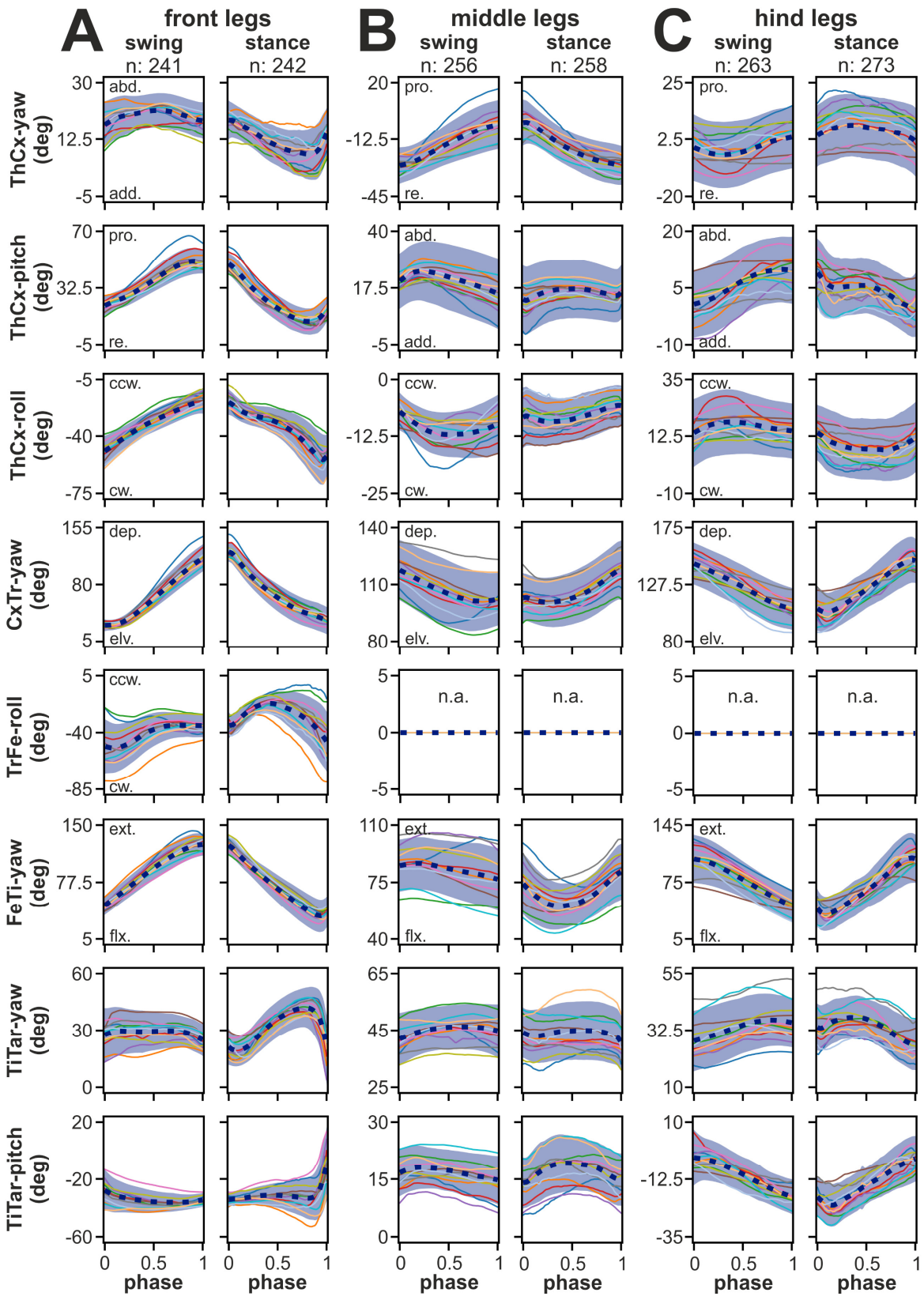

Figure 4.7. Model joint angle time courses. The angle time courses are shown in relation to the normalized swing and stance phases for front (**A**), middle (**B**), and hind (**C**) legs. Angles were calculated in relation to the initial posture of the model, except for CxTr-yaw and FeTi-yaw. These were post-

processed to show the relationship between the linked segments: zero degrees indicates a complete overlap of both segments, while 180 degrees indicates that both segments are on a straight line. Blue dashed lines and blue areas represent the mean ± SD, while solid colored lines represent the mean of individual flies. n-numbers of analyzed phases are indicated at the top for each leg's swing and stance phase. For roll DOFs, anatomical directions for clockwise and counterclockwise rotations are described in the main text. Abbreviations: abd., abduction; add., adduction; pro., promotion; re., remotion; ext., extension; flx., flexion; cw., clockwise; ccw., counterclockwise; n.a., not available.

of the tibia in relation to the femur was not separated by the phase transitions. While the tibia was only slightly flexed during the swing phase, flexion increased strongly during the first half of the stance phase and the tibia was extended in relation to the femur only during the second half.

The rotational movements by ThCx of the hind legs were comparable to those of the front legs, i.e. promotion/remotion, abduction/adduction, and rolling of the coxa. However, in contrast, the ThCx-yaw DOF governed promotion and remotion, while the ThCx-pitch allowed abduction and adduction. Although movements of the coxa were less prominent in the hind legs compared to the front legs, the rotational ranges for ThCx DOFs were relatively similar, except for the smaller range for the roll DOF (**Figure 4.7C**; mean ranges: ThCx-yaw: 44.2 ± 15.7 degrees, ThCx-pitch: 45.8 ± 16.1 degrees, ThCx-roll: 17.3 ± 6.1 degrees; for ThCx-roll: clockwise was towards posterior, counterclockwise was towards anterior). However, the ranges used by individual flies were commonly smaller. The yaw DOF of FeTi and CxTr showed the opposite movements compared to the front legs with respect to the step cycle phases (**Figure 4.7C)**. The femur was lifted and depressed within a rotational range of 141.7 ± 11.9 degrees, while the tibial flexion and extension within a rotational range of 132.8 ± 10.3 degrees occurred during swing phase and stance phase, respectively.

In conclusion, the kinematics of each leg pair showed distinct leg kinematics accompanied by joint angle time courses which were characteristic for the respective leg pairs. Forward stepping of front and hind legs was primarily executed in the anterior-posterior plane, but respective movements in the swing and stance phases were opposite for both leg pairs. For example, swing of front legs was mainly performed by promotion of the coxa, depression of

the femur and tibial extension. In contrast, remotion of the coxa, elevation of the femur and tibial flexion was observed in the hind legs during the swing phase. The middle legs, on the other hand, showed an idiosyncratic kinematic pattern as e.g. rotation of the femur-tibia plane played a major role for protraction and retraction of the legs.

4.3.7 Rotation of femur-tibia plane in the middle legs

Remarkably, although the middle legs showed a prominent rotational movement of the tibia-femur plane during forward walking, the model did not require any additional roll DOF for adopting leg postures, as was the case for the front legs. Moreover, mainly the ThCx-yaw DOF appeared to govern the plane rotation. To gain a deeper understanding of the kinematic origin of the tibia-femur plane rotations, the capability of single and combinations of DOFs to rotate the plane were studied in an *in silico* experiment (**Figure 4.8A**). Therefore, for each analyzed step (n: 210), the model middle legs were set to its initial posture of either the stance or swing phase by using all joint angles. Afterwards, only the angles of selected DOFs were updated for all subsequent leg postures of the respective phase. The rotational range of the plane for each phase was measured by the angle between the plane normal at the beginning and its orientation at the end of the examined phase.

Under control conditions, i.e. angles for all present model DOFs were updated including the three DOFs of the ThCx as well as the CxTr-yaw, the median of the rotational range was comparable for swing and stance phases with 38.2 degrees (IQR: 15.0 degrees) and 40.9 degrees (IQR: 9.2 degrees), respectively (**Figure 4.8B**). Strikingly, most other tested DOF configuration showed a reduction in the rotational range. The reduction was strongest when either the pitch or roll DOF of the ThCx were movable only (mean ± 95% CI for swing / stance: ThCx-pitch only: -32.4 ± 1.4 degrees / -35.3 ± 1.2 degrees, ThCx-roll only: -28.3 ± 1.0 degrees / -34.1 ± 1.0 degrees). In contrast, the rotational range was larger when the ThCx-yaw was the only moveable DOF in the kinematic chain, but it was still reduced by -11.3 ± 0.3 degrees and -12.3 ± 0.3 degrees for the swing and stance phase (mean ± 95% CI), respectively. Adding the pitch, the roll DOF, or both to the ThCx-yaw DOF did not further increase the rotational range of the femur-tibia plane (**Figure 4.8B**). When only the CxTr-yaw DOF was updated during

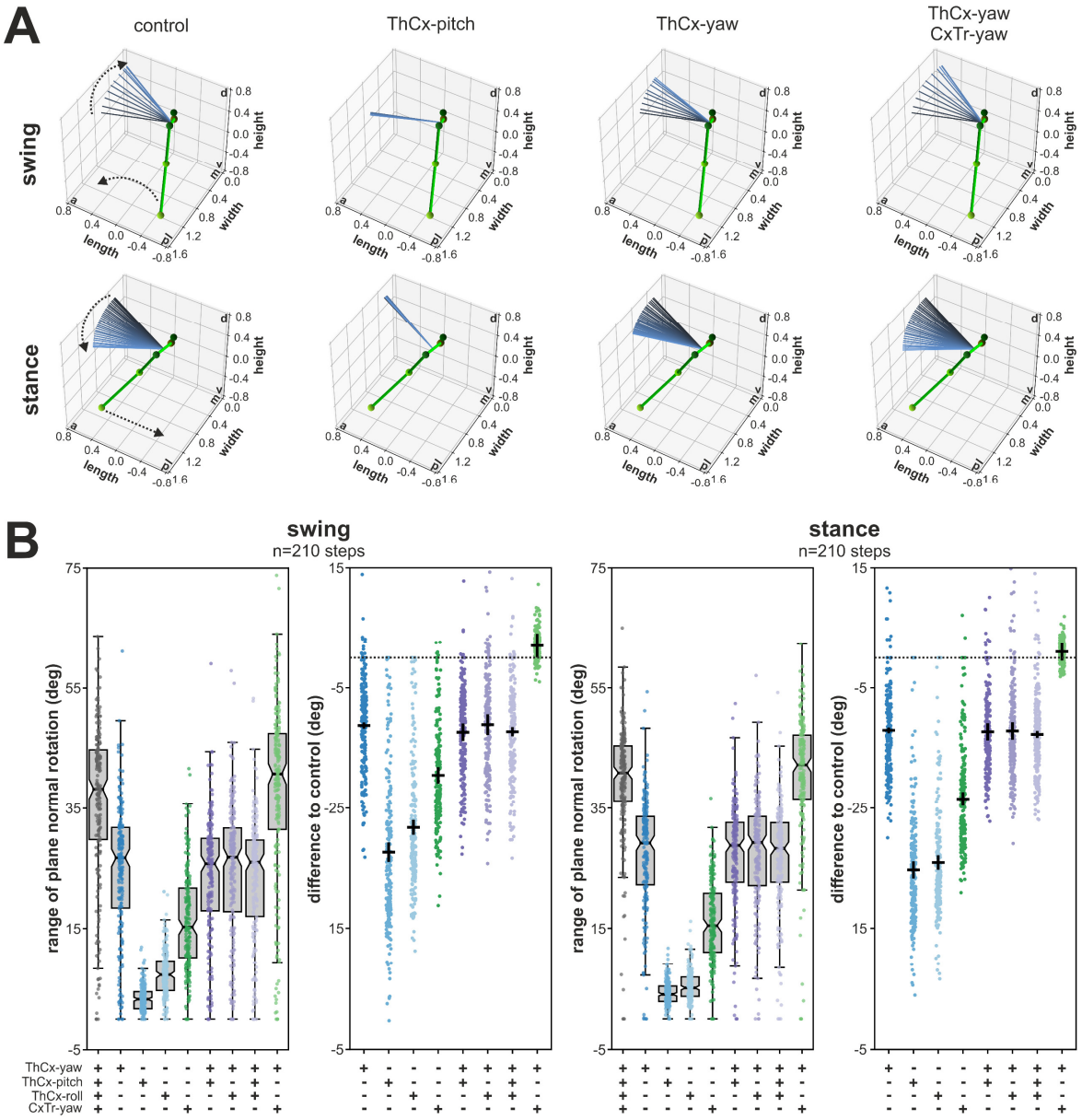

Figure 4.8. Rotation of femur-tibia plane in the middle legs. (A) Example for a left middle leg showing the impact on the femur-tibia plane normal when different DOF combinations were updated in the model during either the swing phase (upper panels) or the subsequent stance phase (lower panels) of one step. Displayed example DOF combinations were from left to right: all ThCx DOFs and the CxTr-yaw DOF (control), only ThCx-pitch, only ThCx-yaw, or ThCx-yaw and CxTr-yaw were updated. The initial posture of the leg for each phase is represented as stick-and-ball model in green. The orientation of the femur-tibia plane normal for each leg posture of the respective phase is represented as colored-coded lines from black (initial posture) to light blue (final posture). Dashed arrows indicate the direction of the tarsus tip and the plane normal movements during the respective phase. Abbreviations: a, anterior; p, posterior; m, medial; l, lateral; v, ventral; d, dorsal. **(B)** Analysis of the rotational range of the femur-tibia plane during the swing (left panels) and stance (right panels) phases. The range of plane

normal rotation for each analyzed step is represented by the angle between the plane normal of the initial and the final leg posture of the examined phase which was depicted in the left panel of the respective phase analysis. To compare DOF configurations, the absolute difference to the rotational range under control condition for each analyzed phase was depicted in the right panel of the respective phase analysis. Black solid lines represent the mean and the 95% CI of the absolute differences. Dashed horizontal black line indicates zero differences. The used DOF configuration is indicated in the x-axis labels (+: movable DOF, -: fixed DOF).

each step phase, the rotational range was larger than for model configurations without the ThCx-yaw DOF (**Figure 4.8B**), although a pronounced reduction of the range was observed (mean ± 95% CI for swing / stance: -19.5 ± 1.1 degrees / -23.5 ± 0.9 degrees). Interestingly, the combination of the ThCx-yaw and the CxTr-yaw DOFs resulted in a recovery of the rotational range, which was, however, slightly larger compared to the control DOF configuration (mean ± 95% CI for swing / stance: +2.1 ± 1.8 degrees / +1.0 ± 1.3 degrees) (**Figure 4.8B**).

Taken together, the ThCx-yaw and the CxTr-yaw DOFs were the main contributors of the kinematic model to the rotation of the femur-tibia plane of the middle legs. The finding that the rotational range was also slightly larger when only these two DOFs were used suggests that the other DOFs also have a small influence on the general orientation of the femur-tibia plane.

4.4 Discussion

In this chapter, a kinematic leg model for *Drosophila* was introduced, analysed in depth, and used to decompose the joint kinematics of forward walking. The obtained findings have not only implications for the technical aspects of kinematic modeling, but more importantly provide insights into the understanding of walking in *Drosophila*.

Although insects share a common blueprint for their legs (Snodgrass, 1935), there are numerous differences between species that are evident not only in the morphological appearance of leg segments, but also in the number of functional DOFs of the individual joints.

Therefore, the first aim was to determine the minimum number of DOFs required to accurately model the kinematics of tracked fruit flies for each leg pair by comparing the model error of a reference model (seven DOFs in total: ThCx, three DOFs; CxTr, one DOF; FeTi, one DOF; TiTar, two DOFs) to the resulting errors of a variety of alternative configurations of the kinematic leg chains with more or less DOFs. In the following paragraphs, the main findings and the results for joints with a focus on the ThCx and TrFe are discussed in detail.

One of the major findings was that the front legs required an additional roll DOF to allow rotation of the femur-tibia plane, while the reference model was already sufficient to adapt to the leg postures of middle and hind legs. This is in stark contrast to the kinematic model used in two previously studies (Goldsmith et al., 2022; Lobato-Rios et al., 2022), which are the only two 3D leg models for *Drosophila* published to date. Lobato-Rios et al. (2022) needed to add a roll DOF in all three leg pairs to prevent out-of-plane leg movements for their neuromechanical model of *Drosophila*. In addition, Goldsmith et al. (2022) aimed to determine the three most crucial DOFs in the middle and hind legs for the design of a *Drosophila*-inspired walking robot that can closely approximate the leg movements of real fruit flies. Under this assumption, they found that the combination of a CxTr-yaw, TrFe-roll, and FeTi-yaw was able to mimic the leg movements while balancing necessary robotic platform considerations. In this setting, they also concluded that the TrFe-roll DOF was necessary to prevent out-of-plane leg movements. One explanation why the TrFe-roll DOF was not required in the middle and hind legs in the kinematic model presented here might be that the main joint rotational axes based on anatomical landmarks, i.e. the joint condyles. In contrast, in both studies mentioned above, these axes were positioned rather generically in an orthogonal orientation with regard to the leg segments. This not only highlights the importance of considering anatomical axes for kinematic modeling, but also demonstrates that slanted joint axes, as often found in biological limbs, can yield evolutionary and functional benefits such as minimizing the number of required DOFs for specific movements. This notion is supported by the finding that the slanted and therefore non-orthogonal axes orientation between the two hinge joints that allow movements of the antennae in the stick insect improves the efficiency of active tactile sensing (Krause and Dürr, 2004).

In insects, the ThCx is assumed to be a ball-and-socket joint with three DOFs at least in the front legs, whereas the middle and hind legs typically use only two DOFs of the ThCx during forward stepping (Bender et al., 2010; Hughes, 1952). Moreover, in walking stick insects only one DOF is mainly involved in protraction and retraction, while the second DOF is little used for walking in all legs (Cruse and Bartling, 1995; Cruse et al., 2009). To determine the required number of DOFs for walking fruit flies, the resulting model error of different DOF configurations with one to three DOFs in the ThCx were compared. The best model fit for all legs was always achieved when the all three DOFs of the ThCx were available and at least two additional DOFs in the kinematic chain were needed to compensate the removal of a single DOF in the ThCx. In contrast to the other leg pairs, the front legs showed pronounced movements of the coxa, which were mainly governed by promotion and rotation via the pitch and the roll DOFs of the ThCx, respectively. However, adduction and abduction by the ThCx-yaw DOF were also observable. Moreover, the range of rotations of the coxa in the front legs was much larger than in the middle and hind legs. Such extensive use of all three DOFs accompanied by a pronounced rotation of the coxa was also previously observed in the front legs of the cockroach (Kram et al., 1997; Ritzmann et al., 2004; Tryba and Ritzmann, 2000). In contrast, the coxa of the middle and hind legs is not only smaller in *Drosophila*, but also did not exhibit marked movements. The ThCx mainly mediated promotion/remotion and adduction/abduction of coxa in these leg pairs. That is again similar to the middle and hind legs of the cockroach, although here the promotion/remotion of the coxa results rather in depression/levation due to the anatomical posture of these limbs (Bender et al., 2010). Although the roll DOF was less used in the middle and hind legs, its actions resulted in recurrent movement patterns specific for each leg pair during stepping.

Although the TrFe is moveable in many insects, its role in walking or other behaviors remains still elusive (Frantsevich and Wang, 2009). Because of the observed limited mobility of the TrFe and small size of the trochanter, the TrFe is commonly neglected in kinematic studies for the sake of simplicity and its role in walking was examined in only a few publications to date. In cockroaches, the TrFe is thought to assist in the initiation of the swing phase by lifting the tarsus from the ground through rotation of the tibia in the middle and hind legs, but not in the front legs (Bender et al., 2010; Szczecinski et al., 2014). Additionally, it was further proposed that the TrFe might compensate rotational constraints of the coxa and/or it might

act as damping mechanism counteracting disturbances by external forces during walking (Frantsevich and Wang, 2009). In this work, no conclusive evidence was found for or against the TrFe being used for forward walking in *Drosophila*. On the one hand, although many of the DOF configurations that showed an improved model fit included one or more DOFs in the TrFe in the middle and the hind legs, the model error was only slightly smaller compared to the reference model with a fixed TrFe. Based on this finding, however, it is impossible to decide whether the TrFe is moveable and contributes only little to walking or whether the kinematic model simply benefits from an additional DOF to minimize the distances between model and tracked leg keypoints. On the other hand, the TrFe-roll DOF was required to appropriately fit the kinematics of the front legs. However, the model error did not differ when the CxTr-roll DOF, as proposed by Lobato-Rios (2022), was used instead. The main argument for favoring the TrFe-roll over the CxTr-roll DOF in this model was that the CxTr is commonly described as hinge joint with only one DOF for levation and depression of the femur (Büschges et al., 2008; Cruse and Bartling, 1995; Cruse et al., 2009; Kram et al., 1997; Tryba and Ritzmann, 2000) and there is no evidence to date for the existence of an additional roll DOF of the CxTr in insects, whereas the trochanter has muscles innervated by the nervous system in *Drosophila* (Enriquez et al., 2015; Soler et al., 2004). In addition, the need for a movable TrFe to fit movements of the front legs but not for the other leg pairs was also found in a kinematic model of the cricket (Petrou and Webb, 2012). However, to definitively answer the question of whether the TrFe is functional in *Drosophila*, future studies focusing on a wider variety of locomotive behaviors or experimental manipulations such as optogenetic activation or inhibition of the muscles in the trochanter or the motor neurons that innervate those, for instance, are needed.

Interestingly, the front and the middle legs exhibited a rotation of the femur-tibia plane during stepping. This rotation was very prominent in the middle legs and seemed to contribute largely to protraction and retraction of the leg. In contrast, this rotation was rather unobtrusive in the front legs, but still necessary for modeling of the leg kinematics. Femur-tibia plane rotations were already reported for middle legs of the cockroaches (Bender et al., 2010) and *Drosophila* (Karashchuk et al., 2021) during walking. For the cockroach, it was proposed that this rotation emerges from actions of the TrFe (Bender et al., 2010). In the present model, a putative involvement of the TrFe for the femur-tibia plane rotations was only found for the

front legs. In the middle legs, surprisingly, these rotations were exerted by combined actions of the ThCx-yaw and CxTr-yaw DOFs, which can most likely be attributed to the alignment of their rotational axes. This not only emphasize the aforementioned importance of the orientation of anatomical axes for explaining leg kinematics, but also invites speculations about the relationship between leg morphology and the underlying motor control circuits in insect middle legs. For example, stick insects do not show such a prominent plane rotation in the middle legs and it is widely accepted that protraction/retraction and levation/depression of the leg during stepping is performed by the ThCx and the CxTr, respectively (Büschges et al., 2008). In the present *Drosophila* leg model, the very same movements emerged from rotations about the ThCx-yaw and CxTr-yaw DOFs. This could be interpreted to mean that similar neuronal commands are generated in both species to drive a basic leg stepping pattern, but morphological differences such as the orientation of joint rotational axes lead mainly to the huge dissimilarity in the observed movements of middle legs.

Some adaptations of the model were necessary to fit accurately the tarsal movements of the tracked animals. The tarsus of real fruit flies showed complex movements which are due to the fact that the tarsus consists of five segments linked by ball-and-socket joints (Tajiri et al., 2010). To simplify this complexity, the tarsus was modeled with two DOFs in the TiTar and its length was adjusted in a frame to frame manner, i.e. approximately 12-15 DOFs could be efficiently reduced to only three parameters. However, taken under consideration that *Drosophila* practise a kind of "toe walk" and the tarsus is the leg segment that interacts directly with the ground, the tarsus evidently has an important role for walking. From a biomechanical perspective, the tarsus comprises a large percentage of the total leg length, serves as adhesive pad and has a passive swing effect which contributes to ground force transmission (Manoonpong et al., 2021). Additionally, multiple campaniform sensilla have been found on the tarsus in *Drosophila* (Dinges et al., 2021), making it to a potential site for providing sensory feedback for mechanical load during walking. All of this suggests that a more detailed kinematic model of the tarsus will be needed in the future, particularly for dynamic simulations of *Drosophila* walking. On the other hand, tarsal segments do not have intrinsic muscles allowing independent control by the nervous system, but can be actively moved only together by muscle tension on the long tendon (Soler et al., 2004), which is known as retractor unguis apodeme in other insects. From studies in cockroach and stick insects, it was suggested

that active tension on the retractor unguis apodeme supports the leg lift-off at the beginning of the swing phase and influences the general stiffness of the tarsus (Frazier et al., 1999; Radnikov and Bässler, 1991). This further implies that observable tarsal movements are mediated, at least in part, by passive forces on the tarsus. Consequently, the present kinematic model with a simplified tarsus incorporates already the majority of joints which are under active control of the nervous system.

Other limitations of the modeling approach to determine the actual DOF configuration of *Drosophila* legs presented here must be mentioned. It is important to bear in mind that all findings discussed here are based only on tracked data of forward walking fruit flies. This means that individual DOFs that could be excluded by this model may still be required in other behaviors, locomotive or otherwise. For example, curve walking or turning in insects involves numerous adaptations of the leg kinematics (DeAngelis et al., 2019; Dürr and Ebeling, 2005; Gruhn et al., 2016; Jindrich and Full, 1999; Strauß and Heisenberg, 1990) and may also involve DOFs that are not used or used to a lesser extent during forward walking. In addition, although the joint orientations in the model were based on anatomical landmarks, only the rotational axes of yaw DOFs were derived directly from locations of the joint condyles. While this does not directly affect the conclusions for movements of the CxTr or the FeTi, as they were modeled as hinge joints with the yaw DOF being the only active DOF, it might have implications for interpretations for joints that include the pitch and/or the roll DOF of the model. For example, the rotational axes of all roll DOFs were placed along the leg segment to be influenced. However, the natural rotational axes could be also skewed, resulting in a tumbling rotation about the leg segment, which could affect the resulting angles of all other DOFs. Furthermore, the joint condyles were extracted from a single μCT of a female fly. Although the model could adapt appropriately to leg postures of all male and female flies examined in this work (e.g. see mean error time courses of individual flies in **Figure 4.3**), it cannot be, however, excluded that there are inter-individual differences in the location and orientation of the joint rotational axes in *Drosophila*. Another limitation is the lack of knowledge of the rotational ranges of the DOFs in *Drosophila*. It is generally challenging to make specific statements about the contribution of individual DOFs in an over-articulated limb system, because one DOF might be able to compensate the absence of another. Restricting the joint constraints to physiological ranges would at least limit this compensatory ability to

a natural level. Future morphological or kinematic studies should shed light on the natural orientation of all occurring joint axes and their range constraints. Additionally, kinematic studies could benefit from applying the systematically approach proposed here, i.e. hierarchical cluster analysis to sort a wide variety of DOF configurations according to their model error. Although this analysis was only helpful to draw conclusions for the front legs because the differences between the mean error of the tested DOF configurations were too small for the middle and the hind legs, the addition of leg postures from other locomotive behaviors that exhibit different leg kinematics compared to forward walking might narrow the number of DOF configurations that are capable to adapt to all presented leg postures.

Nevertheless, since each leg pair showed distinct kinematics, the results of the kinematic model presented here have some general implications for the demands of the underlying motor control system. The prevalent hypothesis of insect leg stepping is that each leg joint is controlled by a distinct CPG and the rhythmical activity of several CPGs is coupled by sensory feedback to generate coordinated leg stepping (Bidaye et al., 2018; Mantziaris et al., 2020). For instance, it is well-established that the fCO in insects encodes the position, velocity, acceleration, and vibration of the tibial movements (Büschges, 1994; Chockley et al., 2022; Mamiya et al., 2018; Matheson, 1990). However, the here presented kinematic data indicate that sensory feedback from the fCO might be shaped differently for the leg pairs with regard to the step phase they occur in. Although the extent of angular changes of the FeTi was comparable in front and hind legs, tibial flexion occurred during the stance or swing phase for front and hind legs, respectively, and vice versa during the opposite phase. That implies that the same sensory signal can mediate a different information about which step phase a leg is in. In addition, in the middle legs flexion and extension was less pronounced but occurred during both step phases. Hence, sensory feedback of the fCO must be integrated differently for each leg pair to contribute meaningfully to stepping. This notion is supported by a recent study by Chockley et al. (2022) which found that optogenetic inhibition of the fCO in *Drosophila* most strongly elongated the stance phase of the front legs and the swing phase of the hind legs. In addition, most knowledge of the neural mechanisms of CPGs in leg stepping emerged from studies of the middle leg of the stick insect (Mantziaris et al., 2020) and it is currently unknown whether all insects share the same CPG organization for all of their legs or if the CPG networks were evolved differently between species and/or between leg pairs to

allow distinct kinematic leg stepping patterns. However, it could also be that differences in leg kinematics arise from morphological differences such as joint structure or muscle arrangement. To answer this question, future biomechanical and neurobiological studies of insect walking should be more guided by the actual kinematic patterns of the individual legs of the species of interest.

Chapter 5

Kinematic synergies of straight walking in *Drosophila*

5.1 Introduction

To execute leg stepping during walking, the nervous system must cope with the problem of coordinating a number of joint DOFs in the legs that is larger than required for the task. Motor synergies were proposed as a general organizational principle of the nervous system to simplify the control of movement in such a redundant motor system (see **1.4**). Motor synergies represent the spatiotemporal coupling of the independent elemental units of the motor system, muscles or DOFs, for instance, and thus can be seen as the building blocks for complex movements (Bruton and O'Dwyer, 2018; Singh et al., 2018). In this notion, instead of having to constantly control all elemental units independently, the nervous system would generate complex movements by modulating the contribution and timing of a much smaller number of synergies. In fact, numerous studies found that the movement of individual body parts and segments are highly coupled and correlated across a wide variety of tasks (Balasubramaniam and Feldman, 2004; Bockemühl et al., 2010; d'Avella et al., 2003; Haid et al., 2018; Halliday et al., 2003; Majed et al., 2017; Santuz et al., 2019; Stetter et al., 2020; Wang et al., 2013).

Although motor synergies were already studied directly at the level of the nervous system by e.g. using microstimulation in the spinal cord of frogs and rats (Bizzi et al., 1991; Giszter et al., 1993; Tresch and Bizzi, 1999), these experiments are highly invasive, rather sophisticated, and might interfere with the natural behavior of interest. Therefore, most research on motor synergies to date relied on a behavioral approach, i.e. on recordings of the overall output of the elemental units of the motor system. When considering that one of the main features of synergies is the coordination between the elemental units, synergies can be examined by identifying covariations or correlations in the motor output. Motor synergies are thus typically studied by utilizing dimension reduction methods on movement data (Bruton and O'Dwyer, 2018) and consequently come in different variants depending on the type of the acquired data: Muscle synergies are derived from electromyograms (Barroso et al., 2014;

d'Avella et al., 2003; Nazifi et al., 2017; Singh et al., 2018), kinematic synergies are based on kinematic parameters such as e.g. joint angles (Bockemühl et al., 2010; Catavitello et al., 2018; Huang et al., 2021) or their Cartesian positions (Federolf et al., 2012; Stetter et al., 2020), and kinetic synergies are extracted from force measurement data (Hooke et al., 2012; Kipp et al., 2012; Santello and Soechting, 2000).

Dimension reduction methods are a natural choice for the identification of motor synergies from movement data because they exploit covariations in a redundant high-dimensional data set to transform the original values into a low-dimensional space while preserving as much information, i.e. variability, as possible from the original data set (for review: Ma and Zhu, 2013). Principal component analysis (PCA) is the most popular method for the analysis of kinematic synergies (Bockemühl et al., 2010; Bruton and O'Dwyer, 2018; Catavitello et al., 2018; Daffertshofer et al., 2004; Federolf, 2016; Schütz and Schack, 2013; Stetter et al., 2020; Tang et al., 2019; Wang et al., 2013). By identifying covariations or correlations between single variables in a data set, PCA constructs linear combinations of the original variables called principal components (PCs) which are ordered descendingly by the amount of variance they explain, i.e. the first PC captures more variance of the data set than the next PCs, and so on. Geometrically, PCs can be thought of representing the axes of a new coordinate system which is used to describe the original data set in directions of its largest variance. Although the number of PCs is identical to the number of variables, the first few PCs commonly explain most of the variance in the data set which consequently allows the reduction of dimensionality by omitting the subsequent PCs from the following analyses.

In terms of kinematic synergies derived from parameters such as e.g. joint angles, the rationale for using PCA is that if movements of limb segments are coupled, the joint angles should co-vary (Bockemühl et al., 2010; Schütz and Schack, 2013). Moreover, the more the coupling is synchronized and the covariance between joint angles is constant, i.e. can be described by a fixed magnitude ratio, the more the underlying coordination can be described as a linear relationship which can be captured by PCA. The resulting PCs are interpreted as follows: the PCs accounting for the majority of variance represent the invariant patterns of the motor output, i.e. the kinematic synergies, whereas PCs accounting for only a small fraction of

variance capture random noise of the motor system or the measurement method and can therefore be neglected (Wang et al., 2013).

Since behavioral motor synergies are derived from movement data, they however do not allow direct inference of how the nervous system generates an appropriated motor output, but should rather be interpreted as theoretical constructs which are nonetheless related to functioning of the nervous system (Federolf, 2016; Wang et al., 2013). In addition, it was also argued that identified synergies might rather reflect the biomechanical constraints of a studied task and the experimental conditions than the underlying neural control strategy (Lambert-Shirzad and Van der Loos, 2016; Rearick et al., 2003; Steele et al., 2015; Todorov and Ghahramani, 2004). Nevertheless, there is accumulating evidence that identified motor synergies can be shared between different tasks (Barroso et al., 2014; d'Avella and Bizzi, 2005; Huang et al., 2021; Nazifi et al., 2017; Stetter et al., 2020) or even between animals (Catavitello et al., 2018) and it was suggested that, at least in vertebrates, a flexible neural network substrate for the control of functional synergies, i.e. motor synergies as defined here, exists (McMorland et al., 2015). This supports the notion that behavioral motor synergies can indeed serve to formulate hypotheses for the underlying motor control mechanisms of the nervous system.

Although some studies used dimension reduction methods on kinematic parameters to analyze walking in *Drosophila* (e.g. DeAngelis et al., 2019; Karashchuk et al., 2021), there is no study to date that investigated kinematic synergies at the leg joint level in *Drosophila* in detail. Hence, PCA was utilized in this thesis to identify and analyze kinematic synergies derived from the angular time courses of the leg joint DOFs of straight walking fruit flies.

5.2 Material and methods

5.2.1 Extraction of kinematic synergies by PCA

Kinematic synergies were extracted by performing PCA. Mathematically, PCA decomposes the covariance matrix or the correlation matrix of the original data set into the PC eigenvectors, eigenvalues, and scores (Bockemühl et al., 2010; Daffertshofer et al., 2004; Jolliffe

and Cadima, 2016; Stetter et al., 2020). The eigenvectors represent the PCs and thus indicate the directions of the largest variations in the data set. In addition, each eigenvector consists of the coefficients which describe the contribution for each variable of the data set to the respective PC. The eigenvalues indicate the amount of the total variance accounted for by each PC and therefore is used to order the PCs. Finally, the scores represent the projections of the original variables onto each PC, i.e. they describe the location of all values in the coordinate system of the PC space.

Since the main goal of the analysis presented here was to identify general kinematic synergies for straight walking in *Drosophila*, independent PCAs were performed on the mean angles time courses of the DOFs for each leg pair and fly (see **Figure 4.7**). This effectively minimized the influence of leg-specific differences as well as inter-individual and step-to-step variability on the resulting PCs and thus allowed to identify independent movement patterns shared by individual flies for each leg pair.

Prior to PCA, data sets had to be normalized in order to prevent bias from different units or ranges of the original variables. For this, the joint angle time curves for each DOF were centered by subtracting their mean. Because all variables had the same unit, i.e. angular degrees, further normalization by dividing through the SD to obtain z-scores was not performed (this step is often performed when the variables on which the PCA is based have very different absolute amplitudes or units). Consequently, the performed PCAs was based on the covariance matrix of the joint angle data. As a consequence, single DOFs which show larger variations during a leg step than others might dominate the resulting PCs. The implications of using the covariance matrix on the resulting PCs are addressed further in the discussion (see **5.4**). Eventually, all PCAs were performed using the decomposition package of the Scikit-learn software library version 0.24.2 (Pedregosa et al., 2011).

There are various methods proposed to determine the minimum number of PCs that is sufficient to capture most of the variance in the data set (Peres-Neto et al., 2005; Valle et al., 1999; Wang et al., 2013). However, since the decision which PCs must be retained (because they contain relevant information) or which PCs can be omitted (because they mainly capture noise) strongly depends on the underlying data set, the number of relevant PCs might differ between methods and must be interpreted in the light of data set. Thus, two commonly used

criteria for the minimum number of PCs were evaluated in this analysis. First, the explained variance of each PC was compared to the hypothetical explained variance that can be expected from an uncorrelated data set with the same overall statistics, i.e. the joint angles would not co-vary (Peres-Neto et al., 2005). For this, the time course of joint angles for each DOF was randomly permutated which resulted in a data set with the same size and values, but in which any systematic relationship between joint angles that formed the natural leg postures was broken. When the explained variance of a PC based on the original joint angle data set was higher than that of the hypothetical data set, this PC should be retained. The second criterion used here based on the cumulative percent variance to determine the minimum number of PCs (Bockemühl et al., 2010; Valle et al., 1999; Wang et al., 2013). Since the first PCs usually capture most of the total variance in the data set, PCs were retained until the cumulative fraction of explained variance was equal or exceeded a 95% of the total variance.

5.2.2 Reconstruction of movements from PCs

Since PCA projects the original data set into a new PC space, the PC scores can also be transformed back into the joint angle space by reversing the calculations. For each DOF, the products of the score (s) and coefficient (c) of the DOF for each of the used PCs (n) were summed and added to the mean angle of this DOFs (**Eq. 5.1**).

$$angle_{DOF} = mean_{DOF} + \sum_{i=1}^{n} s_{DOF_i} c_{DOF_i} \tag{5.1}$$

Importantly, the original data set can be completely recovered when all PCs are used, while a reduced set of PCs can only approximate the original data set (Bockemühl et al., 2010). Nevertheless, since the loss of accuracy depends on the cumulative fraction of explained variance of the number of PCs used, reconstructed joint angles from a smaller set of PCs typically contain the main aspects of the underlying leg postures. To eventually obtain leg postures from the reconstructed joint angle data sets, the joint angles were inserted into the previously described kinematic leg model (see **chapter 4**).

5.3 Results

5.3.1 PCA of mean steps from individual flies

PCA showed that a few PCs were able to sufficiently capture the variance, i.e. changes of joint angles to adopt the leg postures occurring within the mean steps, for all flies and leg pairs (**Figure 5.1A**). The first PC already accounted for a very large percentage of variance with 86.7 ± 3.1% and 94.2 ± 2.8% for the front and hind legs, respectively. In addition, the explained variance for the second and third PC was higher for the front legs (PC2: 10.0 ± 2.6%; PC3: 2.4 ± 0.7%) than for the hind legs (PC2: 4.9 ± 2.6%; PC3: 0.56 ± 0.19%). In contrast, the first PC captured less variance (67.6 ± 7.8%) for the middle legs and its amount varied more between flies (**Figure 5.1A**). Moreover, while the explained variance of the second PC (25.5 ± 6.9%) was much higher for the middle legs, the amount of variance captured by the third PC (5.9 ± 2.0%) was similar compared with the other legs. The remaining PCs for all legs accounted in average for less than 1% of the total variance (front legs: 0.8 ± 0.2%; middle legs: 0.9 ± 0.6%; hind legs: 0.3 ± 0.1%). In general, these findings indicate strong couplings between the involved joint angles in all legs.

Next, the minimal number of PCs required to sufficiently reconstruct the observed leg postures was determined. When comparing the explained variance of individual PCs to the respective mean captured variance of the permutated data sets, values for PC1 were higher for all flies and legs (**Figure 5.1A**). In contrast, the captured variance of the second PC was only higher in 7 of 12 flies for the middle legs than for its permutated counterpart, and the third PC never captured more variance than in the permutated data sets. However, the explained variance for the permutated data sets was relatively high for the first three PCs, suggesting that a few joint angle variables dominated the data sets even when permutated, most likely due to their wider angular range. When the second criterion used here, i.e. accepting all PCs required to explain at least 95% of the total variance, was evaluated, the first two PCs explained more than 95% of variance for the front and hind legs of all flies, but for the middle legs the third PC was required to reach the 95% cut-off criterion for over 80% of flies (**Figure 5.1B**). Additionally, for about half of the flies, the first PC of the hind legs was

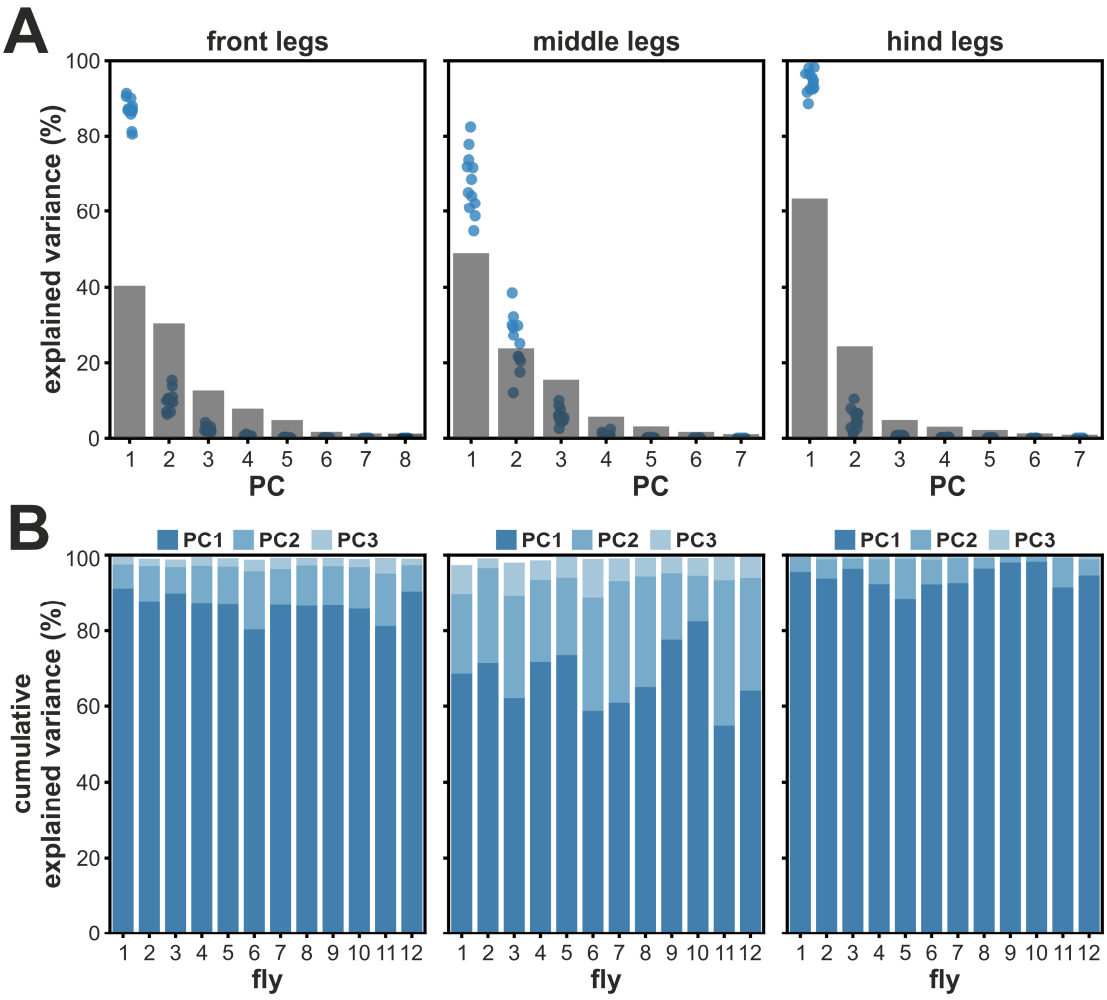

Figure 5.1. Variance explained by PCA. (**A**) Explained variance of PCA for front, middle, and hind legs. Filled blue circles represent individual flies (n=12), while gray bars display the mean explained variance from permutated versions of all data sets. (**B**) Cumulative explained variance of the first three PCs of individual flies for front, middle, and hind legs.

already sufficient to explain more than 95% of variance, while two PCs were needed to meet this criterion for the front legs.

In conclusion, although one or two PCs for all legs were sufficient to meet the evaluated criteria for the majority of flies, the cumulative explained variances of the first three PCs was almost always over 99% and never lower than 97.4% (**Figure 5.1B**). Thus, the first three PCs were considered for the following analyses to better compare the results between all flies. Moreover, even when more PCs were used than might be necessary to adequately reconstruct the joint angles for the respective leg postures of individual flies, the reduction of

dimensionality was still high considering that three variables were enough to model the underlying joint angles of seven to eight DOFs.

5.3.2 Evaluation of single PCs

Since each PC consists of a constant coefficients vector and a varying score vector describing the relationship between the PC and the underlying DOFs of a leg and the required scaling factor to obtain different sets of angles from this PC, respectively, the time course of scores can be interpreted as a kind of time-varying control signal for the kinematic synergy represented by a PC. Strikingly, the time courses of the scores showed very similar shapes for the evaluated PCs of the individual legs for all flies, except for PC1 and PC2 of the middle legs in three flies (**Figure 5.2**). For PC1, the scores decreased steadily from the beginning during the swing phase and increased continuously during the stance phase, forming a cosine-like pattern with relatively constant amplitudes for each leg. Interestingly, the minimum of the scores were reached at the transition between swing and stance or shortly after for the front and hind legs, respectively, while its timing varied more around the swing-to-stance transition for the middle legs (**Figure 5.2**).

The majority of scores' time courses of PC2 of middle and hind legs exhibited an inverted sinus-like shape and their amplitudes varied more between individual flies (**Figure 5.2B+C**). In contrast, front leg PC2 scores increased during the swing phase either constantly or until they reached a plateau at the middle of the swing phase, while the shape of their time course was similar to the other legs during the stance phase, i.e. they increased until the middle of the stance phase and decreased afterwards (**Figure 5.2A**). Additionally, the time courses for PC3 scores for all legs resembled a W-like pattern, i.e. during both the swing and stance phase, the scores decreased from the beginning to the middle of the respective phase and increased afterwards until the end of the phase (**Figure 5.2**).

Interestingly, with respect to the middle legs, three flies exhibited time courses of PC1 scores that were more similar to those of PC2 from the other flies when flipped (**Figure 5.2B**: pink lines vs. blue lines). Correspondingly, the PC2 scores' time courses of these flies were more comparable to PC1 score courses of the other flies even without flipping. One explanation for

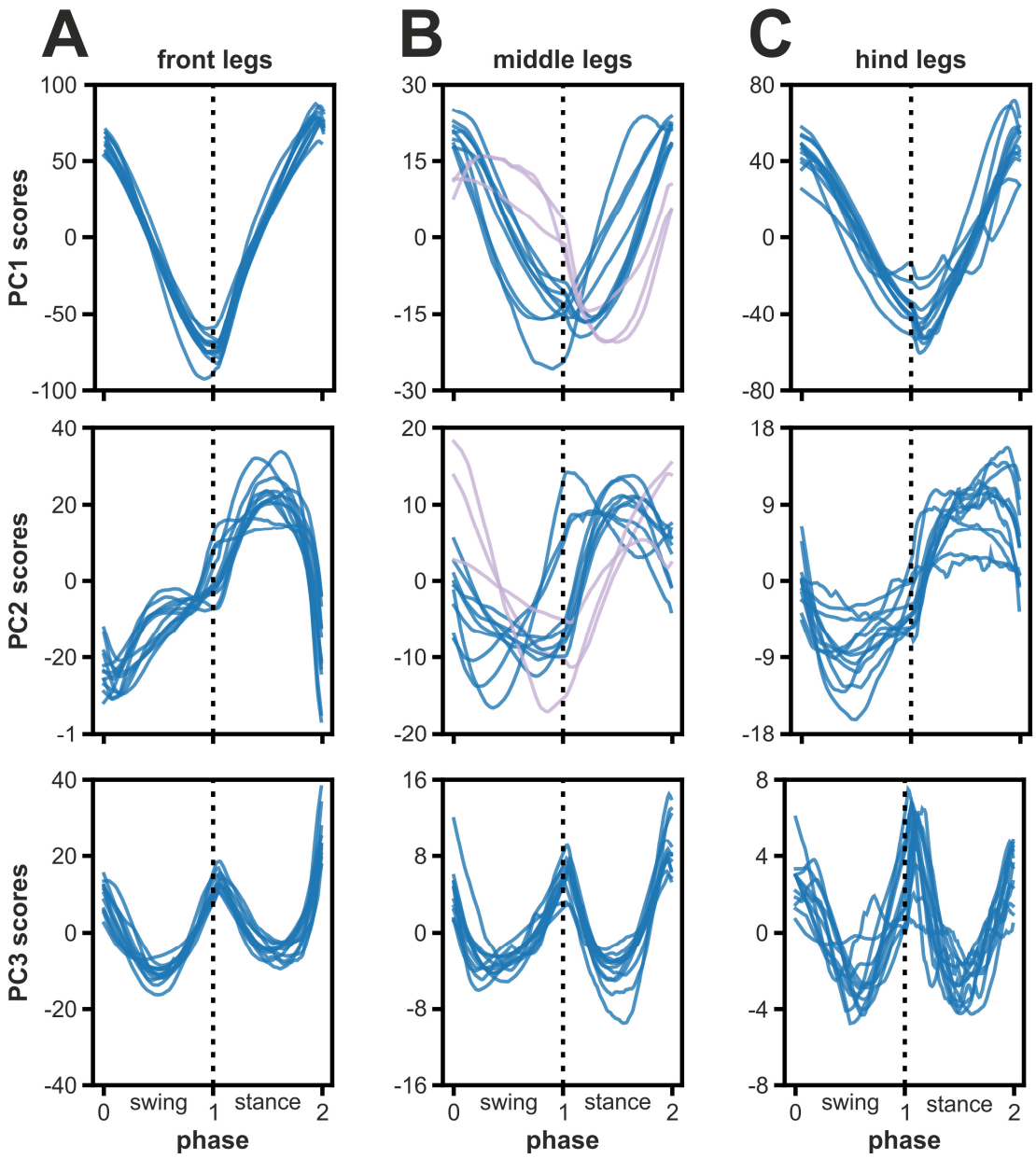

Figure 5.2. Time courses of scores from single PCs. Scores of the first three PCs are shown for the front (**A**), middle (**B**), and hind (**C**) legs for individual flies (n=12). For the middle legs, the pinkish lines highlight score time courses of flies for which PC1 and PC2 seemed to be swapped, i.e. the time courses of PC1 exhibit a similar shape when flipped compared to the time courses of PC2, while PC2 time courses resemble those of PC1 from the other flies. Time courses are normalized to step cycle phase (zero to one: swing/ one to two: stance) and dashed black lines indicate the transition from swing to stance.

this observation might be that PC1 and PC2 together describe a similar 2D plane in the joint angle space for all flies, but which of these two PCs explains most of the variance was determined by inter-individual variations in the mean steps between the flies.

Since the coefficients of each PC can be interpreted as the strength of coupling between the leg DOFs within the respective PC, the magnitude of a coefficient for a single DOF allows to draw conclusion about the contribution of this DOF to the respective PC (**Figure 5.3**). Coefficients of PC1 did not differ much between flies for the front middle legs, whereas they varied more for the middle legs. Strikingly, for all legs, PC1 was mainly dominated by CxTr-yaw and FeTi-yaw. Further contributions of additional DOFs to PC1 were observable for each leg (front: ThCx-roll and ThCx-pitch; middle: ThCx-yaw; hind: TiTar-pitch) as indicated by median coefficients with magnitudes over 0.2. The direction of all coefficients was identical for PC1 of the front and hind legs, but ThCx-yaw was negatively correlated with CxTr-yaw and FeTi-yaw in the middle legs. In contrast, PC2 and PC3 were dominated by different groups of DOFs with respect to the legs and coefficients were more variable between flies than observed for PC1 (**Figure 5.3**). Interestingly, the coefficients of PC2 and PC3 of the front legs for all flies showed the same direction for the main contributing DOFs and the variability between flies was lower compared to the other legs.

To obtain a more intuitive description of the main aspects of captured movements by the first three PCs, leg movements were reconstructed by using a single PC at a time. Strikingly, PC1 captured most of the protraction and retraction movements of all legs in the majority of flies, i.e. PC1 mainly captured the straightening and flexing of the front and hind legs for all flies, while it accounted mostly for promotion and remotion of the coxa of the middle legs in 10 of 12 analyzed flies. However, PC1 drove also flexion and extension of the tibia of the middle legs in 6 of 12 analyzed flies and this was the main observed movements in the two flies which did not show protraction/retraction movements in PC1.

In contrast, reconstructions based on PC2 resulted in depression and levation movements of the front and hind legs. Additionally, PC2 was also associated with rotational movements of the coxa and the femur of the front legs. For the middle legs, however, PC2 captured a mixture of leg movements, i.e. reconstructions exhibited primarily leg promotion/remotion of the coxa in 7 of 12 flies, levation/depression in 5 of 12 flies, and tibial flexion/extension in 2 of 12 flies.

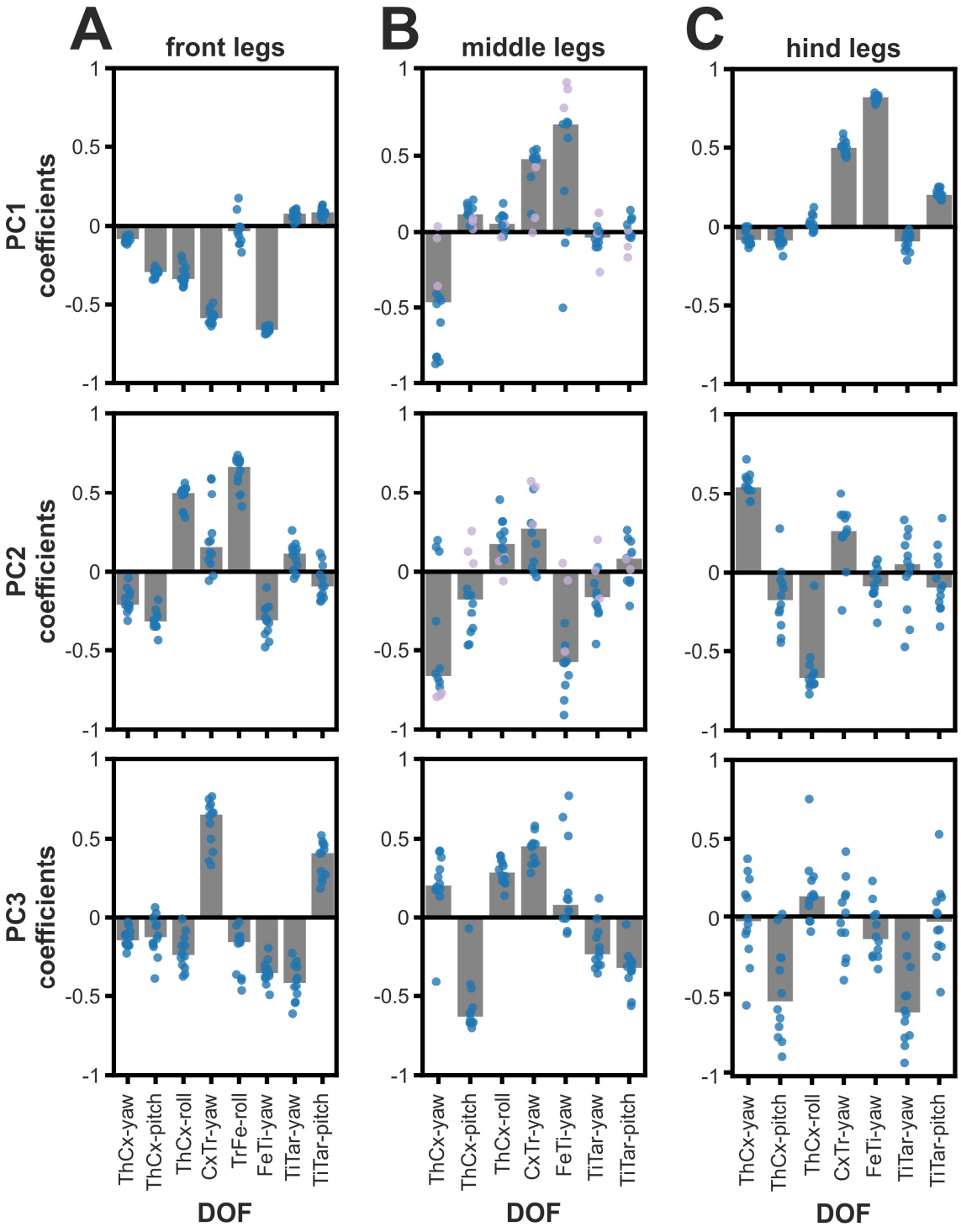

Figure 5.3. Coupling strengths between DOFs in single PCs. The coupling strength is expressed by the coefficients of the individual PCs. Coefficients of PC1 (upper panels), PC2 (middle panels), and PC3 (lower panels) are displayed for front (**A**), middle (**B**), and hind (**C**) legs. Filled circles represent the coefficients for individual flies (n=12), while gray bars represent the median for each DOF in the respective PC. For middle legs, pink filled circles highlight flies in which PC score time courses seem to be swapped between PC1 and PC2 (see text and **Figure 5.2**).

Importantly, promotion/remotion of the coxa was more pronounced in flies which did not already show movements of the coxa in reconstructions from PC1. In addition, PC3 mainly resulted in leg levation/depression in the front and middle legs for all flies. For the hind legs, however, reconstructions based on PC3 resulted in levation/depression in only two flies, while mainly slight promotion/remotion of the coxa was observed in the other flies.

5.3.3 Reconstruction of tarsus tip movements by PCs

When considering that propulsion of the body in *Drosophila* is mainly driven by force transmission of the tarsal tips to the ground in the stance phase, it can be assumed that the generation of an appropriate trajectory of the tarsal tips constitutes one of the main goals for the motor control of leg movements during walking. Thus, the next step was to evaluate how well the kinematic synergies, i.e. the PCs derived from PCA, were able to reconstruct the tarsus trajectory of the legs. Since reconstructions of leg movements for both body sides was based on the same PCs, the resulting trajectories were identical, except for the fact that the positions in the transversal plane were mirrored. Therefore, only the trajectories of the tarsal tips from the right body side were considered in the following analysis.

The mean trajectory of the tarsus tip of the mean steps from all flies (n=12) showed for all legs an ellipsoid-like shape in the transverse plane, while it was rather semicircular-like or governed by the ball surface of the motion capture setup in the sagittal plane during the swing and stance phase, respectively (**Figure 5.4A**). Additionally, the mean steps between flies were more variable in the sagittal plane than in the transverse plane as indicated by the higher standard deviation (**Figure 5.4A**). When only PC1 was used for reconstruction, the tarsus tip of the front and hind leg was moved only on a line in both planes and thus failed to reconstitute the majority of the trajectories, particularly in the sagittal plane (**Figure 5.4B**). In addition, although the reconstructed mean trajectory exhibited an ellipsoid-like shape for the middle leg, the original mean trajectory was not recovered accurately. In contrast, reconstructions based on the first two PCs were able to fit largely the original tarsal tips trajectories of the legs (**Figure 5.4B**). However, the reconstructed trajectory still deviated noticeably in the sagittal plane for the front leg and the middle leg when only two PCs were

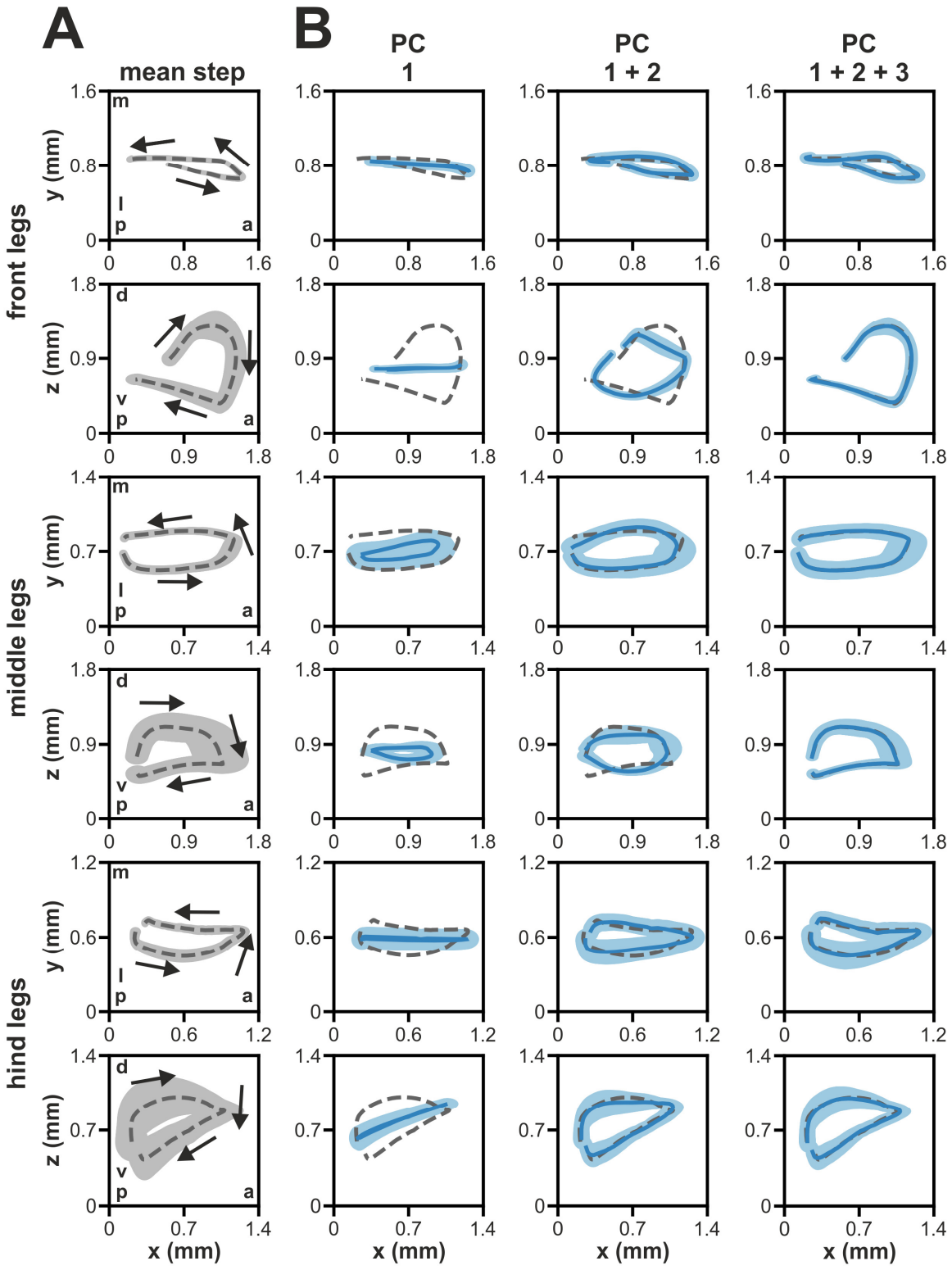

Figure 5.4. Reconstruction of tarsus trajectory for legs of the right body side. The trajectory of the tarsus is shown for front, middle, and hind legs. For each leg, positions of the tarsus are shown for transversal plane view (x-y; upper panels) and sagittal plane view (x-z; lower panel). (**A**) Original tarsus tip trajectory. Dashed gray lines represent the mean trajectory derived from mean steps of all flies (n=12) and the gray areas indicate the SD. Arrows indicate the direction of the tarsus movements from start of

the swing phase to end of stance phase. (**B**) Tarsus trajectory reconstructed from either the first (left panels), first two (middle panels), and first three (right panels) PCs. Blue lines represent the resulting mean trajectory of all reconstructed trajectories, while blue areas exhibit the 95% CI. Abbreviations: a, anterior; p, posterior; m, medial; l, lateral; d, dorsal; v, ventral.

used. Eventually, a high correspondence between the original and the reconstructed trajectory was achieved by using the first three PCs (**Figure 5.4B**).

5.4 Discussion

For all legs, the first three PCs not only explained almost all of the variance in the DOF angle time courses, but were also sufficient to reconstruct the movements of the tarsus tip with high accuracy. This means that the coordination of leg movements in straight walking fruit flies can be captured by only three linear kinematic synergies. In other words, the problem of controlling seven to eight joint DOFs can essentially be reduced to a three-dimensional control space. That further indicates that a bijective, i.e. one-to-one, mapping between the 3D PC space and the 3D Cartesian space is possible, suggesting that the redundancy problem could be simply solved at least for movements of the tarsus tip.

Strikingly, leg protraction/retraction was the dominant movement pattern for PC1 for all legs in most flies and the scores' time courses of all PCs were similar between flies. This suggests that all leg pairs could principally be controlled by congeneric motor or pre-motor activation patterns, although the stepping movements of the leg pairs differed in terms of joint angle time courses and use of DOFs (see **Figure 4.7**). However, despite the fact that time courses were comparable for most PCs, the shape of PC2 time courses for the front legs deviated from the middle and hind legs at the swing phase and at the end of the stance phase. This is presumably explained by the use of the TrFe-roll DOF in the front legs, since PC2 captured most of its joint angle changes as indicated by the high coefficient for this DOF (**Figure 5.3A**).

The coefficients for many PCs were comparable across flies to a great extent. However, there were qualitative differences between the individual leg pairs. All PCs for the front legs showed the lowest variability between flies, while the coefficients for single or multiple DOFs in the middle and hind legs exhibited not only more varying coupling strengths but also different signs for some flies (**Figure 5.3**). One interpretation of this finding is that the stepping pattern of the front legs in *Drosophila* is more stereotypic than that of the other leg pairs and therefore can be better captured by the same PCs. Following this view and considering that PCs are ordered according to their importance for the leg movements, stepping of the hind legs is more similar between flies than stepping of the middle legs, since PC1 of the hind legs exhibited very similar coefficients, whereas only PC3 showed less variability of the coefficients for the middle legs. This is, however, a surprising finding, because the front legs seemed to show the most complex movements during walking and had more joint DOFs.

While the first two PCs exhibited one oscillation for a complete step, the time courses of PC3 scores consistently oscillated at twice the stepping frequency and thus PC3 contributed equally to stepping during the swing and the stance phase. The occurrence of such phase relationship between the first few PCs were also observed in human walking and was associated with higher-frequency secondary features of body movement during walking. For instance, PCs with a doubled frequency was found by Daffertshofer et al. (2004) for the second and fourth PC, which captured knee and ankle bending or body sway, respectively. Additionally, Troje (2002) identified such a phase relationship for the third and fourth PC, which represented a hop-like or bounce-like motion of the body. However, both studies not only studied bipedal walkers, but also utilized a set of body markers for the whole body and analyzed their positional changes which is in contrast to the approach applied here, i.e. an independent joint angle-based analysis for each leg pair. Although a direct comparison is therefore not possible, the repeated observation of movement components oscillating at twice the stepping frequency points toward a general aspect of walking movements across species.

Although already two PCs explained over 90% of the total variance in most flies for all legs and the third PC seemed to contribute only little, three PCs were required for an accurate reconstruction of the tarsus trajectory for at least the front and middle legs. This suggests that in terms of kinematic synergies, the use of traditional cut-off criteria to determine the

minimum number of PCs should be used with caution and additional considerations, such as positioning the end-effector (tarsus tip) in 3D Cartesian space, must be taken into account. Another interpretation of this observation is that even when reconstructed joint angles match the original joint angles very closely, the resulting movements might still show a larger discrepancy. For instance, when considering that motions of a joint DOF affects the positions of all subsequent joints in a kinematic chain (see **chapter 4**), e.g. motions of the ThCx as the first joint of insect legs influence the whole leg posture in *Drosophila*, already subtle differences in angles can result in meaningful changes of the final posture and tarsal position. This further argues for a general use of kinematic models, if available, to validate kinematic synergies derived from PCAs of joint angles.

Data normalization is a crucial step for PCA and the results depend on whether the covariance (non-normalized) or correlation matrix (normalized) is used (Jolliffe and Cadima, 2016; Wang et al., 2013). Using the covariance matrix results in greater coefficients in the PCs for variables that vary over a larger absolute range, whereas the correlation matrix is agnostic to the range covered by variables because the amplitudes for each variable is normalized separately. Additionally, the use of the covariance matrix usually results also in a larger fraction of explained variance for the first PCs (Jolliffe and Cadima, 2016; Wang et al., 2013). Here, the covariance matrix was used and joint DOFs with larger angle ranges are likely to dominate the PCs. Consequently, while the contribution of single DOFs to a PCs might have been partly obfuscated by this normalization approach, DOFs were highlighted that were more important for the underlying leg movements as they had to vary over a wider range.

Although the consistency of the kinematic synergies found here for straight walking between flies argues for the existence of a common control mechanism based on the coupling of joint DOFs, how these synergies might be embedded in the nervous system is a difficult question to answer. Since the kinematic synergies were derived here from the overall motor output at the behavioral level, i.e. changes in joint angles, they do not allow to draw direct conclusions for the individual contributions of the output of the motor neurons, the underlying muscle physiology and their activation patterns, other biomechanical constrains such as interaction torques that arise by mechanical coupling between the leg segments, as well as sensory feedback influencing the movement patterns identified by the individual PCs (Bockemühl et

al., 2010). As such, the kinematic synergies are relatively abstract and combine the contributions of all of these levels in a holistic manner.

Studying muscle synergies might be an alternative to obtain results that are closer to the output of the nervous system. However, the methods used to date for recording muscle activity in *Drosophila* might interfere with the natural walking behavior. Muscle activity can be measured either by using electrodes to perform extracellular recordings (Akitake et al., 2015; Azevedo et al., 2020; Jin et al., 1998) or by using calcium imaging (Azevedo et al., 2020; Lehmann et al., 2013; Lindsay et al., 2017). Extracellular recordings are, however, highly invasive since the electrode must be poked through the cuticle and consequently the leg segment containing the muscle of interest must be immobilized. In addition, extracellular recordings usually allow only the simultaneous investigation of a limited number of muscles (Lindsay et al., 2017). In contrast, although calcium imaging allows simultaneous recording of all muscles expressing a calcium indicator protein directly through the cuticle (Vajente et al., 2020), the temporal resolution is much lower compared to extracellular recordings (Lindsay et al., 2017) and, with respect to leg muscles, it requires also immobilization of leg segments to prevent movement artefacts (Azevedo et al., 2020). Recently, however, another much more promising experimental approach was developed. Two studies demonstrated that it is possible to perform calcium imaging of neurons of the ventral nerve cord in walking fruit flies (Chen et al., 2018; Hermans et al., 2022). This would allow for the examination of kinematic synergies in direct relation to the output of motor neurons or other neuron populations associated with the motor control of walking, provided that a sufficient temporal resolution can be achieved (Chiappe and Jayaraman, 2012).

Chapter 6

General discussion and future outlook

In this dissertation, I established an experimental platform based on a motion capture setup for the precise spatiotemporal tracking of leg joint positions in 3D (**chapter 3**) and a kinematic leg model used here to extract the joint angles of forward walking fruit flies (**chapter 4**). Finally, I used the angle time courses of all joint DOFs obtained from the kinematic model to identify and analyze kinematic synergies for forward walking in *Drosophila* (**chapter 5**).

Since the anatomical DOF configuration of the leg joints in Drosophila is currently unknown, the kinematic model was extremely useful for determining a putative DOF configurations for all leg pairs. For this, the model error, i.e. the distance between the joint positions of the model and the motion capture data, was evaluated after fitting the model to the motion capture data (see **4.3**). An appropriated model fit was achieved when the middle and hind legs were equipped with seven joint DOFs (ThCx, three DOFs; CxTr, one DOF; FeTi, one DOF; TiTar, two DOFs). In contrast, the front legs required an additional roll DOF in the TrFe.

The main advantage of kinematic leg model presented here, in contrast to the other two previously published models for *Drosophila* legs (Goldsmith et al., 2022; Lobato-Rios et al., 2022), is that it takes into account the anatomical orientation of the main rotational axes of each joint. As a result, an additional DOF in the CxTr or TrFe was not required in the middle and hind legs to prevent out-of-plane leg movements (see **4.3.4**). This was particularly surprising for the middle legs as they exhibited a pronounced rotation of the femur-tibia plane during stepping, which at first glance argues for an additional roll DOF close to the femur. However, in the kinematic model presented here, this rotation resulted from the combined movements of the ThCx and the CxTr (see **4.3.7**). Interestingly, both joints were already associated with other essential movement components of stepping, i.e. the ThCx and CxTr were mainly responsible for protraction/retraction and levation/depression in the middle legs, respectively. This suggests that the natural movement repertoire of legs can be expanded through biomechanical interactions between joints without directly increasing the demands on the nervous system for motor control.

In addition, a roll DOF in the TrFe was required to adequately fit the kinematic model to the movements of the front legs (see **4.3.4**). This provides new arguments for the debate on whether the TrFe is mobile in *Drosophila* legs (Goldsmith et al., 2022; Lobato-Rios et al., 2022). Although a mobile TrFe was not required to model forward walking in the other leg pairs, it cannot be excluded that the TrFe of the middle and hind legs is involved in other walking behaviors such as e.g. curve walking. Hence, further studies are needed to conclusively answer the question of whether the TrFe is functional in *Drosophila*. An elegant approach might be to analyze the effects of optogenetic activation or inhibition of the muscles of the trochanter or the motor neurons innervating them on a range of natural occurring leg movements.

The aforementioned findings obtained from the kinematic model are also critical for developing more sophisticated models of leg movements in *Drosophila*. Dynamic models for determination of joint torques (e.g. Dallmann et al., 2016) , musculoskeletal models (e.g. Full and Ahn, 1995), and complete neuromechanical models (e.g. Guo et al., 2018; Lobato-Rios et al., 2022) are all build on top of a kinematic model that specifies the allowed direction and ranges of leg segment movements during walking. Consequently, deviations from the natural occurring joint DOFs and their rotational axes could lead to misleading results from these models.

Although the kinematic leg model presented here can serve as a starting point for such models in future, there are still gaps to be filled in our understanding of the leg kinematics in *Drosophila*. For instance, the complexity of the tarsus was simplified in the kinematic model used here. Instead of modeling all five segments which are linked by ball-and-socket joints (Tajiri et al., 2010), i.e. the tarsus has approximately 12-15 DOFs, here movements of the tarsus were modeled by only three parameters. Additionally, despite the rotational axis of the first DOF of each joint, referred to as yaw in this dissertation, was derived from the locations of the joint condyles, the real anatomical orientations of rotational axes of the other DOFs, i.e. pitch and roll, in joints such as the ThCx are not yet known. Another limitation is the lack of knowledge of the physiological rotational ranges of the joint DOFs. These points should be addressed in future morphological, biomechanical, and kinematic studies.

Strikingly, the results of the PCA of the mean angle time course of the joint DOFs showed that three kinematic synergies, i.e. PCs, were sufficient to reconstruct very accurately the movements of the tarsus tip of all three leg pairs during stepping (see **5.3.3**). This implies that the control of seven to eight joint DOFs can be shifted in a hypothetical three-dimensional motor synergy control space. Importantly, this further suggests that a bijective, i.e. one-to-one, mapping is possible between the position of the tarsus tip in the 3D Cartesian space and the 3D kinematic synergy space. This would simply solve the redundancy problem, at least with respect to the movements of the tarsus tip. Additionally, despite all leg pair showed distinct kinematics in terms of joint DOFs (see **4.3.6**), the time courses of all PCs were relatively similar between flies and the first PC captured mainly leg protraction/retraction for all leg pairs. This suggests that the nervous system could theoretically control all leg pairs by the same congeneric motor or pre-motor activation patterns.

Although kinematic synergies combine the contributions of all neuromechanical components of the motor apparatus and thus do not allow direct inference for the exact role of the nervous system, these finding demonstrate that a coordinative structure exists and the nervous system would benefit from using it to simplify the motor control of walking. Since in this dissertation kinematic synergies were only extracted from forward walking fruit flies, future studies should aim to identify kinematic synergies in other walking behaviors such as e.g. curve walking or backwards walking. Thereby, it would be possible to find shared kinematic synergies across different locomotor behaviors which in turn would argue for an underlying common coordination scheme (e.g. Huang et al., 2021; Stetter et al., 2020).

In conclusion, this dissertation provides detailed insights into the leg joint kinematics of *Drosophila* which are relevant for deciphering motor control of walking in insects. When combined with the extensive genetic toolbox offered by *Drosophila* as model organism, the experimental platform presented here, i.e. the 3D motion capture setup and the kinematic leg model, will facilitate deeper investigations of *Drosophila* walking behavior in the future.

List of Figures

List of Tables

References

Akay, T., Bässler, U., Gerharz, P. and Büschges, A. (2001). The Role of Sensory Signals From the Insect Coxa-Trochanteral Joint in Controlling Motor Activity of the Femur-Tibia Joint. *Journal of Neurophysiology* **85**, 594–604.

Akay, T., Haehn, S., Schmitz, J. and Büschges, A. (2004). Signals From Load Sensors Underlie Interjoint Coordination During Stepping Movements of the Stick Insect Leg. *Journal of Neurophysiology* **92**, 42–51.

Akay, T., Ludwar, B. Ch., Göritz, M. L., Schmitz, J. and Büschges, A. (2007). Segment Specificity of Load Signal Processing Depends on Walking Direction in the Stick Insect Leg Muscle Control System. *J. Neurosci.* **27**, 3285–3294.

Akitake, B., Ren, Q., Boiko, N., Ni, J., Sokabe, T., Stockand, J. D., Eaton, B. A. and Montell, C. (2015). Coordination and fine motor control depend on Drosophila TRPγ. *Nature Communications* **6**, 7288.

Alexander, R. M. (1989). Optimization and gaits in the locomotion of vertebrates. *Physiological Reviews* **69**, 1199–1227.

Alexander, R. M. (1992). *Exploring biomechanics: animals in motion*. New York: Scientific American Library : Distributed by W.H. Freeman.

Alexander, R. M. (2006). *Principles of animal locomotion*. Princeton: Princeton University Press.

Altman, N. and Krzywinski, M. (2017). P values and the search for significance. *Nat Methods* **14**, 3–4.

Arac, A., Zhao, P., Dobkin, B. H., Carmichael, S. T. and Golshani, P. (2019). DeepBehavior: A Deep Learning Toolbox for Automated Analysis of Animal and Human Behavior Imaging Data. *Front. Syst. Neurosci.* **13**, 20.

Aristidou, A., Lasenby, J., Chrysanthou, Y. and Shamir, A. (2018). Inverse Kinematics Techniques in Computer Graphics: A Survey. *Computer Graphics Forum* **37**, 35–58.

Arroyave-Tobon, S., Drapin, J., Kaniewski, A., Linares, J.-M. and Moretto, P. (2022). Kinematic Modeling at the Ant Scale: Propagation of Model Parameter Uncertainties. *Front. Bioeng. Biotechnol.* **10**, 767914.

Austin, P. C. and Hux, J. E. (2002). A brief note on overlapping confidence intervals. *Journal of Vascular Surgery* **36**, 194–195.

Ayali, A., Borgmann, A., Büschges, A., Couzin-Fuchs, E., Daun-Gruhn, S. and Holmes, P. (2015). The comparative investigation of the stick insect and cockroach models in the study of insect locomotion. *Current Opinion in Insect Science* **12**, 1–10.

Azevedo, A. W., Dickinson, E. S., Gurung, P., Venkatasubramanian, L., Mann, R. S. and Tuthill, J. C. (2020). A size principle for recruitment of Drosophila leg motor neurons. *eLife* **9**, e56754.

Backhaus, B. S. E., Sulkowski, E. and Schlote, F. W. (1984). A semi-synthetic, general-purpose medium for Drosophila melanogaster. *Drosophila Information Service* **60**, 210–212.

Balasubramaniam, R. and Feldman, A. G. (2004). Guiding Movements without Redundancy Problems. In *Coordination Dynamics: Issues and Trends* (ed. Jirsa, V. K.) and Kelso, J. A. S.), pp. 155–176. Berlin, Heidelberg: Springer.

Barroso, F. O., Torricelli, D., Moreno, J. C., Taylor, J., Gomez-Soriano, J., Bravo-Esteban, E., Piazza, S., Santos, C. and Pons, J. L. (2014). Shared muscle synergies in human walking and cycling. *Journal of Neurophysiology* **112**, 1984–1998.

Begon, M., Andersen, M. S. and Dumas, R. (2018). Multibody Kinematics Optimization for the Estimation of Upper and Lower Limb Human Joint Kinematics: A Systematized Methodological Review. *J Biomech Eng* **140**,.

Bellen, H. J., Tong, C. and Tsuda, H. (2010). 100 years of Drosophila research and its impact on vertebrate neuroscience: a history lesson for the future. *Nature Reviews Neuroscience* **11**, 514–522.

Bender, J. A., Simpson, E. M. and Ritzmann, R. E. (2010). Computer-Assisted 3D Kinematic Analysis of All Leg Joints in Walking Insects. *PLOS ONE* **5**, e13617.

Berendes, V. (2016). Speed-dependent interaction of sensory signals and local, pattern-generating activity during walking in Drosophila.

Bernstein, N. A. (1967). *The coordination and regulation of movements*. Oxford: Pergamon Press Ltd.

Bernstein, N. A. and Latash, M. L. (2021). *Bernstein's construction of movements: the original text and commentaries*. New York, NY: Routledge.

Bidaye, S. S., Machacek, C., Wu, Y. and Dickson, B. J. (2014). Neuronal Control of Drosophila Walking Direction. *Science* **344**, 97–101.

Bidaye, S. S., Bockemühl, T. and Büschges, A. (2018). Six-legged walking in insects: how CPGs, peripheral feedback, and descending signals generate coordinated and adaptive motor rhythms. *Journal of Neurophysiology* **119**, 459–475.

Bidaye, S. S., Laturney, M., Chang, A. K., Liu, Y., Bockemühl, T., Büschges, A. and Scott, K. (2020). Two Brain Pathways Initiate Distinct Forward Walking Programs in Drosophila. *Neuron* **108**, 469-485.e8.

Biewener, A. A. and Patek, S. N. (2018). Movement on Land. In *Animal Locomotion*, p. Oxford: Oxford University Press.

Bizzi, E., Mussa-Ivaldi, F. A. and Giszter, S. (1991). Computations underlying the execution of movement: a biological perspective. *Science* **253**, 287–291.

Blanke, A., Watson, P. J., Holbrey, R. and Fagan, M. J. (2017). Computational biomechanics changes our view on insect head evolution. *Proceedings of the Royal Society B: Biological Sciences* **284**, 20162412.

Bockemühl, T. (2017). Prehensile Movements. In *Neurobiology of Motor Control*, pp. 341–364. John Wiley & Sons, Ltd.

Bockemühl, T., Troje, N. F. and Dürr, V. (2010). Inter-joint coupling and joint angle synergies of human catching movements. *Human Movement Science* **29**, 73–93.

Borgmann, A., Hooper, S. L. and Büschges, A. (2009). Sensory Feedback Induced by Front-Leg Stepping Entrains the Activity of Central Pattern Generators in Caudal Segments of the Stick Insect Walking System. *J. Neurosci.* **29**, 2972–2983.

Borgmann, A., Toth, T. I., Gruhn, M., Daun-Gruhn, S. and Büschges, A. (2011). Dominance of local sensory signals over inter-segmental effects in a motor system: experiments. *Biological Cybernetics* **105**, 399–411.

Bradski, G. (2000). The OpenCV Library. *Dr. Dobb's Journal of Software Tools*.

Bradski, G. R. and Kaehler, A. (2008). *Learning OpenCV: computer vision with the OpenCV library*. 1. ed. Beijing: O'Reilly.

Branch, M. A., Coleman, T. F. and Li, Y. (1999). A Subspace, Interior, and Conjugate Gradient Method for Large-Scale Bound-Constrained Minimization Problems. *SIAM J. Sci. Comput.* **21**, 1–23.

Brown, D. (1971). Close-Range Camera Calibration. In *Photogramm Engg.*, pp. 855–866.

Bruton, M. and O'Dwyer, N. (2018). Synergies in coordination: a comprehensive overview of neural, computational, and behavioral approaches. *J Neurophysiol* **120**, 2761–2774.

Burns, M. D. (1973). The Control of Walking in Orthoptera. *Journal of Experimental Biology* **58**, 45–58.

Burrows, M. and Pflüger, H. J. (1988). Positive feedback loops from proprioceptors involved in leg movements of the locust. *J. Comp. Physiol.* **163**, 425–440.

Büschges, A. (1994). The physiology of sensory cells in the ventral scoloparium of the stick insect femoral chordotonal organ. *J. Exp. Biol.* **189**, 285–292.

Büschges, A. (2005). Sensory Control and Organization of Neural Networks Mediating Coordination of Multisegmental Organs for Locomotion. *Journal of Neurophysiology* **93**, 1127–1135.

Büschges, A., Schmitz, J. and Bässler, U. (1995). Rhythmic patterns in the thoracic nerve cord of the stick insect induced by pilocarpine. *J. Exp. Biol.* **198**, 435–456.

Büschges, A., Akay, T., Gabriel, J. P. and Schmidt, J. (2008). Organizing network action for locomotion: Insights from studying insect walking. *Brain Research Reviews* **57**, 162–171.

Camomilla, V., Dumas, R. and Cappozzo, A. (2017). Human movement analysis: The soft tissue artefact issue. *Journal of Biomechanics* **62**, 1–4.

Carreira, V. P., Mensch, J. and Fanara, J. J. (2009). Body size in Drosophila: genetic architecture, allometries and sexual dimorphism. *Heredity* **102**, 246–256.

Castillo-Escario, Y., Rodríguez-Cañón, M., García-Alías, G. and Jané, R. (2020). Identifying Muscle Synergies From Reaching and Grasping Movements in Rats. *IEEE Access* **8**, 62517–62530.

Catavitello, G., Ivanenko, Y. and Lacquaniti, F. (2018). A kinematic synergy for terrestrial locomotion shared by mammals and birds. *eLife* **7**, e38190.

Ceseracciu, E., Sawacha, Z. and Cobelli, C. (2014). Comparison of Markerless and Marker-Based Motion Capture Technologies through Simultaneous Data Collection during Gait: Proof of Concept. *PLoS ONE* **9**, e87640.

Chang, K. R., Tsao, D. D., Bennett, C., Wang, E., Floyd, J. F., Tay, A. S. Y., Greenwald, E., Kim, E. S., Griffin, C., Morse, E., et al. (2022). Transgenic *Drosophila* lines for LexA-dependent gene and growth regulation. *G3 Genes|Genomes|Genetics* **12**, jkac018.

Chen, C.-L., Hermans, L., Viswanathan, M. C., Fortun, D., Aymanns, F., Unser, M., Cammarato, A., Dickinson, M. H. and Ramdya, P. (2018). Imaging neural activity in the ventral nerve cord of behaving adult Drosophila. *Nat Commun* **9**, 4390.

Cheze, L. (2014). *Kinematic analysis of human movement*. Hoboken, NJ: Wiley-ISTE.

Chiappe, M. E. and Jayaraman, V. (2012). Performing Electrophysiology and Two-Photon Calcium Imaging in the Adult Drosophila Central Brain During Walking Behavior. In *Genetically Encoded Functional Indicators* (ed. Martin, J.-R.), pp. 83–101. Totowa, NJ: Humana Press.

Chockley, A. S., Dinges, G. F., Di Cristina, G., Ratican, S., Bockemühl, T. and Büschges, A. (2022). Subsets of leg proprioceptors influence leg kinematics but not interleg coordination in *Drosophila melanogaster* walking. *Journal of Experimental Biology* **225**, jeb244245.

Colyer, S. L., Evans, M., Cosker, D. P. and Salo, A. I. T. (2018). A Review of the Evolution of Vision-Based Motion Analysis and the Integration of Advanced Computer Vision Methods Towards Developing a Markerless System. *Sports Medicine - Open* **4**, 24.

Craig, J. J. (2005). *Introduction to robotics: mechanics and control*. 3rd ed. Upper Saddle River, N.J: Pearson/Prentice Hall.

Crawford, N. R., Yamaguchi, G. T. and Dickman, C. A. (1996). Methods for determining spinal flexion/extension, lateral bending, and axial rotation from marker coordinate data: Analysis and refinement. *Human Movement Science* **15**, 55–78.

Crawford, N. R., Yamaguchi, G. T. and Dickman, C. A. (1999). A new technique for determining 3-D joint angles: the tilt/twist method. *Clinical Biomechanics* **14**, 153–165.

Cronin, N. J. (2021). Using deep neural networks for kinematic analysis: Challenges and opportunities. *Journal of Biomechanics* **123**, 110460.

Cruse, H. and Bartling, Ch. (1995). Movement of joint angles in the legs of a walking insect, Carausius morosus. *Journal of Insect Physiology* **41**, 761–771.

Cruse, H., Dürr, V., Schilling, M. and Schmitz, J. (2009). Principles of Insect Locomotion. In *Spatial Temporal Patterns for Action-Oriented Perception in Roving Robots* (ed. Arena, P.) and Patanè, L.), pp. 43–96. Berlin, Heidelberg: Springer Berlin Heidelberg.

Cumming, G. and Finch, S. (2005). Inference by Eye: Confidence Intervals and How to Read Pictures of Data. *American Psychologist* **60**, 170–180.

Cunningham, P., Cord, M. and Delany, S. J. (2008). Supervised learning. In *Machine learning techniques for multimedia*, pp. 21–49. Springer.

d'Avella, A. and Bizzi, E. (2005). Shared and specific muscle synergies in natural motor behaviors. *PNAS* **102**, 3076–3081.

d'Avella, A., Saltiel, P. and Bizzi, E. (2003). Combinations of muscle synergies in the construction of a natural motor behavior. *Nature Neuroscience* **6**, 300–308.

Daffertshofer, A., Lamoth, C. J. C., Meijer, O. G. and Beek, P. J. (2004). PCA in studying coordination and variability: a tutorial. *Clinical Biomechanics* **19**, 415–428.

Dallmann, C. J., Dürr, V. and Schmitz, J. (2016). Joint torques in a freely walking insect reveal distinct functions of leg joints in propulsion and posture control. *Proc Biol Sci* **283**, 20151708.

David, I., Holmes, P. and Ayali, A. (2016). Endogenous rhythm and pattern-generating circuit interactions in cockroach motor centres. *Biology Open* **5**, 1229–1240.

DeAngelis, B. D., Zavatone-Veth, J. A. and Clark, D. A. (2019). The manifold structure of limb coordination in walking Drosophila. *eLife* **8**, e46409.

Delcomyn, F. (1971). The Locomotion of the Cockroach Periplaneta Americana. *J. Exp. Biol.* **54**, 443–452.

Denavit, J. and Hartenberg, R. S. (1955). A kinematic notation for lower-pair mechanisms based on matrices. *Trans.\ ASME E, Journal of Applied Mechanics* **22**, 215–221.

Desai, B. S., Chadha, A. and Cook, B. (2014). The stum Gene Is Essential for Mechanical Sensing in Proprioceptive Neurons. *Science* **343**, 1256–1259.

Dickinson, M. H., Farley, C. T., Full, R. J., Koehl, M. a. R., Kram, R. and Lehman, S. (2000). How Animals Move: An Integrative View. *Science* **288**, 100–106.

Diedrichsen, J., Shadmehr, R. and Ivry, R. B. (2010). The coordination of movement: optimal feedback control and beyond. *Trends in Cognitive Sciences* **14**, 31–39.

Dinges, G. F., Chockley, A. S., Bockemühl, T., Ito, K., Blanke, A. and Büschges, A. (2021). Location and arrangement of campaniform sensilla in Drosophila melanogaster. *Journal of Comparative Neurology* **529**, 905–925.

Duffy, J. B. (2002). GAL4 system in drosophila: A fly geneticist's swiss army knife. *genesis* **34**, 1–15.

Dunn, T. W., Marshall, J. D., Severson, K. S., Aldarondo, D. E., Hildebrand, D. G. C., Chettih, S. N., Wang, W. L., Gellis, A. J., Carlson, D. E., Aronov, D., et al. (2021). Geometric deep learning enables 3D kinematic profiling across species and environments. *Nat Methods* **18**, 564–573.

Dürr, V. and Ebeling, W. (2005). The behavioural transition from straight to curve walking: kinetics of leg movement parameters and the initiation of turning. *J. Exp. Biol.* **208**, 2237–2252.

Duysens, J., Clarac, F. and Cruse, H. (2000). Load-Regulating Mechanisms in Gait and Posture: Comparative Aspects. *Physiological Reviews* **80**, 83–133.

Emmert-Streib, F., Yang, Z., Feng, H., Tripathi, S. and Dehmer, M. (2020). An Introductory Review of Deep Learning for Prediction Models With Big Data. *Front. Artif. Intell.* **3**, 4.

Enriquez, J., Venkatasubramanian, L., Baek, M., Peterson, M., Aghayeva, U. and Mann, R. S. (2015). Specification of Individual Adult Motor Neuron Morphologies by Combinatorial Transcription Factor Codes. *Neuron* **86**, 955–970.

Federolf, P. A. (2016). A novel approach to study human posture control: "Principal movements" obtained from a principal component analysis of kinematic marker data. *Journal of Biomechanics* **49**, 364–370.

Federolf, P., Tecante, K. and Nigg, B. (2012). A holistic approach to study the temporal variability in gait. *Journal of Biomechanics* **45**, 1127–1132.

Feng, K., Sen, R., Minegishi, R., Dübbert, M., Bockemühl, T., Büschges, A. and Dickson, B. J. (2020). Distributed control of motor circuits for backward walking in Drosophila. *Nat Commun* **11**, 6166.

Field, L. H. and Matheson, T. (1998). Chordotonal Organs of Insects. In *Advances in Insect Physiology* (ed. Evans, P. D.), pp. 1–228. Cambridge, MA, USA: Academic Press.

Frantsevich, L. and Wang, W. (2009). Gimbals in the insect leg. *Arthropod Structure & Development* **38**, 16–30.

Frazier, S. F., Larsen, G. S., Neff, D., Quimby, L., Carney, M., DiCaprio, R. A. and Zill, S. N. (1999). Elasticity and movements of the cockroach tarsus in walking. *J Comp Physiol A* **185**, 157–172.

Fuchs, E., Holmes, P., Kiemel, T. and Ayali, A. (2011). Intersegmental Coordination of Cockroach Locomotion: Adaptive Control of Centrally Coupled Pattern Generator Circuits. *Frontiers in Neural Circuits* **4**, 125.

Full, R. and Ahn, A. (1995). Static forces and moments generated in the insect leg: comparison of a three-dimensional musculo-skeletal computer model with experimental measurements. *Journal of Experimental Biology* **198**, 1285–1298.

Full, R. J. and Koditschek, D. E. (1999). Templates and anchors: neuromechanical hypotheses of legged locomotion on land. *Journal of Experimental Biology* **202**, 3325–3332.

Full, R. J. and Tu, M. S. (1991). Mechanics of a rapid running insect: two-, four- and six-legged locomotion. *Journal of Experimental Biology* **156**, 215–231.

Gebehart, C. and Büschges, A. (2021). Temporal differences between load and movement signal integration in the sensorimotor network of an insect leg. *Journal of Neurophysiology* **126**, 1875–1890.

Giszter, S. F., Mussa-Ivaldi, F. A. and Bizzi, E. (1993). Convergent force fields organized in the frog's spinal cord. *J Neurosci* **13**, 467–491.

Goldsmith, C. A., Haustein, M., Bockemühl, T., Büschges, A. and Szczecinski, N. S. (2022). Analyzing 3D Limb Kinematics of Drosophila Melanogaster for Robotic Platform Development. In *Biomimetic and Biohybrid Systems* (ed. Hunt, A.), Vouloutsi, V.), Moses, K.), Quinn, R.), Mura, A.), Prescott, T.), and Verschure, P. F. M. J.), pp. 111–122. Cham: Springer International Publishing.

Goodman, S. (2008). A Dirty Dozen: Twelve P-Value Misconceptions. *Seminars in Hematology* **45**, 135–140.

Graham, D. (1972). A behavioural analysis of the temporal organisation of walking movements in the 1st instar and adult stick insect (Carausius morosus). *Journal of comparative physiology* **81**, 23–52.

Graham, D. (1985). Pattern and Control of Walking in Insects. In *Advances in Insect Physiology* (ed. Berridge, M. J.), Treherne, J. E.), and Wigglesworth, V. B.), pp. 31–140. Academic Press.

Graving, J. M., Chae, D., Naik, H., Li, L., Koger, B., Costelloe, B. R. and Couzin, I. D. (2019). DeepPoseKit, a software toolkit for fast and robust animal pose estimation using deep learning. *eLife* **8**, e47994.

Greenfield, M. L. V. H., Kuhn, J. E. and Wojtys, E. M. (1998). A Statistics Primer. *Am J Sports Med* **26**, 145–149.

Grillner, S. (2006). Biological Pattern Generation: The Cellular and Computational Logic of Networks in Motion. *Neuron* **52**, 751–766.

Grillner, S. and El Manira, A. (2020). Current Principles of Motor Control, with Special Reference to Vertebrate Locomotion. *Physiological Reviews* **100**, 271–320.

Grillner, S. and Kozlov, A. (2021). The CPGs for Limbed Locomotion–Facts and Fiction. *IJMS* **22**, 5882.

Gruhn, M., Zehl, L. and Büschges, A. (2009). Straight walking and turning on a slippery surface. *J. Exp. Biol.* **212**, 194–209.

Gruhn, M., Rosenbaum, P., Bockemühl, T. and Büschges, A. (2016). Body side-specific control of motor activity during turning in a walking animal. *eLife* **5**, e13799.

Günel, S., Rhodin, H., Morales, D., Compagnolo, J., Ramdya, P. and Fua, P. (2019). DeepFly3D: A deep learning-based approach for 3D limb and appendage tracking in tethered, adult Drosophila. *bioRxiv* 640375.

Guo, S., Lin, J., Wöhrl, T. and Liao, M. (2018). A Neuro-Musculo-Skeletal Model for Insects With Data-driven Optimization. *Scientific Reports* **8**, 2129.

Guthrie, D. M. (1967). Multipolar stretch receptors and the insect leg reflex. *Journal of Insect Physiology* **13**, 1637–1644.

Haid, T. H., Doix, A.-C. M., Nigg, B. M. and Federolf, P. A. (2018). Age Effects in Postural Control Analyzed via a Principal Component Analysis of Kinematic Data and Interpreted in Relation to Predictions of the Optimal Feedback Control Theory. *Front. Aging Neurosci.* **10**, 22.

Hales, K. G., Korey, C. A., Larracuente, A. M. and Roberts, D. M. (2015). Genetics on the Fly: A Primer on the Drosophila Model System. *Genetics* **201**, 815–842.

Halliday, D. M., Conway, B. A., Christensen, L. O. D., Hansen, N. L., Petersen, N. P. and Nielsen, J. B. (2003). Functional Coupling of Motor Units Is Modulated During Walking in Human Subjects. *Journal of Neurophysiology* **89**, 960–968.

Harris, C. R., Millman, K. J., van der Walt, S. J., Gommers, R., Virtanen, P., Cournapeau, D., Wieser, E., Taylor, J., Berg, S., Smith, N. J., et al. (2020). Array programming with NumPy. *Nature* **585**, 357–362.

Harris-Warrick, R. M. and Ramirez, J.-M. (2017). Neural Networks for the Generation of Rhythmic Motor Behaviors. In *Neurobiology of Motor Control* (ed. Hooper, S. L.) and Büschges, A.), pp. 225–262. Hoboken, NJ, USA: John Wiley & Sons, Inc.

Hart, C. B. and Giszter, S. F. (2004). Modular premotor drives and unit bursts as primitives for frog motor behaviors. *J Neurosci* **24**, 5269–5282.

Hartley, R. and Zisserman, A. (2004). *Multiple View Geometry in Computer Vision*. 2nd ed. Cambridge: Cambridge University Press.

Hastie, T., Tibshirani, R. and Friedman, J. (2009). Unsupervised Learning. In *The Elements of Statistical Learning: Data Mining, Inference, and Prediction* (ed. Hastie, T.), Tibshirani, R.), and Friedman, J.), pp. 485–585. New York, NY: Springer New York.

Hays, W. L. (1973). *Statistics for the social sciences*. 2d ed. New York: Holt, Rinehart and Winston.

He, K., Zhang, X., Ren, S. and Sun, J. (2016). Deep Residual Learning for Image Recognition. In *2016 IEEE Conference on Computer Vision and Pattern Recognition (CVPR)*, pp. 770–778. Las Vegas, NV, USA: IEEE.

Hermans, L., Kaynak, M., Braun, J., Ríos, V. L., Chen, C.-L., Friedberg, A., Günel, S., Aymanns, F., Sakar, M. S. and Ramdya, P. (2022). Microengineered devices enable long-term imaging of the ventral nerve cord in behaving adult Drosophila. *Nat Commun* **13**, 5006.

Hess, D. and Büschges, A. (1999). Role of Proprioceptive Signals From an Insect Femur-Tibia Joint in Patterning Motoneuronal Activity of an Adjacent Leg Joint. *Journal of Neurophysiology* **81**, 1856–1865.

Holmes, P., Full, R., Koditschek, D. and Guckenheimer, J. (2006). The Dynamics of Legged Locomotion: Models, Analyses, and Challenges. *SIAM Rev.* **48**, 207–304.

Holstein, H. and Li, B. (2002). Low Density Feature Point Matching for Articulated Pose Identification. In *Procedings of the British Machine Vision Conference 2002*, p. 66.1-66.10. Cardiff: British Machine Vision Association.

Hooke, A. W., Karol, S., Park, J., Kim, Y. H. and Shim, J. K. (2012). Handwriting: Three-Dimensional Kinetic Synergies in Circle Drawing Movements. *Motor Control* **16**, 329–352.

Huang, B., Xiong, C., Chen, W., Liang, J., Sun, B.-Y. and Gong, X. (2021). Common kinematic synergies of various human locomotor behaviours. *R. Soc. open sci.* **8**, rsos.210161, 210161.

Hubbard, R. and Lindsay, R. M. (2008). Why *P* Values Are Not a Useful Measure of Evidence in Statistical Significance Testing. *Theory & Psychology* **18**, 69–88.

Hubel, D. H. and Wiesel, T. N. (1962). Receptive fields, binocular interaction and functional architecture in the cat's visual cortex. *The Journal of physiology* **160**, 106.

Hughes, G. M. (1952). The Co-Ordination of Insect Movements. *J. Exp. Biol.* **29**, 267–285.

Hunter, J. D. (2007). Matplotlib: A 2D Graphics Environment. *Comput. Sci. Eng.* **9**, 90–95.

Ijspeert, A. J. (2002). Vertebrate locomotion. In *The Handbook of Brain Theory and Neural Networks* (ed. Arbib, M. A.), pp. 649–653. Cambridge, MA, USA: The MIT Press.

Insafutdinov, E., Pishchulin, L., Andres, B., Andriluka, M. and Schiele, B. (2016). DeeperCut: A Deeper, Stronger, and Faster Multi-Person Pose Estimation Model.

Ito, K., Shinomiya, K., Ito, M., Armstrong, J. D., Boyan, G., Hartenstein, V., Harzsch, S., Heisenberg, M., Homberg, U., Jenett, A., et al. (2014). A Systematic Nomenclature for the Insect Brain. *Neuron* **81**, 755–765.

Ivanenko, Y. P., Poppele, R. E. and Lacquaniti, F. (2004). Five basic muscle activation patterns account for muscle activity during human locomotion. *The Journal of Physiology* **556**, 267–282.

Jain, A. K., Jianchang Mao and Mohiuddin, K. M. (1996). Artificial neural networks: a tutorial. *Computer* **29**, 31–44.

Jiang, L., Lee, C., Teotia, D. and Ostadabbas, S. (2022). Animal pose estimation: A closer look at the state-of-the-art, existing gaps and opportunities. *Computer Vision and Image Understanding* **222**, 103483.

Jiménez Bascones, J. L., Graña, M. and Lopez-Guede, J. M. (2019). Robust labeling of human motion markers in the presence of occlusions. *Neurocomputing* **353**, 96–105.

Jin, P., Griffith, L. C. and Murphey, R. K. (1998). Presynaptic Calcium/Calmodulin-Dependent Protein Kinase II Regulates Habituation of a Simple Reflex in Adult *Drosophila*. *J. Neurosci.* **18**, 8955–8964.

Jindrich, D. L. and Full, R. J. (1999). Many-legged maneuverability: dynamics of turning in hexapods. *Journal of Experimental Biology* **202**, 1603–1623.

Johnston, R. M. and Levine, R. B. (2002). Thoracic leg motoneurons in the isolated CNS of adult Manduca produce patterned activity in response to pilocarpine, which is distinct from that produced in larvae. *Invertebrate Neuroscience* **4**, 175–192.

Jolliffe, I. T. and Cadima, J. (2016). Principal component analysis: a review and recent developments. *Philosophical Transactions of the Royal Society A: Mathematical, Physical and Engineering Sciences* **374**, 20150202.

Kain, J., Stokes, C., Gaudry, Q., Song, X., Foley, J., Wilson, R. and de Bivort, B. (2013). Leg-tracking and automated behavioural classification in Drosophila. *Nat Commun* **4**, 1910.

Karashchuk, P., Rupp, K. L., Dickinson, E. S., Walling-Bell, S., Sanders, E., Azim, E., Brunton, B. W. and Tuthill, J. C. (2021). Anipose: A toolkit for robust markerless 3D pose estimation. *Cell Reports* **36**, 109730.

Kazama, H. (2015). Systems neuroscience in Drosophila: Conceptual and technical advantages. *Neuroscience* **296**, 3–14.

Kipp, K., Redden, J., Sabick, M. and Harris, C. (2012). Kinematic and Kinetic Synergies of the Lower Extremities During the Pull in Olympic Weightlifting. *Journal of Applied Biomechanics* **28**, 271–278.

Klapoetke, N. C., Murata, Y., Kim, S. S., Pulver, S. R., Birdsey-Benson, A., Cho, Y. K., Morimoto, T. K., Chuong, A. S., Carpenter, E. J., Tian, Z., et al. (2014). Independent optical excitation of distinct neural populations. *Nature Methods* **11**, 338–346.

Krakauer, J. W., Ghazanfar, A. A., Gomez-Marin, A., MacIver, M. A. and Poeppel, D. (2017). Neuroscience Needs Behavior: Correcting a Reductionist Bias. *Neuron* **93**, 480–490.

Kram, R., Wong, B. and Full, R. J. (1997). Three-dimensional kinematics and limb kinetic energy of running cockroaches. *Journal of Experimental Biology* **200**, 1919–1929.

Krause, A. F. and Dürr, V. (2004). Tactile efficiency of insect antennae with two hinge joints. *Biol. Cybern.* **91**, 168–181.

Krishnamoorthy, V., Goodman, S., Zatsiorsky, V. and Latash, M. L. (2003). Muscle synergies during shifts of the center of pressure by standing persons: identification of muscle modes. *Biological Cybernetics* **89**, 152–161.

Krizhevsky, A., Sutskever, I. and Hinton, G. E. (2012). ImageNet Classification with Deep Convolutional Neural Networks. In *Advances in Neural Information Processing Systems* (ed. Pereira, F.), Burges, C. J.), Bottou, L.), and Weinberger, K. Q.), p. Curran Associates, Inc.

Lambert-Shirzad, N. and Van der Loos, H. F. M. (2016). On identifying kinematic and muscle synergies: a comparison of matrix factorization methods using experimental data from the healthy population. *Journal of Neurophysiology* **117**, 290–302.

Latash, M. L. (2010). Motor synergies and the equilibrium-point hypothesis. *Motor Control* **14**, 294–322.

LeCun, Y., Bengio, Y. and Hinton, G. (2015). Deep learning. *Nature* **521**, 436–444.

Lehmann, F.-O., Skandalis, D. A. and Berthé, R. (2013). Calcium signalling indicates bilateral power balancing in the *Drosophila* flight muscle during manoeuvring flight. *J. R. Soc. Interface.* **10**, 20121050.

Leon, S. J., Björck, Å. and Gander, W. (2013). Gram-Schmidt orthogonalization: 100 years and more: GRAM-SCHMIDT ORTHOGONALIZATION: 100 YEARS AND MORE. *Numer. Linear Algebra Appl.* **20**, 492–532.

Lindsay, G. W. (2021). Convolutional Neural Networks as a Model of the Visual System: Past, Present, and Future. *Journal of Cognitive Neuroscience* **33**, 2017–2031.

Lindsay, T., Sustar, A. and Dickinson, M. (2017). The Function and Organization of the Motor System Controlling Flight Maneuvers in Flies. *Current Biology* **27**, 345–358.

Lobato-Rios, V., Ramalingasetty, S. T., Özdil, P. G., Arreguit, J., Ijspeert, A. J. and Ramdya, P. (2022). NeuroMechFly, a neuromechanical model of adult Drosophila melanogaster. *Nat Methods* **19**, 620–627.

Long, L. and Dongri, S. (2019). Review of Camera Calibration Algorithms. In *Advances in Computer Communication and Computational Sciences* (ed. Bhatia, S. K.), Tiwari, S.), Mishra, K. K.), and Trivedi, M. C.), pp. 723–732. Singapore: Springer Singapore.

Lu, T.-W. and O'Connor, J. J. (1999). Bone position estimation from skin marker co-ordinates using global optimisation with joint constraints. *Journal of Biomechanics* **32**, 129–134.

Ludwar, B. Ch., Göritz, M. L. and Schmidt, J. (2005). Intersegmental Coordination of Walking Movements in Stick Insects. *Journal of Neurophysiology* **93**, 1255–1265.

Lynch, K. M. and Park, F. C. (2017). Denavit-Hartenberg Parameters. In *Modern Robotics: Mechanics Planning and Control*, pp. 585–596. Cambridge, United Kingdom: Cambridge University Press.

Ma, Y. and Zhu, L. (2013). A Review on Dimension Reduction: *A Review on Dimension Reduction*. *International Statistical Review* **81**, 134–150.

MacKay-Lyons, M. (2002). Central Pattern Generation of Locomotion: A Review of the Evidence. *Physical Therapy* **82**, 69–83.

Majed, L., Heugas, A. M. and Siegler, I. A. (2017). Changes in movement organization and control strategies when learning a biomechanically constrained gait pattern, racewalking: a PCA study. *Exp Brain Res* **235**, 931–940.

Mamiya, A., Gurung, P. and Tuthill, J. C. (2018). Neural Coding of Leg Proprioception in Drosophila. *Neuron* **100**, 636-650.e6.

Manoonpong, P., Patanè, L., Xiong, X., Brodoline, I., Dupeyroux, J., Viollet, S., Arena, P. and Serres, J. R. (2021). Insect-Inspired Robots: Bridging Biological and Artificial Systems. *Sensors* **21**, 7609.

Mantziaris, C., Bockemühl, T., Holmes, P., Borgmann, A., Daun, S. and Büschges, A. (2017). Intra- and intersegmental influences among central pattern generating networks in the walking system of the stick insect. *Journal of Neurophysiology* **118**, 2296–2310.

Mantziaris, C., Bockemühl, T. and Büschges, A. (2020). Central pattern generating networks in insect locomotion. *Develop Neurobiol* **80**, 16–30.

Marom, S. (2009). On the Precarious Path of Reverse Neuro-Engineering. *Front. Comput. Neurosci.* **3**,.

Martin, J.-R. (2004). A portrait of locomotor behaviour in Drosophila determined by a video-tracking paradigm. *Behavioural Processes* **67**, 207–219.

Matheson, T. (1990). Responses and locations of neurones in the locust metathoracic femoral chordotonal organ. *J Comp Physiol A* **166**,.

Mathis, A., Mamidanna, P., Cury, K. M., Abe, T., Murthy, V. N., Mathis, M. W. and Bethge, M. (2018). DeepLabCut: markerless pose estimation of user-defined body parts with deep learning. *Nat Neurosci* **21**, 1281–1289.

Mathis, A., Schneider, S., Lauer, J. and Mathis, M. W. (2020). A Primer on Motion Capture with Deep Learning: Principles, Pitfalls, and Perspectives. *Neuron* **108**, 44–65.

McKinney, W. (2010). Data Structures for Statistical Computing in Python.pp. 56–61. Austin, Texas.

McMorland, A. J. C., Runnalls, K. D. and Byblow, W. D. (2015). A Neuroanatomical Framework for Upper Limb Synergies after Stroke. *Front. Hum. Neurosci.* **9**,.

Mendes, C. S., Bartos, I., Akay, T., Márka, S. and Mann, R. S. (2013). Quantification of gait parameters in freely walking wild type and sensory deprived Drosophila melanogaster. *eLife* **2**, e00231.

Mendes, C. S., Rajendren, S. V., Bartos, I., Márka, S. and Mann, R. S. (2014). Kinematic Responses to Changes in Walking Orientation and Gravitational Load in Drosophila melanogaster. *PLOS ONE* **9**, e109204.

Mündermann, L., Corazza, S. and Andriacchi, T. P. (2006). The evolution of methods for the capture of human movement leading to markerless motion capture for biomechanical applications. *J NeuroEngineering Rehabil* **3**, 6.

Mussa-Ivaldi, F. A. and Bizzi, E. (2000). Motor Learning through the Combination of Primitives. *Philosophical Transactions: Biological Sciences* **355**, 1755–1769.

Nakagawa, S. and Cuthill, I. C. (2007). Effect size, confidence interval and statistical significance: a practical guide for biologists. *Biological Reviews* **82**, 591–605.

Nath, T., Mathis, A., Chen, A. C., Patel, A., Bethge, M. and Mathis, M. W. (2019). Using DeepLabCut for 3D markerless pose estimation across species and behaviors. *Nat Protoc* **14**, 2152–2176.

Nazifi, M. M., Yoon, H. U., Beschorner, K. and Hur, P. (2017). Shared and Task-Specific Muscle Synergies during Normal Walking and Slipping. *Front. Hum. Neurosci.* **11**,.

Newell, A., Yang, K. and Deng, J. (2016). Stacked Hourglass Networks for Human Pose Estimation.

Nielsen, J. B. (2003). How we Walk: Central Control of Muscle Activity during Human Walking. *Neuroscientist* **9**, 195–204.

Nishikawa, K., Biewener, A. A., Aerts, P., Ahn, A. N., Chiel, H. J., Daley, M. A., Daniel, T. L., Full, R. J., Hale, M. E., Hedrick, T. L., et al. (2007). Neuromechanics: an integrative approach for understanding motor control. *Integrative and Comparative Biology* **47**, 16–54.

Overduin, S. A., d'Avella, A., Roh, J. and Bizzi, E. (2008). Modulation of Muscle Synergy Recruitment in Primate Grasping. *Journal of Neuroscience* **28**, 880–892.

Overduin, S. A., d'Avella, A., Carmena, J. M. and Bizzi, E. (2012). Microstimulation activates a handful of muscle synergies. *Neuron* **76**, 1071–1077.

Pearson, K. G. (1993). Common Principles of Motor Control in Vertebrates and Invertebrates. *Annual Review of Neuroscience* **16**, 265–297.

Pearson, K. G., Wong, R. K. and Fourtner, C. R. (1976). Connexions between hair-plate afferents and motoneurones in the cockroach leg. *Journal of Experimental Biology* **64**, 251–266.

Pedregosa, F., Varoquaux, G., Gramfort, A., Michel, V., Thirion, B., Grisel, O., Blondel, M., Prettenhofer, P., Weiss, R., Dubourg, V., et al. (2011). Scikit-learn: Machine Learning in Python. *Journal of Machine Learning Research* **12**, 2825–2830.

Pereira, T. D., Tabris, N., Li, J., Ravindranath, S., Papadoyannis, E. S., Wang, Z. Y., Turner, D. M., McKenzie-Smith, G., Kocher, S. D., Falkner, A. L., et al. (2020). *SLEAP: Multi-animal pose tracking*. Animal Behavior and Cognition.

Peres-Neto, P. R., Jackson, D. A. and Somers, K. M. (2005). How many principal components? stopping rules for determining the number of non-trivial axes revisited. *Computational Statistics & Data Analysis* **49**, 974–997.

Petrou, G. and Webb, B. (2012). Detailed tracking of body and leg movements of a freely walking female cricket during phonotaxis. *Journal of Neuroscience Methods* **203**, 56–68.

Phelps, J. S., Hildebrand, D. G. C., Graham, B. J., Kuan, A. T., Thomas, L. A., Nguyen, T. M., Buhmann, J., Azevedo, A. W., Sustar, A., Agrawal, S., et al. (2021). Reconstruction of motor control circuits in adult Drosophila using automated transmission electron microscopy. *Cell* **184**, 759-774.e18.

Pringle, J. W. S. (1938). Proprioception In Insects. *Journal of Experimental Biology* **15**, 467–473.

Radnikov, G. and Bässler, U. (1991). Function of a Muscle Whose Apodeme Travels Through a Joint Moved by Other Muscles: Why the Retractor Unguis Muscle in Stick Insects is Tripartite and has no Antagonist. *Journal of Experimental Biology* **157**, 87–99.

Rearick, M. P., Casares, A. and Santello, M. (2003). Task-Dependent Modulation of Multi-Digit Force Coordination Patterns. *Journal of Neurophysiology* **89**, 1317–1326.

Rein, K., Zöckler, M., Mader, M. T., Grübel, C. and Heisenberg, M. (2002). The Drosophila Standard Brain. *Current Biology* **12**, 227–231.

Ritzmann, R. E. and Bender, J. A. (2010). Insect Flight and Walking: Neuroethological Basis. In *Encyclopedia of Animal Behavior*, pp. 155–160. Elsevier.

Ritzmann, R. E., Quinn, R. D. and Fischer, M. S. (2004). Convergent evolution and locomotion through complex terrain by insects, vertebrates and robots. *Arthropod Structure & Development* **33**, 361–379.

Robertson, D. G. E., Caldwell, G. E., Hamill, J., Kamen, G. and Whittlesey, S. N. (2014). *Research methods in biomechanics*. Second edition. Champaign, Illinois: Human Kinetics.

Santello, M. and Soechting, J. F. (2000). Force synergies for multifingered grasping. *Experimental Brain Research* **133**, 457–467.

Santuz, A., Akay, T., Mayer, W. P., Wells, T. L., Schroll, A. and Arampatzis, A. (2019). Modular organization of murine locomotor pattern in the presence and absence of sensory feedback from muscle spindles. *The Journal of Physiology* **597**, 3147–3165.

Scheffer, L. K. and Meinertzhagen, I. A. (2019). The Fly Brain Atlas. *Annu. Rev. Cell Dev. Biol.* **35**, 637–653.

Scheffer, L. K., Xu, C. S., Januszewski, M., Lu, Z., Takemura, S., Hayworth, K. J., Huang, G. B., Shinomiya, K., Maitlin-Shepard, J., Berg, S., et al. (2020). A connectome and analysis of the adult Drosophila central brain. *eLife* **9**, e57443.

Schütz, C. and Schack, T. (2013). Motor primitives of pointing movements in a three-dimensional workspace. *Exp Brain Res* **227**, 355–365.

Seelig, J. D., Chiappe, M. E., Lott, G. K., Dutta, A., Osborne, J. E., Reiser, M. B. and Jayaraman, V. (2010). Two-photon calcium imaging from head-fixed Drosophila during optomotor walking behavior. *Nature Methods* **7**, 535–540.

Seipel, J., Kvalheim, M., Revzen, S., A. Sharbafi, M. and Seyfarth, A. (2017). Conceptual Models of Legged Locomotion. In *Bioinspired Legged Locomotion*, pp. 55–131. Elsevier.

Sellers, W. I. and Hirasaki, E. (2014). Markerless 3D motion capture for animal locomotion studies. *Biology Open* **3**, 656–668.

Shorten, C. and Khoshgoftaar, T. M. (2019). A survey on Image Data Augmentation for Deep Learning. *J Big Data* **6**, 60.

Silaghi, M.-Că., Plänkers, R., Boulic, R., Fua, P. and Thalmann, D. (1998). Local and Global Skeleton Fitting Techniques for Optical Motion Capture. In *Modelling and Motion Capture Techniques for*

Virtual Environments (ed. Magnenat-Thalmann, N.) and Thalmann, D.), pp. 26–40. Berlin, Heidelberg: Springer Berlin Heidelberg.

Singh, R. E., Iqbal, K., White, G. and Hutchinson, T. E. (2018). A Systematic Review on Muscle Synergies: From Building Blocks of Motor Behavior to a Neurorehabilitation Tool. *Appl Bionics Biomech* **2018**, 3615368–3615368.

Singh, R., Kukshal, V. and Yadav, V. S. (2021). A Review on Forward and Inverse Kinematics of Classical Serial Manipulators. In *Advances in Engineering Design* (ed. Rakesh, P. K.), Sharma, A. K.), and Singh, I.), pp. 417–428. Singapore: Springer Singapore.

Sink, H. (2006). An Introduction to Muscle Development in Drosophila. In *Muscle Development in Drosophila* (ed. Sink, H.), pp. 1–7. New York, NY: Springer.

Snodgrass, R. E. (1935). *Principles of insect morphology*. 1st ed. New York, USA: McGraw-Hill Publishing Co.

Soler, C., Daczewska, M., Ponte, J. P. D., Dastugue, B. and Jagla, K. (2004). Coordinated development of muscles and tendons of the Drosophila leg. *Development* **131**, 6041–6051.

Spong, M. W., Hutchinson, S. and Vidyasagar, M. (2020a). *Robot modeling and control*. Second edition. Hoboken, NJ: John Wiley & Sons, Inc.

Spong, M. W., Hutchinson, S. and Vidyasagar, M. (2020b). Forward Kinematics: The Denavit-Hartenberg Convention. In *Robot Modeling and Control*, pp. 75–100. Hoboken, NJ: John Wiley & Sons, Ltd.

Steele, K. M., Tresch, M. C. and Perreault, E. J. (2015). Consequences of biomechanically constrained tasks in the design and interpretation of synergy analyses. *Journal of Neurophysiology* **113**, 2102–2113.

Stein, W. and Sauer, A. E. (1999). Physiology of vibration-sensitive afferents in the femoral chordotonal organ of the stick insect. *Journal of Comparative Physiology A* **184**, 253–263.

Stein, W., Büschges, A. and Bässler, U. (2006). Intersegmental transfer of sensory signals in the stick insect leg muscle control system. *Journal of Neurobiology* **66**, 1253–1269.

Stetter, B. J., Herzog, M., Möhler, F., Sell, S. and Stein, T. (2020). Modularity in Motor Control: Similarities in Kinematic Synergies Across Varying Locomotion Tasks. *Front. Sports Act. Living* **2**,.

Strauß, R. and Heisenberg, M. (1990). Coordination of legs during straight walking and turning in Drosophila melanogaster. *Journal of Comparative Physiology A* **167**, 403–412.

Sullivan, G. M. and Feinn, R. (2012). Using Effect Size—or Why the *P* Value Is Not Enough. *Journal of Graduate Medical Education* **4**, 279–282.

Szczecinski, N. S., Brown, A. E., Bender, J. A., Quinn, R. D. and Ritzmann, R. E. (2014). A neuromechanical simulation of insect walking and transition to turning of the cockroach Blaberus discoidalis. *Biol Cybern* **108**, 1–21.

Szczecinski, N. S., Bockemühl, T., Chockley, A. S. and Büschges, A. (2018). Static stability predicts the continuum of interleg coordination patterns in *Drosophila*. *Journal of Experimental Biology* jeb.189142.

Tajiri, R., Misaki, K., Yonemura, S. and Hayashi, S. (2010). Dynamic shape changes of ECM-producing cells drive morphogenesis of ball-and-socket joints in the fly leg. *Development* **137**, 2055–2063.

Tang, S., Chen, L., Barsotti, M., Hu, L., Li, Y., Wu, X., Bai, L., Frisoli, A. and Hou, W. (2019). Kinematic Synergy of Multi-DoF Movement in Upper Limb and Its Application for Rehabilitation Exoskeleton Motion Planning. *Front. Neurorobot.* **13**, 99.

Theunissen, L. M. and Dürr, V. (2013). Insects Use Two Distinct Classes of Steps during Unrestrained Locomotion. *PLOS ONE* **8**, e85321.

Ting, L. H. and McKay, J. L. (2007). Neuromechanics of muscle synergies for posture and movement. *Current Opinion in Neurobiology* **17**, 622–628.

Todorov, E. and Ghahramani, Z. (2004). Analysis of the synergies underlying complex hand manipulation. In *The 26th Annual International Conference of the IEEE Engineering in Medicine and Biology Society*, pp. 4637–4640. San Francisco, CA, USA: IEEE.

Torres-Oviedo, G., Macpherson, J. M. and Ting, L. H. (2006). Muscle Synergy Organization Is Robust Across a Variety of Postural Perturbations. *Journal of Neurophysiology* **96**, 1530–1546.

Tresch, M. C. and Bizzi, E. (1999). Responses to spinal microstimulation in the chronically spinalized rat and their relationship to spinal systems activated by low threshold cutaneous stimulation. *Exp Brain Res* **129**, 401–416.

Tresch, M. C. and Jarc, A. (2009). The case for and against muscle synergies. *Current Opinion in Neurobiology* **19**, 601–607.

Tresch, M. C., Saltiel, P. and Bizzi, E. (1999). The construction of movement by the spinal cord. *Nature Neuroscience* **2**, 162–167.

Troje, N. F. (2002). Decomposing biological motion: A framework for analysis and synthesis of human gait patterns. *Journal of Vision* **2**, 2–2.

Tryba, A. K. and Ritzmann, R. E. (2000). Multi-Joint Coordination During Walking and Foothold Searching in the *Blaberus* Cockroach. I. Kinematics and Electromyograms. *Journal of Neurophysiology* **83**, 3323–3336.

Tuthill, J. C. and Wilson, R. I. (2016). Mechanosensation and Adaptive Motor Control in Insects. *Current Biology* **26**, R1022–R1038.

Usherwood, P. N. R., Runion, H. I. and Campbell, J. I. (1968). Structure and Physiology of a Chordotonal Organ in the Locust Leg. *J. Exp. Biol.* **48**, 305–323.

Vajente, N., Norante, R., Pizzo, P. and Pendin, D. (2020). Calcium Imaging in Drosophila melanogaster. In *Calcium Signaling* (ed. Islam, Md. S.), pp. 881–900. Cham: Springer International Publishing.

Valle, S., Li, W. and Qin, S. J. (1999). Selection of the Number of Principal Components: The Variance of the Reconstruction Error Criterion with a Comparison to Other Methods. *Ind. Eng. Chem. Res.* **38**, 4389–4401.

Venken, K. J. T., Simpson, J. H. and Bellen, H. J. (2011). Genetic Manipulation of Genes and Cells in the Nervous System of the Fruit Fly. *Neuron* **72**, 202–230.

Virtanen, P., Gommers, R., Oliphant, T. E., Haberland, M., Reddy, T., Cournapeau, D., Burovski, E., Peterson, P., Weckesser, W., Bright, J., et al. (2020). SciPy 1.0: fundamental algorithms for scientific computing in Python. *Nat Methods* **17**, 261–272.

Wahl, V., Pfeffer, S. E. and Wittlinger, M. (2015). Walking and running in the desert ant Cataglyphis fortis. *Journal of Comparative Physiology A* **201**, 645–656.

Wang, Z., Bovik, A. C., Sheikh, H. R. and Simoncelli, E. P. (2004). Image Quality Assessment: From Error Visibility to Structural Similarity. *IEEE Trans. on Image Process.* **13**, 600–612.

Wang, X., O'Dwyer, N. and Halaki, M. (2013). A review on the coordinative structure of human walking and the application of principal component analysis. *Neural Regen Res* **8**, 662–670.

Wang Qi, Fu Li, and Liu Zhenzhong (2010). Review on camera calibration. In *2010 Chinese Control and Decision Conference*, pp. 3354–3358. Xuzhou, China: IEEE.

Ward, J. H. (1963). Hierarchical Grouping to Optimize an Objective Function. *Journal of the American Statistical Association* **58**, 236–244.

Waskom, M. (2021). seaborn: statistical data visualization. *JOSS* **6**, 3021.

Weiland, G. and Koch, U. T. (1987). Sensory Feedback During Active Movements of Stick Insects. *Journal of Experimental Biology* **133**, 137–156.

Weiland, G., Bässler, U. and Brunner, M. (1986). A Biological Feedback Control System with Electronic Input: The Artificially Closed Femur-Tibia Control System of Stick Insects. *Journal of Experimental Biology* **120**, 369–385.

Wilson, D. M. (1966). Insect Walking. *Annu. Rev. Entomol.* **11**, 103–122.

Woltring, H. J. (1991). Representation and calculation of 3-D joint movement. *Human Movement Science* **10**, 603–616.

Wong, R. K. and Pearson, K. G. (1976). Properties of the trochanteral hair plate and its function in the control of walking in the cockroach. *J. Exp. Biol.* **64**, 233–249.

Wosnitza, A., Bockemühl, T., Dübbert, M., Scholz, H. and Büschges, A. (2013). Inter-leg coordination in the control of walking speed in Drosophila. *Journal of Experimental Biology* **216**, 480–491.

Yamaguchi, S., Desplan, C. and Heisenberg, M. (2010). Contribution of photoreceptor subtypes to spectral wavelength preference in Drosophila. *Proceedings of the National Academy of Sciences of the United States of America* **107**, 5634–5639.

Zakotnik, J., Matheson, T. and Dürr, V. (2004). A posture optimization algorithm for model-based motion capture of movement sequences. *Journal of Neuroscience Methods* **135**, 43–54.

Zenkevich, L. A. (1945). The evolution of animal locomotion. *J. Morphol.* **77**, 1–52.

Zhang, Z. (2000). A flexible new technique for camera calibration. *IEEE Trans. Pattern Anal. Machine Intell.* **22**, 1330–1334.

Zill, S. N. (1985). Plasticity and proprioception in insects. I. Responses and cellular properties of individual receptors of the locust metathoracic femoral chordotonal organ. *Journal of Experimental Biology* **116**, 435–461.

Zill, S. N. (1987). Selective mechanical stimulation of an identified proprioceptor in freely moving locusts: role of resistance reflexes in active posture. *Brain Research* **417**, 195–198.

Zill, S., Schmitz, J. and Büschges, A. (2004). Load sensing and control of posture and locomotion. *Arthropod Structure & Development* **33**, 273–286.

Zill, S. N., Keller, B. R. and Duke, E. R. (2009). Sensory Signals of Unloading in One Leg Follow Stance Onset in Another Leg: Transfer of Load and Emergent Coordination in Cockroach Walking. *Journal of Neurophysiology* **101**, 2297–2304.

Acknowledgements

First of all, I would like to express my sincere gratitude to Prof. Ansgar Büschges for not only giving me the opportunity to pursue my PhD studies in his research group, but also for being an enthusiastic supervisor, the freedom to pursue my own scientific ideas, and supporting me throughout this scientific journey, especially at the end.

I would like to extend my sincere thanks to Prof. Martin Nawrot for agreeing on being the second referee of this thesis and all the fruitful discussions during my TAC meetings. Many thanks to Prof. Alexander Blanke for contributing to my work as part of my TAC and by analyzing the μCT scan data. In this context, I would also like to thank Dr. Gesa Dinges for providing me with the μCT scan data, without which my work would not have been possible. Furthermore, I would like to thank Prof. Günter Schwarz for be willing to chair my defense.

This endeavor would not have been possible without Dr. Till Bockemühl. Thank you for all the help, motivational and emotional support, and all the discussions about science, kinematics, statistics, programming, and drought monitoring. Working with you always felt really synergistic.

I am deeply grateful to the team of the electronic workshop of the Büschges group and I am indebted to Dipl.-Ing. Michael Dübbert and Mehrdad Ghanbari who greatly supported me in all technical questions and made frequently all my impossible equipment requests come true.

I would further like to thank all members of the AG Büschges, the former and the current, for the warm working atmosphere, all the great scientific discussions, and last but not least for the team building activities aka Mauerbier, lab retreats, etc.. A special thanks to Vincent Godesberg for all the discussions about philosophy and programming, and for giving me new perspectives on the world. Furthermore, I am grateful for the assistance given by Sandra Uckermann, Sherylane Seelinger, and Sima Seyed-Nejadi with regard to help in the laboratory and administrative issues. Special thanks to Dr. Isabell Witt for helping me with all the GSfBS regulations.

I am also grateful to Clarrisa Goldsmith and Prof. Nick Szczecinski for the great discussions about my project and our collaboration.

My heartfelt appreciation goes to my mother Dagmar Haustein and my father Gregor Haustein for their encouragement and support throughout my life. Literally, I would not have come far in life without you.

I owe my deepest gratitude to Mia Lingner for her love. Not only have you supported me through all these years, but you have made me a better person with every single day we spend together.

Erklärung

Hiermit versichere ich an Eides statt, dass ich die vorliegende Dissertation selbstständig und ohne die Benutzung anderer als der angegebenen Hilfsmittel und Literatur angefertigt habe. Alle Stellen, die wörtlich oder sinngemäß aus veröffentlichten und nicht veröffentlichten Werken dem Wortlaut oder dem Sinn nach entnommen wurden, sind als solche kenntlich gemacht. Ich versichere an Eides statt, dass diese Dissertation noch keiner anderen Fakultät oder Universität zur Prüfung vorgelegen hat; dass sie - abgesehen von unten angegebenen Teilpublikationen und eingebundenen Artikeln und Manuskripten - noch nicht veröffentlicht worden ist sowie, dass ich eine Veröffentlichung der Dissertation vor Abschluss der Promotion nicht ohne Genehmigung des Promotionsausschusses vornehmen werde. Die Bestimmungen dieser Ordnung sind mir bekannt. Darüber hinaus erkläre ich hiermit, dass ich die Ordnung zur Sicherung guter wissenschaftlicher Praxis und zum Umgang mit wissenschaftlichem Fehlverhalten der Universität zu Köln gelesen und sie bei der Durchführung der Dissertation zugrundeliegenden Arbeiten und der schriftlich verfassten Dissertation beachtet habe und verpflichte mich hiermit, die dort genannten Vorgaben bei allen wissenschaftlichen Tätigkeiten zu beachten und umzusetzen. Ich versichere, dass die eingereichte elektronische Fassung der eingereichten Druckfassung vollständig entspricht.

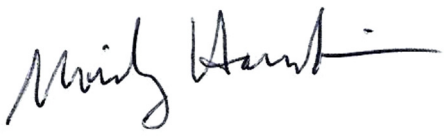

Köln, den 18.12.2022 Moritz Haustein

Teilpublikationen

Conference paper

Goldsmith, C., **Haustein, M.**, Bockemühl, T., Büschges, A., Szczecinski, N. (2022) Analyzing 3D limb kinematics of Drosophila melanogaster for robotic platform development. In: *Biomimetic and Biohybrid Systems*. Living Machines 2022. Lecture Notes in Computer Sciences. Vol 13548. Springer, Cham. DOI: 10.1007/978-3-031-20470-8_12

Poster abstracts

SEB 2021 Annual Conference, held online, June 2021

Title: Modelling leg kinematics of walking fruit flies, *Drosophila melanogaster*

Virtual Interdisciplinary College 2021, held online, April 2021

Title: Modeling leg kinematics of walking fruit flies, *Drosophila melanogaste*r

Virtual Interdisciplinary College 2020, held online, April 2020

Title: 3D motion capture of leg joints in the walking fruit fly *Drosophila melanogaster*

Curriculum Vitae

Moritz Haustein

Education

01/2019 – present	**PhD (Dr. rer. nat.)**, Institute of Zoology, University of Cologne, Cologne, Germany Topic: Decomposition of 3D joint kinematics of walking in *Drosophila melanogaster* Advisor: Prof. Dr. Ansgar Büschges
04/2016 – 10/2018	**MSc in Biological Sciences**, University of Cologne, Cologne, Germany Emphasis: Neurobiology Thesis: The role of chordotonal organs for local pattern-generating activity of a leg stump during walking in *Drosophila* Advisor: Prof. Dr. Ansgar Büschges
10/2011 – 12/2015	**BSc (Honours) in Natural Sciences**, The Open University, Milton Keynes, United Kingdom Project: Effects of platelet-derived growth factors on expansion of murine bone marrow-derived mesenchymal stem cells cultured in a serum-free medium designed for pluripotent stem cell-derived cardiomyocyte maintenance
10/2001 – 09/2003	**Diploma in Biology**, Heinrich-Heine-University, Düsseldorf, Germany (discontinued)

Professional history

05/2016 – 12/2018	**Employee in research**, Paediatric Cardiology, University Hospital of Cologne, Cologne, Cologne, Germany Emphasis: Studied bacterial translocation in patients with Fontan circulation with protein-losing enteropathy.

08/2006 – 04/2016	**Biology laboratory technician**, Paediatric Cardiology/ Institute of Neurophysiology, University Hospital of Cologne, Cologne, Germany Emphasis: Analysed contractile and electrophysiological properties of myocardial tissues and pluripotent stem cell-derived cardiomyocytes
09/2003 – 06/2006	**Vocational training as biology laboratory technician**, University Hospital of Cologne, Germany

Peer-reviewed publications #authors contributed equally

Goldsmith, C., **Haustein, M.**, Bockemühl, T., Büschges, A., Szczecinski, N. (2022) Analyzing 3D limb kinematics of Drosophila melanogaster for robotic platform development. In: *Biomimetic and Biohybrid Systems*. Living Machines 2022. Lecture Notes in Computer Sciences. Vol 13548. Springer, Cham.

Nourse, W. , Szczecinski, N., **Haustein, M.**, Bockemühl, T., Büschges, A., Quinn, R. (2019) Analyzing the Interplay Between Local CPG Activity and Sensory Signals for Inter-leg Coordination in *Drosophila*. In: *Biomimetic and Biohybrid Systems*. Living Machines 2019, vol 11556. Springer, Cham.

Trieschmann, J.[#], **Haustein, M.[#]**, Köster, A., Hescheler, J., Brockmeier, K., Bennink, G., Hannes T. (2019) Different Responses to Drug Safety Screening Targets between Human Neonatal and Infantile Heart Tissue and Cardiac Bodies Derived from Human-Induced Pluripotent Stem Cells. *Stem Cells Int.* 2019:6096294

Trieschmann, J., Bettin, D., **Haustein, M.**, Köster, A., Molcanyi, M., Halbach, M., Hanna, M., Fouad, M., Brockmeier, K., Hescheler, J., Pfannkuche, K., and Hannes, T. (2016) The interaction between adult cardiac fibroblasts and embryonic stem cell-derived cardiomyocytes leads to pro-arrhythmic changes in in vitro co-cultures. *Stem Cells Int*. 2016:2936126

Haustein, M.[#], Hannes, T.[#], Trieschmann, J., Verhaegh, R., Köster, A., Hescheler, J., Brockmeier, K., Adelmann, R., and Khalil, M. (2015). Excitation-contraction coupling in zebrafish ventricular myocardium is regulated by trans-sarcolemmal Ca2+ influx and sarcoplasmic reticulum Ca2+ release. *PLoS One*. 10(5):e0125654

Hannes, T., Wolff, M., Doss, M.X., Pfannkuche, K., **Haustein, M.**, Müller-Ehmsen, J., Sachinidis, A., Hescheler, J., Khalil, M., and Halbach, M. (2015) Electrophysiological characteristics of embryonic stem cell-derived cardiomyocytes are cell line-dependent. *Cell Physiol Biochem*. 35(1):305-314

Rubach, M., Adelmann, R., **Haustein, M.**, Drey, F., Pfannkuche, K., Xiao, B., Koester, A., Udink ten Cate, F.E., Choi, Y.H., Neef, K., Fatima, A., Hannes, T., Pillekamp, F., Hescheler, J., Saric, T., Brockmeier, K., and Khalil, M. (2014) Mesenchymal stem cells and their conditioned medium improve integration of purified induced pluripotent stem cell-derived cardiomyocyte clusters into myocardial tissue. *Stem Cells Dev*. 23(6):643-653

Tang, M., Yin, M., Tang, M., Liang, H., Yu, C., Hu, X., Luo, H., Baudis, B., **Haustein, M.**, Khalil, M., Saric, T., Hescheler, J., and Xi, J. (2013) Baicalin maintains late-stage functional cardiomyocytes in embryoid bodies derived from murine embryonic stem cells. *Cell Physiol Biochem*. 32(1):86-99

Pillekamp, F.[#], **Haustein, M.[#]**, Khalil, M., Emmelheinz, M., Nazzal, R., Adelmann, R., Nguemo, F., Rubenchyk, O., Pfannkuche, K., Matzkies, M., Reppel, M., Bloch, W., Brockmeier, K., and Hescheler, J. (2012) Contractile properties of early human embryonic stem cell-derived cardiomyocytes: beta-adrenergic stimulation induces positive chronotropy and lusitropy but not inotropy. *Stem Cells Dev*. 21(12):2111-2121

Xi, J., Khalil, M., Shishechian, N., Hannes, T., Pfannkuche, K., Liang, H., Fatima, A., **Haustein, M.**, Suhr, F., Bloch, W., Reppel, M., Sarić, T., Wernig, M., Jänisch, R., Brockmeier, K., Hescheler, J., and Pillekamp, F. (2010) Comparison of contractile behavior of native murine ventricular tissue and cardiomyocytes derived from embryonic or induced pluripotent stem cells. *FASEB J*. 24(8):2739-2751

Mauritz, C., Schwanke, K., Reppel, M., Neef, S., Katsirntaki, K., Maier, L.S., Nguemo, F., Menke, S., **Haustein, M.**, Hescheler, J., Hasenfuss, G., and Martin, U. (2008) Generation of functional murine cardiac myocytes from induced pluripotent stem cells. *Circulation*. 118(5):507-517

Conferences

Oral presentations

09/2012	**Title**: 'Power of the beat: Contractile properties of pluripotent stem cell-derived cardiomyocytes' RAMSES Annual Workshop 2012, Institute of Cellular Biology and Pathology "Nicolae Simionescu", Bucharest, Romania
05/2011	**Title**: 'iPS cell culture techniques – practical-related insights' RAMSES 1st multiplier workshop, Cairo University, Cairo, Egypt

Poster presentations

06/2021	**Title:** 'Modelling leg kinematics of walking fruit flies, *Drosophila melanogaster*' SEB 2021 Annual Conference, held online

04/2021	Title: 'Modeling leg kinematics of walking fruit flies, *Drosophila melanogaster*' Virtual Interdisciplinary College 2021, held online
04/2020	Title: '3D motion capture of leg joints in the walking fruit fly *Drosophila melanogaster*' Virtual Interdisciplinary College 2020, held online
03/2019	Title: 'The Role of Chordotonal Organs for Local Pattern-Generating Activity of a Leg Stump during Walking in *Drosophila*' 13th Göttingen Meeting of the German Neuroscience Society, Göttingen, Germany

Awards

04/2021	1st Prize Poster Session Award, Virtual Interdisciplinary College 2021

Voluntary work

10/2020 – present	Elected deputy representative Graduate School for Biological Sciences (GSfBS), University of Cologne, Cologne, Germany

Professional memberships

01/2019 - present	Graduate School for Biological Sciences (GSfBS), University of Cologne, Cologne, Germany
03/2020 - present	Society of Experimental Biology (SEB)
11/2022 - present	German Neuroscience Society (NWG)

Teaching experience

01/2019 - present	**Teaching assistant**, University of Cologne, Cologne, Germany Course: Introduction in MATLAB, 10 students, 1-2 weeks, annually Course: Animal physiology for BScs, 200 students, 1 week, annually
08/2006 – 04/2016	**Trained biology laboratory technicians,** in cell culture techniques, contraction measurements and fluorescence microscopy